A STUDY OF LEPTONIC DECAY CHANNELS AT THE Z° RESONANCE PEAK

Andrew Charles Pinsent

Merton College

A thesis submitted for the degree of Doctor of Philosophy at the University of Oxford

Michaelmas Term 1990

Front Cover Photograph

A close-up view of the barrel of the DELPHI particle detector, showing the barrel muon chamber modules, designed and manufactured by Oxford University's Nuclear and Astrophysics Department, covering the outer surface. *(a picture of the LEP collider is shown on the back cover)* .

A STUDY OF LEPTONIC DECAY CHANNELS AT THE Z° RESONANCE PEAK

Andrew Charles Pinsent
Merton College

Submitted for the degree of Doctor of Philosophy
Michaelmas Term, 1990

ABSTRACT

This thesis presents an experimental test of the ratio of charged lepton to hadron production in Z^0 boson decays against the theoretical prediction of the Glashow-Salam-Weinberg Standard Model, and also details a test of lepton universality at an energy scale of $s \sim 8300(\mathrm{GeV})^2$. The data sample is taken from the DELPHI experiment which operates at the newly commissioned LEP collider, running at centre of mass collision energies that scan across the resonance peak for Z^0 production at around 91GeV.

The value of the hadron/charged lepton partial width ratio (Γ_{had}/Γ_{ll}) is calculated to be 20.85 in the GSW theory with an error of 1% due to the uncertainty of the value of the strong interaction coupling constant α_s at LEP energies. This ratio is shown to be nearly independent of two of the principal unknown parameters of the Standard Model, the top quark mass and Higgs boson mass, making its value a highly constrained prediction. A brief overview of the DELPHI experiment is given, with special attention being paid to the detector components crucial to the leptonic analysis. The analysis procedure is then described in detail, with the data samples from 1989 and 1990 treated separately due to systematic changes in detector performance between the two running periods. The final experimental values for Γ_{had}/Γ_{ll} are found to be $\Gamma_{had}/\Gamma_{ee} = 21.73 \pm 0.59(\mathrm{stat.}) \pm 0.49(\mathrm{syst.})$ for electrons, and $\Gamma_{had}/\Gamma_{\mu\mu} = 20.94 \pm 0.61(\mathrm{stat.}) \pm 0.37(\mathrm{syst.})$ for muons. The average of these values is found to be $\Gamma_{had}/\Gamma_{ll} = 21.33 \pm 0.43(\mathrm{stat.}) \pm 0.35(\mathrm{syst.})$ and this agrees well with an improved theoretical computation of $\Gamma_{had}/\Gamma_{ll} = 20.69 \pm 0.10$, which uses a measurement of $\alpha_s[{M_Z}^2] = 0.106 \pm 0.006(\mathrm{stat.}) \pm 0.007(\mathrm{syst.})$ obtained from DELPHI hadronic data studies.

A direct comparison of the electron and muon samples gives a relative production rate $\Gamma_{ee}/\Gamma_{\mu\mu} = 0.964 \pm 0.038(\mathrm{stat.}) \pm 0.022(\mathrm{syst.})$, and a comparison with a sample of tau events yields $\Gamma_{\tau\tau}/\Gamma_{\mu\mu} = 1.00 \pm 0.06(\mathrm{stat.})$. Within the precision of these measurements lepton universality is therefore confirmed at this energy scale.

All the experimental values obtained are therefore in agreement with the predictions of the Standard Model.

ACKNOWLEDGEMENTS

This thesis details an analysis of data recorded by the DELPHI experiment at the LEP particle collider, which has provided since its inauguration in August 1989 an opportunity for a precision study of the behaviour of matter at an energy scale of $\sim 8300(\mathrm{GeV})^2$. This thesis is consequently one of the indirect results of a tremendous amount of work by many people over nearly a decade of planning and construction, as well as an investment of several hundred million pounds by the taxpayers of Europe.

I would like to thank the Department of Nuclear and Astrophysics at Oxford University for providing me with the opportunity to participate in this extraordinary project.

I would like to thank my colleagues at the Department who are involved with the DELPHI project for all their friendship and encouragement. While it is impossible to thank everyone, I would like to mention my supervisor, Dr. Alan Segar, for offering consistent good advice and encouragement, and also Dr. Peter Renton who has been closely involved with my work. Also in this category are my fellow graduate students working on DELPHI, Timothy Adye, Martin Bates, Christine Beeston, Simon Blyth, Harald Borner, Paula Collins, Simon Hodgson, Guy Wilkinson, Elizabeth Veitch and above all Nigel Crosland, who have helped to make my time both in Oxford and Geneva so enjoyable.

There are also many individuals and groups outside the high energy physics community to whom I am deeply indebted - most obviously my parents, Charles and Teresa, and my sisters, Jane and Katherine. Many members of my wider family have also given me much love and support, and I would like to mention some special friends, Jonathan Gregory, Nigel Dowrick, David Clark and Gareth Leach. I would also like to thank Nigel Veitch, another good friend, and Brian Perkins for an excellent holiday in Kenya in 1988, and Sonia Batista and Márcia Lopes for a marvellous holiday in Brazil in July 1990. In addition I am grateful to Maria Von Schlippe and the University Ballroom Dance Team for teaching me ballroom dancing and thereby providing me with a welcome relief from my computer terminal. While in Geneva I was also able to enjoy the friendship of members of the choir of the John XXIII Catholic Church, and I am very grateful in addition to the Christian community at 11, Norham Gardens for providing me with a place to stay at those irregular times when I have been in Oxford over the last three years.

I would like to thank the Science and Engineering Research Council (SERC) who have been my principal source of financial support while doing this research and, in addition, International Computers Limited (ICL) for an industrial sponsorship.

Finally, I acknowledge that although I have worked hard over the past three years I have also been very blessed in the activities I have undertaken. This thesis is therefore offered up to the greater praise and glory of God who has, in His wisdom, created a world of extraordinary subtlety and beauty, and who has given to us frail creatures of dust, minds with which to explore and appreciate its wonder.

Deo Gratias

November 1990

> *'Then the Star Maker said, "Let there be light." And there was light.*
> *From all the coincident and punctual centres of power, light leapt and blazed.'*
>
> *(Olaf Stapleton, "Star Maker", 1937.)*

Contents

List of Figures

List of Tables

Chapter 1

The Standard Model Of Electroweak Interactions

Preamble

Chapter 1 presents a brief overview of the Glashow-Salam-Weinberg Standard Model of electroweak interactions, starting with quantum electrodynamics (QED), tracing out the major ideas and providing a non-rigorous derivation of the principal results. The motivation for constructing the LEP collider is explained and the lowest order theoretical prediction of the Z^0 partial width ratios to charged lepton channels and hadrons derived; a more precise result is also quoted. The equivalence of the production rates of s-channel electrons, muons and taus (lepton universality) in the standard model is also noted as a prediction to be tested. Finally the procedure of subsequent chapters in obtaining the experimental partial width ratios from the DELPHI experiment at LEP is explained, together with a brief summary of the theoretical computer models that play an essential part in that analysis.

1.1 Quantum Electrodynamics

The Dirac Lagrangian which describes the behaviour of a free electron is

$$\mathcal{L}_D = \overline{\psi}(i\gamma^\mu \partial_\mu - m)\psi. \tag{1.1}$$

where ψ is the Dirac spinor for the electron field, m is the electron mass, and the γ_μ span a four dimensional matrix representation of the algebra $\{\gamma_\mu, \gamma_\nu\} = 2g_{\mu\nu}$ [1] ; this equation has the desired property of covariance under Lorentz transformations.

In the theory of QED (Quantum Electrodynamics), which is a gauge theory, this equation should be invariant i.e lead to an equivalent description of the same physical reality, under the local U(1) phase transformation

$$\psi(\mathbf{x}) \rightarrow \psi'(\mathbf{x}) = e^{-ie\chi(\mathbf{x})}\psi(\mathbf{x}), \tag{1.2}$$

[1] A standard metric that is often used for the values of $g_{\mu\nu}$ is that $g_{\mu\nu} = 0$ except for $g_{00} = 1, g_{11} = -1, g_{22} = -1, g_{33} = -1$

Equation 1.1 is not, by itself, U(1) gauge invariant but can be made so by adding a term

$$\mathcal{L}_{INT} = -\overline{\psi}\gamma^{\mu}\psi\partial_{\mu}e\chi(\mathbf{x}) = -e\overline{\psi}\gamma^{\mu}\psi A_{\mu} \tag{1.3}$$

to the original Lagrangian, provided the new field A_{μ} transforms as

$$A_{\mu} \rightarrow A'_{\mu} = A_{\mu} + \partial_{\mu}\chi(\mathbf{x}). \tag{1.4}$$

However, if the new field A_{μ} is to be physically interesting, some kinetic term must be also added to describe its behaviour. A possible term which is also locally U(1) gauge invariant is

$$\mathcal{L}_{EM} = -\frac{1}{4}G_{\mu\nu}G^{\mu\nu} \tag{1.5}$$

where

$$G_{\mu\nu} = \partial_{\mu}A_{\nu} - \partial_{\nu}A_{\mu}. \tag{1.6}$$

It should be noted that when the total expression is now substituted into the classical Euler-Lagrange field equation

$$\partial_{\mu}\left(\frac{\partial\mathcal{L}}{\partial(\partial_{\nu}A_{\mu})}\right) - \frac{\partial\mathcal{L}}{\partial A_{\mu}} = 0 \tag{1.7}$$

the following equation is obtained

$$\Box A^{\mu} - \partial^{\mu}(\partial_{\nu}A^{\nu}) = e\overline{\psi}\gamma^{\mu}\psi \tag{1.8}$$

If $e\overline{\psi}\gamma^{\mu}\psi$ is identified with the electromagnetic current and if $\partial_{\nu}A^{\nu} = 0$ (the Lorentz Gauge) is *chosen*, this is now the covariant form of Maxwell's equations for electromagnetism i.e

$$\Box A^{\mu} = j^{\mu}. \tag{1.9}$$

This would therefore seem to be a good candidate for a quantum theory of electromagnetism. The final locally U(1) invariant Lagrangian can be written as

$$\mathcal{L} = \overline{\psi}(i\gamma^{\mu}D_{\mu} - m)\psi - \frac{1}{4}G_{\mu\nu}G^{\mu\nu} \tag{1.10}$$

where

$$D_{\mu} \equiv (\partial_{\mu} + ieA_{\mu}). \tag{1.11}$$

D_{μ} is called the *covariant derivative.*

The principle of gauge invariance can therefore be used to produce the covariant form of Maxwell's equations for the electromagnetic field, and to show the existence of an interaction term between the electron field and the electromagnetic field with a coupling strength e, which is not fixed by the theory and must be empirically determined. This derivation was first carried out by C.N.Yang and R.L.Mills in 1954 [1]. Fig. 1.1 shows a Feynman diagram representation of the interaction term which forms the lowest order contribution to the total matrix element of a calculation of a physical process. However,

Figure 1.1: Feynman Diagrams of (a) the first order interaction of an electron and photon field and (b) the vacuum polarisation correction.

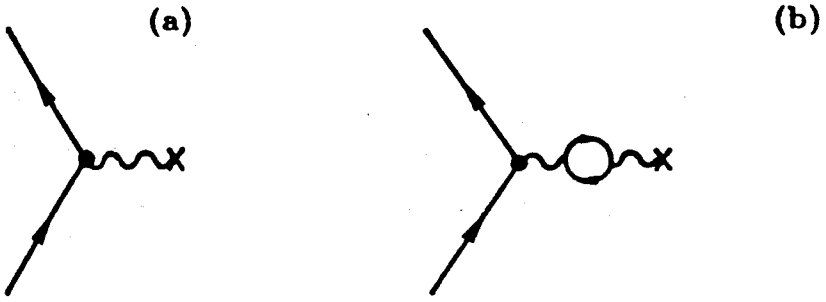

the full calculation of the matrix element also includes higher order terms such as the diagram on the right of the figure. These loop terms are problematical, because the loop momentum can take any value from 0 to ∞, and this leads to divergent integrals. The procedure followed to solve this problem is to regularize (modify) the divergent expression to give a finite integral and then renormalise the potentially divergent parts in terms of physically measurable quantities (e.g. mass and charge in the $q^2 \rightarrow 0$ limit, where q is the momentum transfer to the electron in the measurement process); the final result should not depend on the regularisation process. This procedure is known as *renormalisation* and the fact that gauge theories can produce renormalisable results makes them interesting candidates for describing the forces found in nature. A theory does not *have* to be renormalisable to be useful; however non-renormalisable theories break down at some energy scale (a scale which can signify new physics), whereas any candidate

for a fundamental description of some aspect of nature must be able to operate at any energy scale [2].

It is in principle possible to calculate the effect of the higher order terms in QED. This has been done for certain situations where very precise experiments are also possible; to date no experimental measurement has been found to be in disagreement with the QED predictions. [3].

1.2 Weak Interactions

The first model of weak interactions was a pointlike interaction of four fermions at a vertex with a fixed coupling constant. This was developed by E.Fermi [4] as a model of nuclear beta decay, and was modified to a V-A theory by R.P Feynman and M.Gell-Mann in 1958 [5] after an experiment by C.S.Wu *et al* [6] that showed that the weak interaction was parity violating. N.Cabbibo provided a framework for explaining the existence of strangeness changing weak interactions by proposing that the weak interactions couple to quark states that are a rotation in isospin space of the quark mass eigenstates [7] . A problem remains in the weak theory with the dimensional pointlike Fermi coupling constant G_F; at high energies a weak interaction cross-section which must behave like ${G_F}^2E^2$ on dimensional grounds, and which must be pure s-wave in a partial wave analysis of the interaction, eventually violates the upper bound (at $\sim$ 300GeV) on the cross-section of each partial wave component which falls like $\pi/2E^2$. A possible solution is to propose a heavy vector particle of mass M_W transmitting the weak force in an analogous way to the photon in QED; it has to be heavy to account for the short range nature of the force. The coupling is now replaced by $G/\sqrt{2} \rightarrow g^2/(q^2 - {M_W}^2)$ and there must be at least two massive bosons for carrying positive and negative charge; however infinities remain in the higher order calculations.

[2]This is not the only reason for interest in gauge theories; what is of more importance is that a theory of quark-quark interactions can be developed with them, QCD (Quantum Chromo Dynamics), that is renormalisable and which can also model asymptotic freedom.

[3]One of the most precise confirmations of the theory is in the measurement of the anomalous magnetic moment of the electron. The eighth order QED contribution has been calculated by T.Kinoshita *et al.* [2] thereby making the most precise theoretical prediction to be $g-2 = (1\ 159\ 652\ 411 \pm 166) \times 10^{-12}$; the value of α used is taken from the Josephson effect measurement by Williams and Olsen, 1979. This prediction has been experimentally confirmed to be $(1\ 159\ 652\ 222 \pm 50) \times 10^{-12}$ by P.B.Schwinberg *et al.* [3].

Following the procedure of Section 1.1 it would seem worthwhile to attempt to use the gauge principle for deriving the weak interactions; the problem of infinities in the higher order calculations might then be removed by renormalisation. A possible candidate for the deriving the forms of the weak interactions is an SU(2) gauge invariant theory, which signifies invariance under transformations of the form

$$\psi'(\mathbf{x}) = e^{-ig\boldsymbol{\alpha}(\mathbf{x}).\boldsymbol{\tau}/2}\psi(\mathbf{x}) \tag{1.12}$$

where the $\boldsymbol{\tau}$ matrices are a representation of SU(2). A 2-dimensional matrix representation is provided by the Pauli Spin Matrices:

$$\boldsymbol{\tau} = \begin{pmatrix} 0 & 1 \\ 1 & 0 \end{pmatrix}, \begin{pmatrix} 0 & -i \\ i & 0 \end{pmatrix}, \begin{pmatrix} 1 & 0 \\ 0 & -1 \end{pmatrix}. \tag{1.13}$$

For an infinitesimal transformation

$$\psi'(\mathbf{x}) = (1 - ig\boldsymbol{\alpha}(\mathbf{x}).\boldsymbol{\tau}/2)\psi(\mathbf{x}), \tag{1.14}$$

the required covariant derivative is now

$$D_\mu \equiv (\partial_\mu + ig\boldsymbol{\tau}.\boldsymbol{W}_\mu/2). \tag{1.15}$$

The three $\boldsymbol{W}^\mu$ compensating fields must themselves transform as

$$\delta\boldsymbol{W}^\mu = \partial^\mu\delta\boldsymbol{\alpha} + g\delta\boldsymbol{\alpha}\times\boldsymbol{W}^\mu. \tag{1.16}$$

A kinetic term for the new fields can be added as before and a candidate that satisfies the local SU(2) invariance requirement is

$$\mathcal{L} = -\frac{1}{4}\boldsymbol{F}_{\mu\nu}.\boldsymbol{F}^{\mu\nu} \tag{1.17}$$

where

$$\boldsymbol{F}_{\mu\nu} = \partial^\mu\boldsymbol{W}_\nu - \partial^\nu\boldsymbol{W}_\mu - g(\boldsymbol{W}^\mu\times\boldsymbol{W}^\nu). \tag{1.18}$$

This theory, which can accommodate particles like the W^+, W^- and photon was first developed by C.N.Yang and R.Mills. A feature that should be noted is that unlike the electromagnetic field derived from U(1) gauge invariance, there are self-interaction terms of these fields at lowest order. Unfortunately, although the problem of renormalisation is solved by using a gauge theory the vector bosons

have no mass as there are no terms of the form $m_W W^\nu W_\nu$, nor are such terms possible if invariance is to be maintained under Equation 1.12. A solution to this problem, which allows both renormalisation and massive vector bosons is to introduce the concept of "hidden" symmetry suggested by P.Higgs [8]; this is the method followed in the model of electroweak interactions (today's standard model) developed by Glashow, Salam and Weinberg [9].

1.3 The Higgs Mechanism and the GSW Theory

The GSW (Glashow, Salam, Weinberg) model of electroweak interactions is based on the gauge group $SU(2) \otimes U(1)$. This gives rise to $3 + 1$ fields, for which there are dimensionless coupling constants g and g' which are not predicted by the model. To generate the particle masses, while retaining renormalisability, the Higgs mechanism of spontaneous symmetry breaking is introduced. In the minimal model this involves introducing an SU(2) doublet of complex scalar fields ϕ where

$$\phi = \begin{pmatrix} \phi_\alpha \\ \phi_\beta \end{pmatrix} = \frac{1}{\sqrt{2}} \begin{pmatrix} \phi_1 + i\phi_2 \\ \phi_3 + i\phi_4 \end{pmatrix} \tag{1.19}$$

The Klein-Gordon Lagrangian for such a set of non-interacting bosonic fields would be

$$\mathcal{L}_{KG} = \partial_\mu \phi^\dagger \partial^\mu \phi - \frac{1}{2}\mu^2 \phi^\dagger \phi. \tag{1.20}$$

The shape of this potential energy component of this formula in $(\phi_\alpha, \phi_\beta)$ space is shown in Fig. 1.2(a). However, these minimal Higgs fields are based on a different kind of potential the shape of which is shown in Fig 1.2(b).

$$\mathcal{L}_H = \partial_\mu \phi^\dagger \partial^\mu \phi + \frac{1}{2}\mu^2 \phi^\dagger \phi - \frac{1}{2}\lambda^2 (\phi^\dagger \phi)^2. \tag{1.21}$$

The important point to notice in the new Lagrangian is that the origin is no longer a point of stable equilibrium. The true equilibrium configuration is the locus ${\phi_\alpha}^2 + {\phi_\beta}^2 = \mu^2/\lambda^2$. However, although there are infinitely many possibilities for the stable configuration, once a point is chosen the rotational symmetry about the third axis will be lost and the symmetry will be "hidden". To obtain a sensible perturbation theory it is now necessary to expand ϕ about some stable

Figure 1.2: The potential energy term in the Klein-Gordon Lagrangian (a) and $\mathcal{L}_H$ (see text) (b) plotted as a function of the two-component field ϕ with $\lambda = \mu = 1$

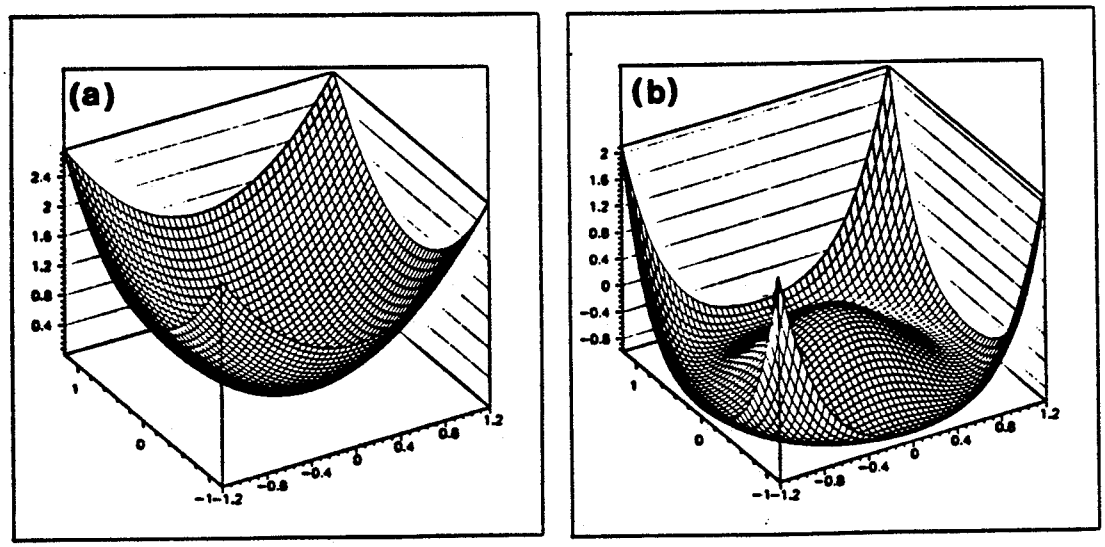

field configuration on the locus of the equilibrium states. For this work it is convenient to choose a polar coordinate system (ρ, θ). The vacuum expectation value of the system can be chosen to be

$$< 0|\phi|0 >= \begin{pmatrix} 0 \\ f/\sqrt{2} \end{pmatrix}; \quad f = \mu/\lambda \tag{1.22}$$

and the general ϕ is then described by

$$\phi = \frac{1}{\sqrt{2}} \exp(-i\tau.\theta(\mathrm{x})/2f). \begin{pmatrix} 0 \\ f + H(\mathrm{x}) \end{pmatrix}. \tag{1.23}$$

Under local SU(2) transformations of the form in Equation 1.12 it is always possible to *choose*

$$\alpha = -\theta/fg, \tag{1.24}$$

and therefore,

$$\phi' = \begin{pmatrix} 0 \\ f + H(\mathrm{x})/\sqrt{2} \end{pmatrix}. \tag{1.25}$$

The full $SU(2) \otimes U(1)$ invariant Lagrangian for the original bosonic field is

$$\mathcal{L} = D_\mu \phi^\dagger D^\mu \phi + \frac{1}{2}\mu^2 \phi^\dagger \phi - \frac{1}{2}(\lambda^2 \phi^\dagger \phi)^2 - \frac{1}{4} F_{\mu\nu}.F^{\mu\nu} - \frac{1}{4} G_{\mu\nu} G^{\mu\nu} \tag{1.26}$$

where the covariant derivative is now a combination of 1.11 and 1.15:

$$D_\mu \equiv (\partial_\mu + ig\tau.W_\mu/2 + ig' B_\mu/2). \tag{1.27}$$

If Equation 1.25 is now substituted into this we obtain

$$\mathcal{L} = \frac{1}{2}\partial_\mu H \partial^\mu H - \frac{1}{2}\mu^2 H^2 - \frac{1}{4}F^{1,2}{}_{\mu\nu}F^{1,2\mu\nu} + \frac{1}{8}g^2 f^2 W^{1,2}{}_\mu W^{1,2\mu} - \frac{1}{4}F^Z{}_{\mu\nu}F^{Z\mu\nu} + \frac{1}{8}f^2(g^2+g'^2)Z_\mu Z^\mu - \frac{1}{4}F^A{}_{\mu\nu}F^{A\mu\nu} + \cdots \quad (1.28)$$

where the linear combinations

$$Z^\mu \equiv (gW^{3\mu} - g'B^\mu)/\sqrt{(g^2+g'^2)} \equiv \cos(\theta_W)W^{3\mu} - \sin(\theta_W)B^\mu, \quad (1.29)$$

$$A^\mu \equiv (g'W^{3\mu} + gB^\mu)/\sqrt{(g^2+g'^2)} \equiv \sin(\theta_W)W^{3\mu} + \cos(\theta_W)B^\mu \quad (1.30)$$

have been substituted. θ_W is called the Weinberg weak mixing angle. The crucial point about the expressions above is that three of the fields have acquired mass:

$$m_{W^1} = m_{W^2} = gf/2; \quad m_Z = \frac{1}{2}f^2\sqrt{(g^2+g'^2)} = m_{W^1}/\cos(\theta_W). \quad (1.31)$$

There is also one massless field term left. The Standard Model now equates the massless field with the photon, and its interactions with electromagnetism, and two of the massive bosons $W^{1,2}$ with the charged carriers of the weak interaction. The Lagrangian is no longer, of course, $SU(2) \otimes U(1)$ gauge invariant. However the symmetry is still manifest in the relationship of the masses and couplings of the fields which gives the theory predictive power. It also retains the additional advantage of renormalisation, a feature first demonstrated by t'Hooft in 1971. However, a third (electrically neutral) massive boson (the Z° boson) remains which is an apparently indispensable element; evidence for neutral weak currents was first found in mid-1973 using the Gargamelle bubble chamber at CERN [10] when a neutrino beam was found to interact with a nuclear target without generating charged leptons in the final state. Another particle, a scalar Higgs boson, is also predicted to exist in this scheme but its mass is undetermined.

The GSW theory now takes the framework of the above equations and relates them to experimental observation. The SU(2) transformations of the theory are assumed to act on doublets of particles (called weak isodoublets) - thereby coupling these. The lepton and lepton neutrino of the three generations of particles are each taken to form a particle doublet; likewise the two quarks in each generation (though note that these quarks are mixtures of the mass eigenstates). However the experimental observation of weak interaction parity

violation modifies this scheme; and only the left handed particle states form doublets e.g $L_e \equiv (\nu_{eL}, e_L)$ while the right handed states are taken to form singlets $R_e \equiv e_R$ (no right handed neutrino has been observed to exist). The charged weak interaction only couples to the left handed states, the electromagnetic current to both equally and the weak neutral current to both but with different strengths.

The question is now how to fix the relative strengths of the couplings to the singlets and doublets. Glashow suggested that the e-m charge should be given by the analogue of the GMN relation (Gell-Mann (1953), Nishijima (1955))

$$Q_{e.m} = e(T_3 + y/2) \tag{1.32}$$

where y is the "weak hypercharge", the eigenvalue of the U(1) part of the $SU(2)_L \otimes U(1)$ group, and T_3 is the third component of weak isospin (in this convention $+1/2$ for neutrinos, u-like quarks, $-1/2$ for charged leptons and d-like quarks, 0 for right handed states) [4]. This gives

$$y = -1 \text{ for } \begin{pmatrix} \nu_e \\ e \end{pmatrix}_L, \tag{1.33}$$

$$y = -2 \text{ for } e_R \equiv R_e. \tag{1.34}$$

The fermionic part of the $SU(2)_L \otimes U(1)_y$ gauge invariant Lagrangian for a single lepton doublet is now

$$\mathcal{L}_F = \overline{L_e} i\gamma^\mu(\partial_\mu + ig\tau.W_\mu/2 + ig'B_\mu/2)L_e + \overline{R_e} i\gamma^\mu(\partial_\mu - ig'B_\mu)R_e. \tag{1.35}$$

The symmetry breaking Higgs field is now introduced and the analysis of (1.25) to (1.30) goes through as before; though an extra term (the Yukawa term) has to be added to preserve SU(2) symmetry; this term couples the Higgs field and the leptonic fields. After considerable algebra the expression for the interaction of any quark or lepton doublet with the electroweak fields comes out to be:

$$\begin{aligned} \mathcal{L}_{INT} = \quad & eJ_{em}{}^\mu A_\mu + \frac{e}{2\sqrt{2}\sin(\theta_W)}(J_+{}^\mu W_{-\mu} + J_-{}^\mu W_{+\mu}) + \\ & \frac{e}{2\cos(\theta_W)\sin(\theta_W)} J_{NC}{}^\mu Z_\mu \end{aligned} \tag{1.36}$$

[4] A very good account of the reasoning behind this general expression is given in [11] Chapter 16.

where $g\sin(\theta_W)$ has been equated with e - the modulus of the charge on the electron - as the strength of the coupling of the charged lepton and electromagnetic fields, and where

$$J_{em}{}^{\mu} = \sum_f e_f \overline{f}\gamma^{\mu} f; \quad e_f = \begin{cases} -1 & \text{charged leptons} \\ +2/3 & \text{u} - \text{like quarks} \\ -1/3 & \text{d} - \text{like quarks} \end{cases} \tag{1.37}$$

This, the electromagnetic current, is a pure vector current. The charged currents:

$$J_+{}^{\mu} = (\overline{\nu}_e \overline{\nu}_{\mu} \overline{\nu}_{\tau})\gamma^{\mu}(1-\gamma_5)1 \begin{pmatrix} e \\ \mu \\ \tau \end{pmatrix} + (\overline{u}\overline{c}\overline{d})\gamma^{\mu}(1-\gamma_5)V_{KM} \begin{pmatrix} d \\ s \\ b \end{pmatrix}, \tag{1.38}$$

$$J_-{}^{\mu} = (J_+{}^{\mu})^+, \tag{1.39}$$

where V_{KM} is the Kobayashi-Maskawa mixing matrix [19], have a V-A structure, reflecting the fact that only the left handed fermions have non trivial transformation properties under SU(2). Finally the neutral current has mixed vector and axial vector transformation properties:

$$J_{NC}{}^{\mu} = 2\sum_f \overline{f}(V_f\gamma^{\mu} + A_f\gamma^{\mu}\gamma_5)f \tag{1.40}$$

where

$$\begin{aligned} V_f &= \frac{1}{2}(T_3)_f - e_f \sin^2(\theta_W) \\ A_f &= -\frac{1}{2}(T_3)_f \\ (T_3)_f &= \begin{cases} +1/2 & \text{neutrinos, u} - \text{like quarks} \\ -1/2 & \text{charged leptons, d} - \text{like quarks} \end{cases} . \end{aligned} \tag{1.41}$$

1.4 The Motivation for the LEP Collider

The relation between the Fermi coupling constant in the V-A theory and the GSW model at lowest order is

$$\frac{G_F}{\sqrt{2}} = \frac{g^2}{8{M_W}^2} \tag{1.42}$$

This determines the W mass:

$${M_W}^2 = \pi\alpha/\sqrt{2}\sin^2(\theta_W)G_F \tag{1.43}$$

From the results of the previous section the hidden symmetry of the model relates the W and Z masses by

$$\sin^2(\theta_W) = 1 - \frac{{M_W}^2}{{M_Z}^2} \tag{1.44}$$

The Gargamelle experiment was able to measure the ratio of the charged current and neutral current interactions, and later experiments were able to improve on these measurements and to estimate the value of $\sin^2(\theta_W)$ to be ~ 0.23. With this figure the value of M_W comes out as $\sim$ 78GeV and the M_Z at $\sim$ 89GeV; better estimates are possible with higher order calculations. These figures indicate the scale of the energy required for precision tests of the electroweak theory, as interactions mediated by the W and Z will peak in magnitude around their mass values.

The W and Z bosons were discovered at this energy scale by the two large collaborations UA1 and UA2 working at the SPS proton-antiproton collider in 1982 [12]; the value of M_W was found to be $(81.1 \pm 0.8 \pm 1.2)$GeV and M_Z to be $(94.0 \pm 1.0 \pm 1.4)$GeV. This was a dramatic confirmation of the electroweak theory; however only a handful of W's and Z's could be detected and their properties could not be accurately measured. The problem was particularly acute for the Z° since its interactions tend to be masked by photon exchange processes at lower energies. To solve this problem the LEP collider has been constructed by the CERN organisation to collide electron and positron beams at a centre of mass energy of up to 100GeV and at sufficient luminosity to create $\sim 10^6$ Z°'s per year in clean events and at rest in the inertial frame of the detectors. By generating Z°'s near the peak of the resonance the Z° mediated interactions exceed the photon exchange background processes by approximately two orders of magnitude (as shown in the following section) and precision tests of their properties are possible for the first time.

At a future stage in the project it is planned to double the centre of mass energy to nearly 200GeV in the accelerator which will enable the process $Z^\circ \rightarrow W^+W^-$ to be studied. However this requires the installation of superconducting accelerating cavities which will not be completed until 1994.

CERN has produced several detailed reports on physics at LEP (the most recent is ref. [17]). The following sections deal with the theoretical partial

width ratio of charged lepton and hadron production which is under experimental investigation in this thesis.

1.5 Predicted Hadron/Charged Lepton Production Ratios at LEP Energies

The aim of this thesis, the experimental details and results of which are outlined in subsequent chapters, is to test the relative decay rates of the Z° into hadrons and charged leptons against the predictions of the standard model and to test whether the decay rates into different lepton generations are the same. To first order the interaction $e^+e^- \rightarrow f\overline{f}$ via *photon* exchange (i.e QED processes only) is proportional to the square of the coupling of the particle field f to the photon field i.e the square of the charge. The ratio $(e^+e^- \rightarrow \text{hadrons})/\ (e^+e^- \rightarrow \mu^+\mu^-)$ should therefore be

$$R_{QED} = \left(\sum_{f=u,d,s,c,b} (e_f)^2 \times 3 \right) /(1)^2 = 11/3 \sim 3.67 \qquad (1.45)$$

where f is summed over the five quark states accessible above the upsilon resonances ($\sim$ 10GeV), the e_f are their electric charges and the factor of 3 allows for decays into the three colour states of the quarks.

An analogous derivation is possible for the same processes via Z° exchange (i.e weak interactions only). Using the terms of Equation 1.40 for the weak neutral current the decay amplitude for a Z° is given to lowest order by

$$T = \frac{e}{\cos(\theta_W)\sin(\theta_W)} \epsilon^\mu{}_Z(\lambda)\overline{u}_f[V_f\gamma^\mu + A_f\gamma^\mu\gamma_5]v_{\overline{f}}. \qquad (1.46)$$

where u_f and $v_{\overline{f}}$ are the Dirac spinors of the outgoing fermion-antifermion pair and $\epsilon^\mu{}_Z(\lambda)$ is the polarisation vector of the Z°. It is relatively straightforward to show from this that the partial width is proportional to $c_f({V_f}^2 + {A_f}^2)$ if the masses of the outward fermions are treated as negligible. c_f is a colour factor which is 1 for charged leptons and 3 to lowest order for quarks. However there is a substantial correction to this colour factor in both photon and Z° exchange from higher order QCD diagrams such as are shown in Fig. 1.3. These have the effect of modifying the colour factor for quarks to $3 \times (1 + \alpha_s[{M_Z}^2]/\pi + ...$ higher

Figure 1.3: Feynman diagrams of QCD corrections to the decay process $Z^\circ \to q\bar{q}$.

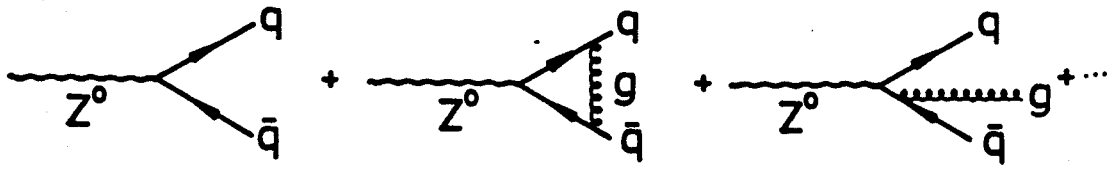

order terms). Using the estimate $\alpha_s[M_Z{}^2]/\pi = (0.04 \pm 0.01)$ [18] this gives a value of $c_{quark} \sim 3.12$ and the ratio of hadron to muon production from Z° decay to lowest order is therefore predicted to be

$$R_{weak+QCD} =$$

$$\frac{2[3.12(1+(1-(8/3)\sin^2(\theta_W))^2)]^{\text{u-like}}_{\text{quarks}} + 3[3.12(1+(1-(4/3)\sin^2(\theta_W))^2)]^{\text{d-like}}_{\text{quarks}}}{(1+(1-4\sin^2(\theta_W))^2)}$$

$$\sim 20.8 \tag{1.47}$$

The error on this evaluation due to the uncertainty of the value of $\alpha_s[M_Z{}^2]$ is 1%.

Both photon and Z° exchange interactions will take place at LEP energies. The lowest order Feynman Diagrams for muon production near the Z° resonance peak by both processes are shown in Fig. 1.4. A straightforward calculation, dropping fermion mass terms, gives

$$\sigma(e^+e^- \to \mu^+\mu^-) = \frac{4\pi\alpha^2}{3s}\left\{1 + \frac{2s(s-M_Z{}^2)}{\sin^2(\theta_W)\cos^2(\theta_W)}\frac{V_e{}^2}{|s-M_Z{}^2+iM_Z\Gamma_Z|^2} + \frac{s^2}{(\sin^2(\theta_W)\cos^2(\theta_W))^2}\frac{(V_e{}^2+A_e{}^2)^2}{|s-M_Z{}^2+iM_Z\Gamma_Z|^2}\right\} \tag{1.48}$$

where s is the square of the centre of mass energy of the colliding particles and M_Z and Γ_Z are the Z° mass and width parameters of the resonance. The first term is the photon exchange (QED) term, the third is the Z° neutral current

Figure 1.4: The lowest order Feynman diagrams contributing to muon production from e^+e^- annihilation.

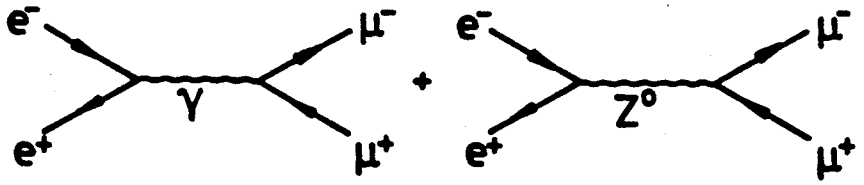

(NC) term and the second is the interference term. The third term is the Breit-Wigner resonance formula which predicts a peak in the cross-section at about $\sqrt{s} = M_Z$. The relative size of this cross-section, compared to the electromagnetic background term, can be computed if the total width (Γ_Z) is estimated by adding up all the contributions of all expected decay channels; this comes out as ~ 2.6GeV which gives $\sigma_{NC} \sim 130 \times \sigma_{QED}$ at $\sqrt{s} = M_Z$. This means the ratio of hadron to muon production will therefore be dominated by the neutral current exchange processes close to the resonance and is expected to be ~ 20.8. The problems of accurate higher order calculations are examined in the next section.

It should also be added that to the extent that the lepton masses may be neglected (a good approximation at this energy scale) the rate of production of electrons, muons and taus from Z° exchange should all be the same in the doublet assignments of the standard model [5]. It should be stressed that this is not a fundamental requirement of the Standard Model in the sense that it is deduced from more basic axioms, but comes about as the result of no experimental observation to date of any difference in the behaviour of electrons, muons and taus that cannot be explained in terms of their different mass values [6]. An

[5]The finite charged lepton mass m_l modifies the partial width Γ_{ll} from being proportional to $(V_l^2 + A_l^2)$ to being proportional to $\sqrt{(1-4\eta)}[(1-\eta)(V_l^2 + A_l^2) + 3\eta(V_l^2 - A_l^2)]$ where $\eta = (m_l/M_Z)^2$. With $m_t = 1.784$GeV and $M_Z = 91.0$GeV, $\eta \sim 0.0004$ which leads to a reduction in the ditau production rate of $\sim 0.25\%$. This kinematic factor is well below the limits of the experimental resolution of this thesis and can be neglected. The modified partial width expression used here is taken from ref. [20] p.492.

[6]As a low energy example the relative decay rate of charged pions to electrons and muons is given by $m_e/m_\mu \times [(m_\pi{}^2 - m_e{}^2)/(m_\pi{}^2 - m_\mu{}^2)]^2 = 1.28 \times 10^{-4}$ assuming universality. This calculation is taken from [20] p.388. With higher order corrections the ratio becomes 1.23×10^{-4} (Berman, 1958; Kinoshita, 1959). The experimentally measured value is $(1.23 \pm 0.02) \times 10^{-4}$ which is in good agreement.

experimental opportunity is available with LEP to test lepton universality at an energy scale $s \sim {M_Z}^2$ and such a study will also be detailed in this thesis.

1.6 Higher Order Corrections

The Z° resonance peak will be modified from its lowest order shape by higher order radiative correction terms. The first order corrections can be divided into two categories; *QED corrections* which consist of those diagrams with an extra photon added to the lowest order diagrams either as a real bremsstrahlung photon or a virtual photon loop and *weak corrections* which collect all other one-loop diagrams. The first category is considered uninteresting with respect to the underlying theory, but due to the size of their effects at LEP energies reliable computation of these is required: the most important is the initial state radiation from the incident e^+ and e^- beams which shifts the cross-section peak up in energy and gives rise to a long radiative tail for $\sqrt{s} > M_Z$. The Feynman diagrams for initial state radiation in dimuon production near the Z° resonance peak are shown in Fig. 1.5.

Figure 1.5: The Feynman diagrams for first order initial state radiation in dimuon production near the Z° resonance.

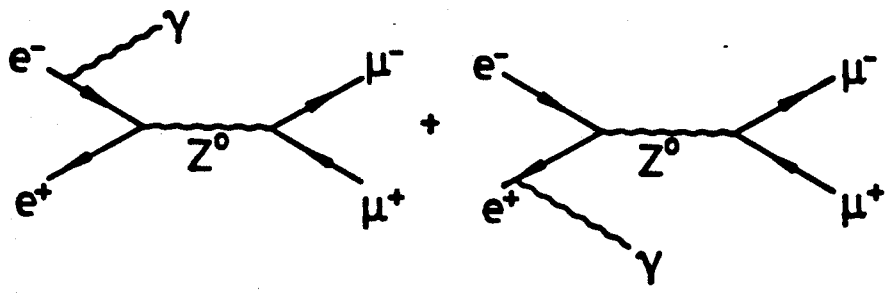

However, although this effect is the most significant for the line shape, it will have little effect on the partial width ratio calculation since for large angle lepton/quark scattering the interference terms between the initial state radiation and the final state particles are small; it will only be important for calculating the correction factors for subtracting off the photon exchange contributions to the relative number of charged leptons and quarks.

The second category includes corrections to the Z° propagator, such as one loop diagrams in the propagator containing quarks, leptons or photons. Because the top quark and Higgs boson can also enter these diagrams there is therefore a small sensitivity to their mass values in the shape of the resonance. Examples of loop diagrams that modify the propagator are shown in Fig. 1.6.

Figure 1.6: Examples of loop diagrams that modify the Z° propagator.

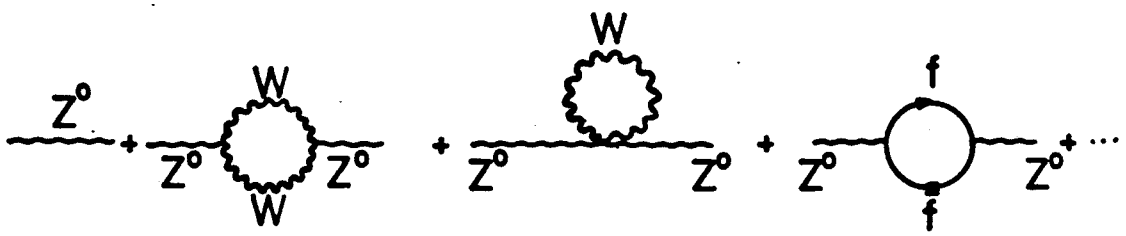

A precise study of the partial width ratios including all of these effects to first order, as well as some second order contributions, can be done with the GAMMAZ program [13] which has an estimated accuracy of 0.1% in calculating the Standard Model partial width values if all the input parameters have been precisely defined. For a constant value of $\alpha_s[M_Z{}^2]/\pi = 0.04$, the charged lepton partial width computed by this program increases by $\sim 2.0\%$ from a value of 20.85 as the top quark mass is increased from 100GeV to 250GeV for a constant Higgs mass of 50GeV and Z° mass of 91.2GeV. There is also a small change of $\sim -0.3\%$ as the Higgs mass is raised to 1000GeV and the top mass is left constant. However, the ratio of partial widths to charged leptons and hadrons remains constant within 0.2%, as the effect of the change in the propagator largely cancels out in the ratio. Therefore the partial width ratio is an important quantity to study since, once $\alpha_s[M_Z{}^2]$ is known, the theoretical partial width ratio is fixed within 0.2% irrespective of the unknown standard model parameters of the Higgs and top mass, and a discrepancy with the experimental values would be an indication of the failure of the standard model.

To summarize - the hadron/charged lepton partial width ratio of the Z° resonance is expected to be about 20.8 in a lowest order calculation (but including

first order QCD effects) and 20.85 when higher order effects are taken into account. The largest error in this calculation is a 1% error due to the uncertainty of the value of α_s at the Z° mass scale; however studies in this chapter show that the uncertainties due to the lack of a top and a Higgs mass value nearly cancel out in the partial width ratio. Therefore, provided α_s can be computed more accurately it will be possible to reduce the error on the theoretical prediction of the partial width ratio below 1%. In fact, it is possible to measure the value of $\alpha_s[{M_Z}^2]$ using hadronic data from the LEP experiments themselves, and the results of one such study are outlined in Chapter 6, together with a more accurate Standard Model prediction of the hadron/charged lepton partial width ratio.

1.7 Experimental Analysis Programme

The determination of the experimental partial width ratio to test the predictions of the preceding sections requires a particle detector designed for the LEP collider and capable of tracking and identifying the decay products of the collisions. The analysis of this thesis is based on data collected using the DELPHI detector which satisfies these criteria and which is described in Chapter 2. Selection cuts, to be applied to event parameters, will be chosen to obtain leptonic events from the general data sample. The resulting event samples will then be scaled up in size to obtain the idealized event numbers in a perfect (i.e 4π solid angle coverage,100% efficient) detector, with a t-channel correction for the Bhabha events [7]. The correction factors necessary to do this will require studies of both real and simulated data.

The final numbers of leptonic events will then be compared to the number of reconstructed hadronic events determined by the analysis of DELPHI team IV, the theoretical photon exchange contribution (the first graph of Fig. 1.4) to the event number ratio subtracted off, and the resulting Z° partial width ratio

[7]Bhabha events are more complex to deal with than other dilepton events in LEP collisions because the resulting particles are indistinguishable from the original ones. As a result in calculating the cross-section there are a greater number of amplitudes to be taken into account; there are electron scattering (t-channel) as well as the annihilation graphs (s-channel). A t-channel correction refers to a multiplicative factor that can be applied to a sample of Bhabha events to obtain the number that would be found if the t-channel contribution could be removed. Once this is applied then the lepton channels can be treated on an equal basis.

compared to the theoretical prediction. The ratio will also be studied as a function of the centre of mass (c.m.) energy across the resonance peak in a search for any systematic variation.

The lepton event generators used with the DELPHI simulation program DELSIM (see Chapter 2) to produce simulated event samples in this analysis are KORALZ [14] for ditau production, DYMU3 [15] for dimuon production and BABAMC [16] for Bhabha production. A comprehensive overview of these generators is also given in ref. [17] Vol.III. The ALIBABA program [21] is used for t-channel subtraction in the Bhabha channel. All these programs calculate at least $O(\alpha)$ radiative corrections and pure electroweak corrections; for the purpose of extrapolating a sample within a restricted angular region of DELPHI up to 4π solid angle their estimated accuracy is much better than 1%, and the limitation will be from the statistics of the generated samples [8]. The exception is the BABAMC generator, because the radiative corrections in the Bhabha channel tend to be larger and because of t-channel particle exchange; BABAMC does not calculate corrections beyond $O(\alpha)$. In this thesis therefore the important task of subtracting off the t-channel Bhabha contribution and extrapolating from the Bhabha sample in the barrel of DELPHI to a sample over 4π solid angle is done by the semi-analytical ALIBABA program; this is the best available computer model of Bhabha production at the time of writing and has an estimated accuracy of $\sim 0.7\%$. The BABAMC generator is only used to produce a simulated Bhabha sample in the barrel region of DELPHI - a task for which the calculation of higher order corrections is not so essential.

The correction for photon exchange to obtain the Z° partial width ratios will be done by the ZHADRO [13] and ZBATCH [13] programs written by G.Burgers. Details of these and comparisons with other programs can be also be found in ref. [17] Vol.III.

[8] Computer processing time is an important constraint. The processing of a KORALZ generated event with full tracking and DELPHI detector simulation takes approximately 1.5min on a Digital Equipment Corporation VAX-8700 computer. The most CPU intensive parts of the simulation are the electromagnetic and hadronic showers and the responses of calorimeters.

Chapter 2

The LEP Collider and the DELPHI Experiment

Preamble

Chapter 2 presents a brief overview of the LEP collider and the design and operation of the DELPHI detector; the main software packages used for DELPHI simulation and the way in which data are structured and processed in the analysis chain are also described. I pay special attention to those components of the detector that are used in the leptonic analysis of Chapter 4, in particular to the design and execution of the barrel muon chamber project as I was closely involved with the calibration, installation and testing of this detector. It should be pointed out that at the time of writing, DELPHI is perhaps the most complex operational particle detector in the world and it is impossible here to give more than a very brief summary. References are, however, provided in the text for further reading.

2.1 The Large Electron Positron (LEP) Collider

The Large Electron Positron (LEP) Collider is designed to collide bunches of electrons and positrons at centre-of-mass energies of up to 100GeV in the first phase of operation, and up to nearly 200GeV in the second phase after the addition of niobium superconducting cavities. It is a circular accelerator with a circumference of 26.658km and it passes at a depth of between 100 and 150m beneath ground level, between the suburbs of Geneva and the foothills of the Jura Mountains. There are currently four bunches per beam and four interaction points which have been equiped with experiments: ALEPH, DELPHI, L3 and OPAL. A diagram showing the layout of part of the LEP collider including the DELPHI and L3 experimental halls is shown in Fig. 2.1. The design luminosity for phase 1 is $1.6 \times 10^{31}\mathrm{cm}^{-2}\mathrm{s}^{-1}$, but the value for most of the 1989 and 1990 running was $0.2 - 0.3 \times 10^{31}\mathrm{cm}^{-2}\mathrm{s}^{-1}$. The length of each bunch is approximately 17mm; when passing through the interaction point at the centre of DELPHI

Figure 2.1: The LEP collider showing the injection system and part of the main ring, including the experimental halls for the DELPHI and L3 experiments.

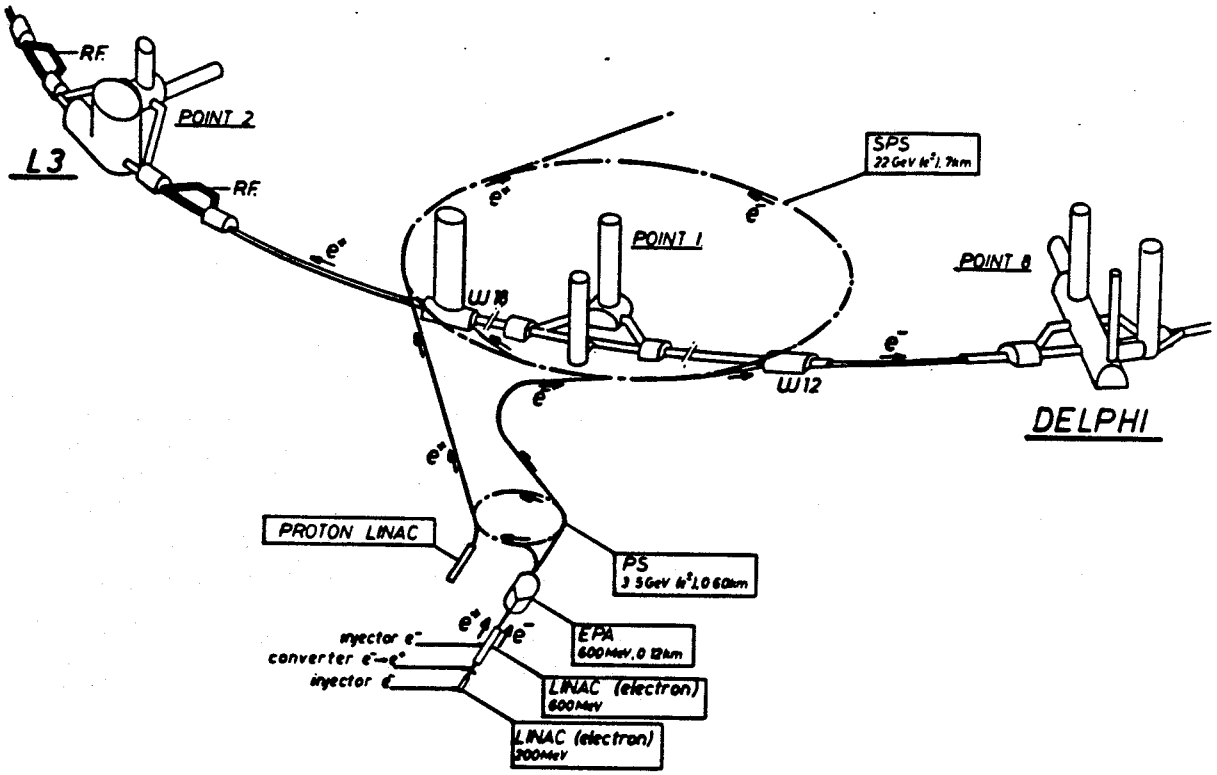

it extends over approximately 15μm vertically and 255μm along the line of a diameter drawn across the ring. This horizontal smearing is a consequence of the momentum dispersion of the beam which gives rise to a smearing of the particle orbits in the bending plane. The accelerator ring has to be large to minimize beam energy losses by synchrotron radiation; the mean energy loss of an electron per turn is given by the formula (see ref. [22])

$$U_0(\mathrm{keV}) = 88.47 \times E^4(\mathrm{GeV})/R(\mathrm{m}), \qquad (2.1)$$

where E is the bunch energy and R is the bending radius of the ring. Consequently for a beam energy of 45GeV nearly 90MeV, or 0.2% of the total beam energy must be supplied per orbit to counteract this loss; in fact the real figure is higher because the addition of straight sections near the experimental halls (to prevent synchrotron radiation flooding the experiments) and the klystron galleries means that the radius of curvature is reduced in the curved sections. The nominal

power output of the klystrons is 16MW; the size of LEP is in fact determined by minimizing total costs due to civil engineering against the operational costs of this massive power requirement which would increase if the bending radius were to be decreased. The collision energy can be measured to an estimated accuracy of ±30MeV. Further information may be obtained from the LEP design report [23].

2.2 An Overview of DELPHI

The DELPHI (**DE**tector for **L**epton **P**hoton and **H**adron **I**dentification) Experiment is situated on the ring of the LEP e^+e^- collider at CERN. It is based on a solenoidal magnetic field of 1.2T and its design is further characterized by hadron and lepton identification over nearly 90% of the full solid angle, fine spatial granularity of all the components and three-dimensional information on every track and energy deposition. The particle identification is designed to be achieved by combining conventional methods, for example the use of electomagnetic and hadronic calorimeters and muon chambers, with ionization measurements in the Time Projection Chamber (TPC) and with velocity measurements based on Ring-Imaging Cherenkov Counters (RICH). The choice of these components also satisfies the requirements for fine granularity and the three-dimensional nature of the collected information.

In order to describe DELPHI in detail it is first necessary to define the coordinate systems used. In Cartesian coordinates the z-direction is defined to be along the beam pipe as it passes through DELPHI, in the direction of the electron beam; the x direction is towards the centre of the LEP ring and y is in the vertical direction. In polar coordinates θ is the angle from the positive z axis and ϕ is the angle in the x-y plane measured anticlockwise (seen from a position of positive z) from the positive x-axis. r is the the absolute distance from the z axis.

A full list of DELPHI detectors and a brief summary of their structure and purpose is given below and Fig. 2.2 shows their general arrangement within the experiment; a full description can be found in ref. [24]. It is worth noting that the detector is split into three major parts; a *barrel* and two *end-caps* that can be retracted for access purposes. The important sub-detectors in the leptonic analysis are explained in greater detail in subsequent sections.

Figure 2.2: The DELPHI detector showing the general arrangement of detector components in the barrel and end-caps.

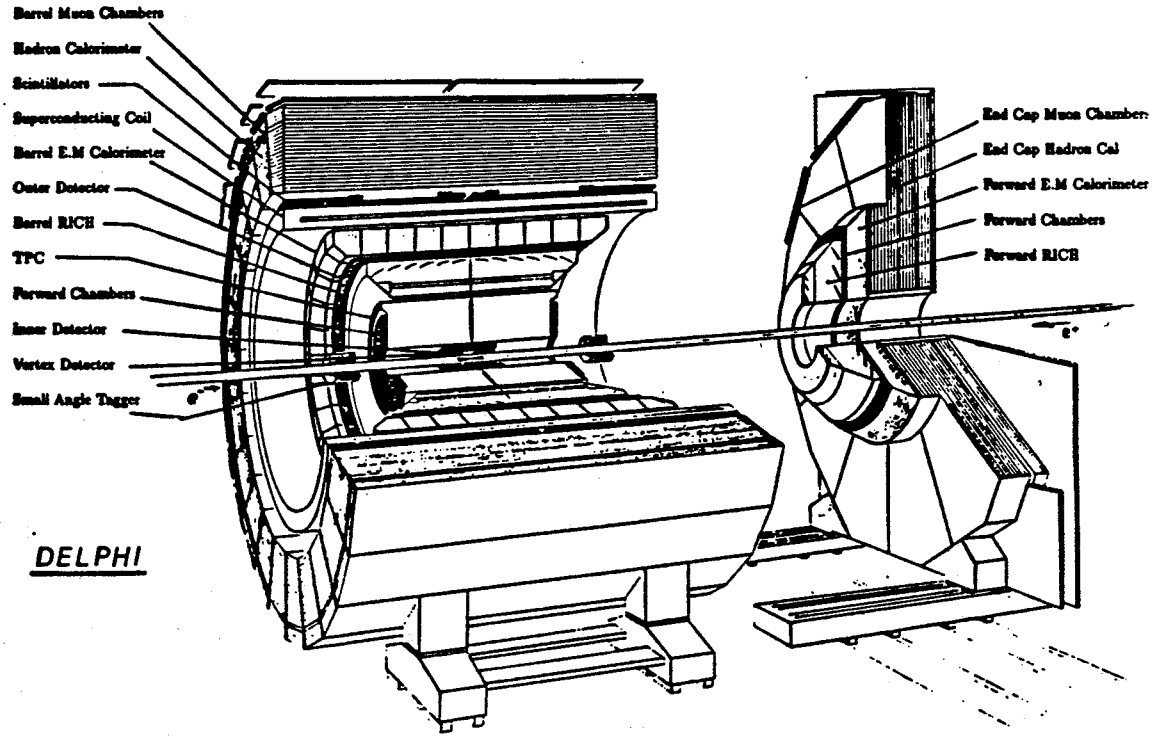

- **Microvertex Detector.** Two concentric shells of silicon strip detectors at average radii of 9cm and 11cm cover the central 24.0cm along the z-axis to provide 5μm single track resolution [1] and $\leq 100\mu$m double track separation in $r\phi$. This detector is designed to be especially useful for heavy flavour physics.

- **Inner Detector.** An inner drift chamber with jet-chamber geometry gives $24 r\phi$ points per track, and five cylindrical MWPC [2] layers provide fast trigger information and resolve the ambiguities from the jet section.

- **Time Projection Chamber (TPC)** . See Section 2.3

- **Ring Imaging Cherenkov Counters (RICH)** [3]. These are designed to utilize the detection of Cherenkov radiation to measure particle velocities

[1] 16μm is the value at the time of writing. Work on the alignment is still under way.
[2] Multiwire proportional chamber.
[3] These are not fully operational at the time of writing

and hence provide extremely good particle identification over most of the momentum range of particles generated in DELPHI. A liquid and gas radiator are used in combination to provide 4.2σ separation for π/K up to 18GeV/c and for K/p up to 33GeV/c in the Barrel RICH. The corresponding figures are 30 and 55GeV/c in the Forward RICH.

- **Outer Detector (OD).** This is composed of 24 modules mounted on the barrel RICH, 4.7m long and each consisting of 145 drift tubes in 5 layers. The layers are staggered and overlap with the adjacent planks thereby providing full azimuthal coverage. It provides fast trigger information in both $r\phi$ and z and improves the momentum resolution when tracks are reconstructed in conjunction with the TPC.

- **Barrel Electromagnetic Calorimeter (HPC).** See Section 2.4.

- **Scintillation (Time of Flight) Counters (TOF).** These serve as fast triggers for beam events and cosmics and may be used to veto cosmic muons during beam crossings. A single layer of 192 scintillation counters is mounted on the inside of the return yoke, just outside the solenoid.

- **Hadron Calorimeter (HCAL).** 20 layers of plastic streamer tubes are inserted into 2cm slots between the 5cm thick iron plates of the segmented magnet return yoke in both the barrel and end-caps. Hadronic showers are generated when incoming particles impact on the iron, and the streamer tubes sample the deposited energy in the layers between the modules.

- **Barrel Muon Chambers (MUB).** See Section 2.5

- **Forward Chambers (FCA,FCB).** These are the equivalent of the OD in the end-caps of DELPHI, and consist of layers of drift chambers providing fast triggers and accurate tracking outside the forward RICH counters.

- **Forward Electromagnetic Calorimeter (FEMC).** This is the end-cap equivalent of the HPC.

- **Forward Muon Chambers (MUF)** . These are the end-cap equivalent of the MUB. They operate, however, in 'streamer' rather than 'proportional' mode.

- **Small Angle Tagger (SAT).** This is the principal luminosity monitor of DELPHI. Each arm consists of a calorimeter and a tracker. The calorimeter covers the polar angles from 43 to 135mrad and consists of alternating layers of lead sheet, 0.9mm thick, and plastic scintillating fibres aligned parallel to the beam. The total thickness is 28 radiation lengths. The tracker is made up of 3 planes of large area silicon detectors at $z = 203, 216$ and 230cm.

- **Very Small Angle Tagger (VSAT).** This is used to make an independent measure of the luminosity. Each arm consists of two rectangular W-Si calorimeter stacks, $24X_0$ deep, 5cm high, 3cm wide and 10cm long mounted at $\pm$7.7m in z to both sides of the elliptical beam pipe. They cover polar angles from 5 to 7mrad. This is also intended to measure the single electron and x-ray background, and to check the orbit calculations for LEP.

2.3 The Time Projection Chamber (TPC)

The TPC is the principal tracking detector of DELPHI and the information it provides normally constitutes the first stage input to pattern recognition algorithms during event processing. It consists of a large cylindrical volume of Ar/CH_4 gas in a 80 : 20 ratio across which an electric field cage sets up a uniform field of nominal strength 150V/cm. The TPC is split into two halves along the $z = 0$ plane in DELPHI; the field in each half pointing towards this plane. Charged particles passing through the volume of gas induce ionization and under the influence of the electric field, droplet shaped clouds of electrons and ionized atoms are formed that drift towards either end of the TPC. The drift velocity is measured to be (66.94 ± 0.07)mm/μs at 22°C under these conditions. The magnetic field is along the same axis as the electric field and has the beneficial effect of causing the electrons to perform helical movements around the magnetic field lines, thereby reducing the transverse diffusion coefficient by a factor of $1/(1 + \omega^2\tau^2)$ ($\omega = eB/m_e$ is the cyclotron frequency of the electrons and τ is the mean free time between collisions). Each end-cap of the TPC is divided into 6 sector plates with 192 sense wires and 16 circular pad rows. The sense wires run perpendicular to a line in the x-y plane through both the centre of

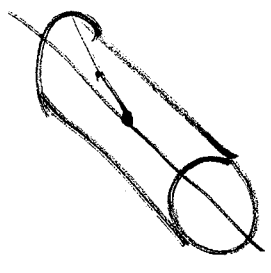

DELPHI and the centre of each TPC segment. The information on the r value is mainly obtained from the wire number hit. The pad rows are 8mm wide and each pad has a length of about 7.5mm. On these pads pulses are induced by avalanches occuring near an anode wire. The magnitude of these pulses varies with the distance between the avalanche and each pad; the centre-of-gravity of the induced charges is used to determine the ϕ position. The arrival time of the drifted electrons is used to fix the coordinate in the z direction and the energy deposited by the charge droplets is used to estimate dE/dx along the length of the tracks and hence provides limited particle identification. The TPC operates at 1atm pressure which, being lower than originally planned, results in a consequent decrease in the resolution of the particle identification. However the DELPHI RICHes (Ring Imaging Cherenkov detectors) promise very superior particle identification which compensates for this and the lower gas pressure results in substantial technical advantages and lower radiation thickness. The reduced dE/dx information is still useful for e-π separation below 8GeV. The size of the TPC is limited (R = 120cm, L = 150cm) by the inclusion of the RICHes and therefore other tracking chambers have been added outside the barrel and end-cap RICHes (the Outer Detector, Forward Chamber A and Forward Chamber B) to improve the precision of the measurement of track curvatures in the magnetic field, and hence the measured track momentum resolution.

2.4 The Barrel Electromagnetic Calorimeter (HPC)

The electromagnetic calorimeter operating in the barrel region of DELPHI is called the HPC (High Density Projection Chamber). The principle of operation is based on the detection of electromagnetic showers caused by the bremsstrahlung interaction of charged particles with the concentrated electric charges of a heavy nuclear material (a *converter*); the high energy photons produced in turn undergo pair production or Compton scattering generating tertiary particles. This interaction is inversely proportional to the square of the incident particle mass, and consequently electrons generate large and distinctive showers, while pions and muons deposit comparatively little energy. The strength of the electron

interaction is such that nearly all of the electron energy is lost in the calorimeter which contains over 18 radiation lengths of material. High energy photons can also be detected by electron pair production which has $\sim 7/9$ of the cross-section of electron bremsstrahlung. The name of the HPC arises from the use of the time-projection principle in the event reconstruction; this is more commonly used in the environment of a central tracking detector and is one of the first instances of its large-scale application in a calorimeter. The secondary particles produced in bremsstrahlung interactions ionize the layers of gas between the walls of the converter material and under the influence of an electric field droplet shaped clouds of ions form that drift to readout pads. The time that they arrive can be used to predict the position of their formation along the drift channel.

The use of this technique enables measurement of the three-dimensional charge distribution induced by electromagnetic showers and by hadrons with a very high granularity in all coordinates, while still keeping the number of required readout channels within acceptable limits. With 18000 electronics channels, a granularity of 4mm along z, 1° in azimuth and energy sampling at nine radial distances along the shower direction ($> 18X_0$ of material) can be achieved. The dynamical range of the detector allows for electromagnetic showers up to about 50GeV while possessing full sensitivity to minimum ionizing particles.

The method of construction is as follows. The converter consists of 41 lead walls spaced by 8mm gas gaps. Each layer is formed by thin trapezoidal lead wires glued to both sides of a fibreglass-epoxy support. A voltage gradient between neighbouring lead wires produces a longitudinal drift field of about 100V/cm. In these narrow drift channels , charge transmission is limited by transverse diffusion which is minimized once the electric drift field in the HPC and the magnetic field in DELPHI are precisely aligned. To adjust to the small radial field component in the magnet, each HPC module can be tilted by up to ±5mrad to optimize transmission. For fast triggering purposes a plane of scintillators is inserted into one of the HPC sampling gaps close to the shower maximum (behind $4.5X_0$). There is a 7.5cm gap in the modules at $z = 0$ caused by a stiffening ring inside the cryostat; this zone is covered by scintillator/lead sandwich blocks providing crude shower information.

2.5 The Barrel Muon Chambers (MUB)

2.5.1 General Description

The DELPHI Barrel Muon Detector has been designed and built by a team of people from the Nuclear Physics Laboratory at Oxford University. It is made up of 1372 sub-units called *drift chambers*. A standard chamber consists of an extruded aluminium casing with external dimensions of $2.0 \times 20.8 \times 365.0$cm, 2 nylon endplugs with electronics protruding 0.7cm into the chamber and 5.0cm out of the chamber, and an internal volume of a gas mixture of $85.5\%Ar, 6.0\%CO_2$ and $8.5\%CH_4$ (see Fig. 2.4). The gas is passed through the chamber at an rate of $\sim$ 10cm^3/sec . Two plastic sheets, each measuring $0.25 \times 20.0 \times 365.0$cm^3 are glued onto the largest inner surfaces of the chamber. Thin parallel copper strips running the length of the chamber are glued onto the plastic at equidistant intervals; these are called the cathode grading strips.

The sensing devices consist of a single 47μm gold plated tungsten anode wire running through the centre of the chamber and a delay line which is glued onto one of the plastic sheets, parallel to the anode wire.

The standard configuration of electrical potentials is a linear progression from zero (earth) to $+4000V$ on the grading strips moving towards the centre of the chamber and a potential of $+6150V$ on the central anode wire. This gives a nominal field gradient of 400V/cm within the chamber.

The principle of operation is as follows [4]. When an energetic charged particle passes through the gas of a drift chamber a discrete number of ionizing collisions take place which liberate electron-ion pairs. Liberated electrons with an energy larger than the ionization potential of the gas can then go on to generate secondary pairs. In the absence of an electric field, these charges would quickly lose their energy in multiple collisions and attain the average thermal energy distribution of the gas. Under the influence of the electric field, two things happen. Firstly the electrons substantially pick up energy between collisions. Secondly a net movement of electrons and ions in the direction of the electric

[4]For a very good general description of the principles of operation of drift chambers see ref. [31]

field takes place. In a simple formulation, due to Townsend (see ref. [32]), this mean drift velocity can be expressed as

$$v_d = (e/2m)E\tau \tag{2.2}$$

where E is the electric field strength, m is the electron mass, and τ is the mean time between collisions. When the electron wavelength approaches that of the electron shells of a molecule the value of τ can change rapidly due to complex quantum mechanical effects (this change is named the Ramsauer Effect). The net result can be that v_d remains nearly constant over a substantial range of E. The drift chambers are operated within this range for the gas mixture used as their drift parameters are therefore less sensitive to small geometric fluctuations in field strength. The practically uniform electric field causes a drift of liberated electrons towards the centre of the drift chamber at a near constant speed. At the centre of the chamber is the anode wire. The field geometry around the wire is such that the field increases as $\sim 1/r$, where r is the distance from the wire centre, in the region close to the wire surface. In this region, once the mean energy gained by the electrons between collisions begins to exceed the ionization potential of the gas, a chain reaction is set up in which there is a large multiplication in the number of liberated electrons. This is called an *avalanche*. The time development of this process is shown in Fig. 2.3.

The electrons produced are collected by the anode wire within $\sim$ 1nsec. The positive ions liberated in the avalanche then form a cloud of positive ions that drift towards the cathode. It is the result of this migration of charge *away* from the anode that causes a pulse in the anode potential. This signal propagates to the end of the wire at $\sim$ 17cm/nsec and is electronically amplified and fed into the read-out system. The pulse is also echoed in the delay line along which two *slow* ($\sim$ 0.44cm/nsec) signals propagate to either end of the chamber. These three signals, the anode, the near and far end delay line signals constitute the maximum information delivered by a drift chamber after the passage of a particle. They are related to the time the particle went through the chamber by,

$$\begin{aligned} t_a &= t_0 + t_{drift} + t_{ap} \\ t_{dln} &= t_0 + t_{drift} + t_{dlnp} \\ t_{dlf} &= t_0 + t_{drift} + t_{dlfp} \end{aligned} \tag{2.3}$$

Figure 2.3: Time development of an avalanche around the anode wire. A single primary electron proceeds towards the anode wire, in regions of increasingly high fields, experiencing ionizing collisions; due to the lateral diffusion, a drop-like avalanche, surrounding the wire develops. Electrons are collected in a very short time (~ 1nsec) and a cloud of positive ions is left, slowly migrating towards the cathode. This migration induces an electrical pulse on the anode wire. Source ref. [31].

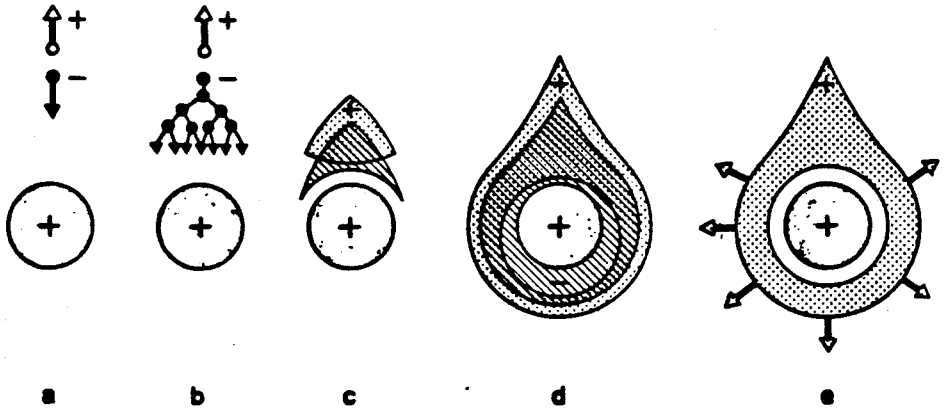

where t_a,t_{dln},t_{dlf} are the three recorded times that the signals reach the ends of the chamber, t_0 is the time of the particle passage, t_{drift} is the drift time and t_{ap},t_{dlnp},t_{dlfp} are the signal propagation times in the anode and delay line. If the time the particle went through the chamber and the chamber drift and delay line parameters are known, the position of the particle where it passed through the plane of the chamber can be calculated. However, one further piece of information is needed because there is still a 2-fold ambiguity regarding which side of the anode wire the particle hit took place since the chambers are symmetric along the line of the anode wire. The solution is to use staggered chambers and compare the hits in adjacent layers. Three signals coming from the same event in a drift chamber are called a **triplet**. If one signal is missing the other two are called a **doublet**. A triplet of signals are constrained by the equation

$$t_{dln} + t_{dlf} - (2 \times t_a) \approx t_{dlnp} + t_{dlfp} = T_{dl} \tag{2.4}$$

where T_{dl} is the total delay line propagation time which is a constant for a particular chamber. This characteristic signal combination, also called a **time sum**, can actually be used to identify the correct set of signals if there is an ambiguity in signal reconstruction arising from the multiplexing process

(see Section 2.5.2), to test whether a chamber is correctly operational and to distinguish random noise.

The drift chambers are assembled into *modules*. These modules are wrapped around the DELPHI Barrel in three concentric layers namely, the inner, outer and peripheral layers, as shown in Fig. 2.4.

The modules in the inner layer contain 14 drift chambers stacked in 3 layers $(5 + 4 + 5)$. The outer and peripheral modules contain 7 chambers stacked in 2 layers $(4 + 3)$. It should be pointed out that the inner layer of modules is embedded in the hadron calorimeter at a depth of 20cm (approximately one hadronic absorption length) from the outer surface. The peripheral modules are designed to cover the gaps left by the outer chambers. The total percentage of the solid angle covered by drift chambers within the angular range $50° \leq \theta \leq 130°$ is 87.4% (evaluated by simulation). The major contributions to the dead space come from the central gap around $\theta = 90°$ and the gaps between the inner modules as seen by a particle projected from the centre of DELPHI in the angular regions $50° \leq \theta \leq 60°$ and $120° \leq \theta \leq 130°$.

It is worth discussing the choice of gas mixture briefly as the final choice reflects an important balance of priorities and was the outcome of several months of research (see ref. [33]) . Argon is used because avalanche multiplication occurs at lower field strengths than in polyatomic molecules with many non-ionizing energy dissipation modes. Argon is also safe and relatively cheap. However it cannot be used on its own without entering into a permanent discharge mode (like a fluorescent light bulb) since photons are emitted when argon atoms which do not actually ionize in an avalanche return to ground state. The minimum energy of the emitted photon in argon is 11eV while the ionization potential for copper of the cathode is 7.7eV. These photons are therefore capable of liberating electrons which can initiate a new avalanche. A new gas component, a *quencher* is needed to 'mop up' these photons.

For the MUB no single additional gas could be found to meet the DELPHI specifications, and in the end the Oxford group chose a combination of 8.5%CO_2 and 6.5%CH_4. A pure CO_2 quencher has several problems. First of all the shallow HV plateau can lead to significant changes in the drift velocity if the grading

Figure 2.4: The DELPHI barrel muon chambers, showing the arrangement of modules around DELPHI, the structure of modules and the internal structure of individual drift chambers.

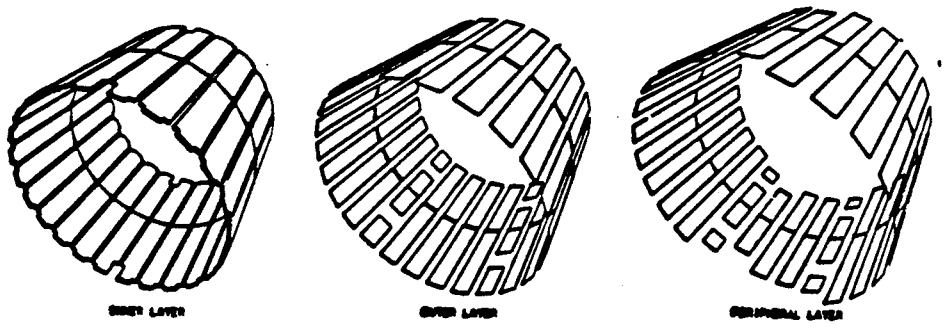

The Distribution of the Muon Chamber Modules in the DELPHI.

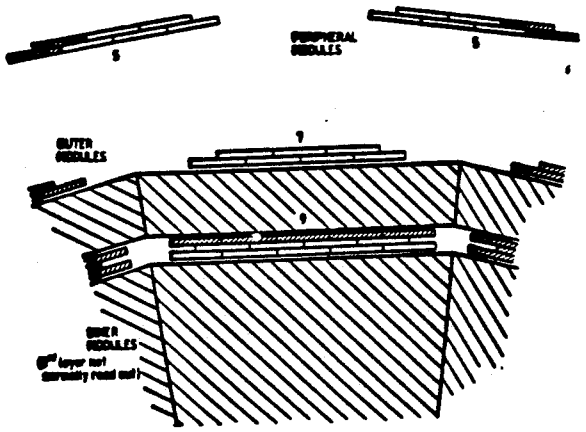

The Arrangement of the Barrel Muon Chambers in Modules.

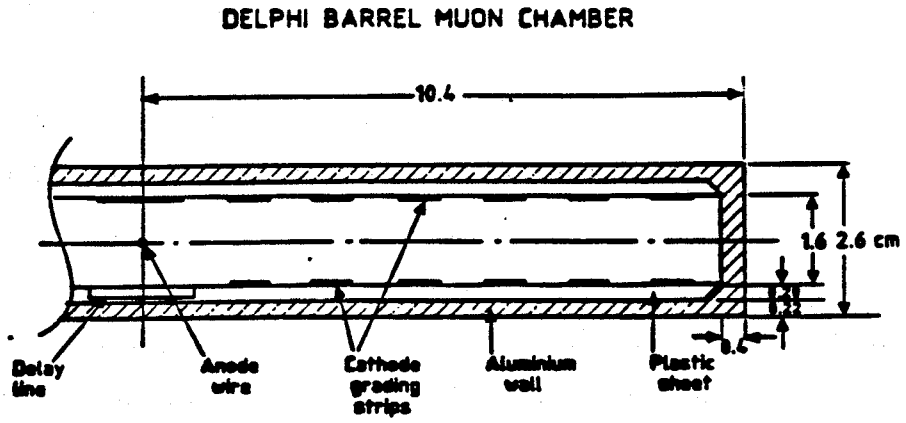

potentials change. Secondly, the plateau itself is at a low drift velocity for CO_2 and leads to unacceptably long drift times that fall outside the specifications of the first level trigger in DELPHI. On the other hand a pure CH_4 quencher increases the rate of deposition of polymerized products on the wires of the drift chambers (a problem that becomes worse with heavier hydrocarbons), and a mixture containing more than 7.0% CH_4 is potentially explosive in air. This is unacceptable, as the barrel muon chambers are in an exposed position in DELPHI and contain a very large number of gas connectors. Therefore the final choice was a mixture of the two gases giving a drift plateau with a velocity of $\sim 4.7\text{cm}/\mu\text{sec}$ - well within the specified tolerance; it is also safe, comparatively cheap and with it the aging of the chambers by polymer deposition will be slow enough for them to last the projected lifetime of the experiment.

2.5.2 The MUB Readout and Slow Control Systems

The three signals from each muon chamber are amplified and fed into a solid state latch system that registers which chamber channels in an event have received signals. These latches are reset at the end of each event. The information is stored as a bit pattern in a memory buffer called the HLB (**H**it **L**atch **B**uffer) and is read out in a ZEBRA data blocklet (see Section 2.7) at the end of each event. The signals from the chamber then pass though a multiplexing system and into digital timing devices called LTD's (**L**EP **T**ime **D**igitizers). The multiplexing system exists for economic reasons; the LTD's are expensive and since the signal rate is so low there is no need to have a 1-1 mapping of chamber signals and LTD input channels when each LTD channel is capable of recording multiple signals during an event.

Each LTD channel is mapped to 6 different MUB input channels which are distributed over the barrel in such a way that it is exceptional for more than one of these channels to receive signals during one event. Unscrambling of the data is done later with reference to the HLB output. An input clock pulse of 117.5Mhz is fed into the LTD's and timing is achieved by recording the number of clock pulses before receiving a STOP signal on an input channel; an additional solid state interpolator (effectively a 2,4,6 and 8nsec delay box) built into them

gives an overall resolution of $\sim$ 2nsec. As mentioned above the LTD's can also record multiple pulses on a single channel during an event, have a dynamic range of 32.7μsec, and are fully compatible with the other FASTBUS (see Section 2.6) units in the DELPHI DAS system. The data they supply are in the form of ZEBRA blocklets of the form shown in Fig. 2.5. The first three words contain the

Figure 2.5: The LTD data blocklet showing the makeup of the 32-bit words that carry the MUB timing information. The hit pattern and timing data words are marked; see text for details.

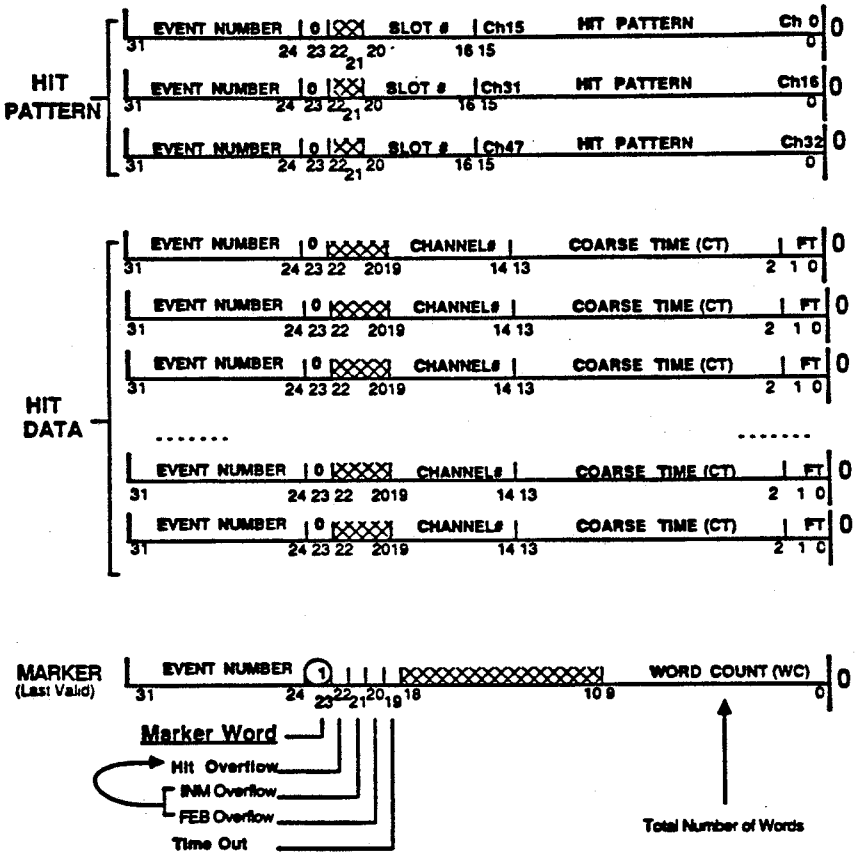

LTD hit pattern, which summarizes which channels have received signals. There is also a marker word at the end of the blocklet recording the total number of data words that should have been present; this may be cross-checked against the actual number. The main body of the data blocklet contains between zero and 48 words recording the times (in terms of input clock pulses) that signals were received on the input channels since the clocks started, and which channels registered hits. The timing words themselves are divided into coarse times, measured in terms of number of input clock pulses, and fine times which record the 2nsec time divisions

from the interpolator. Extensive cross-checks are performed by the MUONLINE program (see Section 3.3) on all the redundant information contained in these data blocklets, such as between the hit pattern and the hit data words.

The flow of data from the HLB and the seven LTD's for each side of the barrel is controled by a local FASTBUS data manager called a FIP (**F**ast **I**ntersegment **P**rocessor). The data flows from the two sides of the DELPHI barrel are then integrated by a FASTBUS LES (**L**ocal **E**vent **S**upervisor) and finally fed into the data stream from the rest of DELPHI; this is shown in Fig. 2.6.

The high voltage supply to the muon chambers is provided by the programmable C.A.E.N. [5] system, and is designed to trip off the high voltage in a muon chamber sector if the integrated dark current in the sector surges too high (above $1\mu A$). During running the overall number of trips per unit time tends to decrease steadily; this is compatible with the characteristic property of drift chambers working in proportional mode to burn off internal dust and contaminants. If a sector trips a high voltage control program written by A.Romaya at Oxford automatically ramps it up to full voltage again, with safety checks on the current, within 4 minutes .

The gas supply to the muon chambers is also monitored by a control program which sends a signal to the C.A.E.N system to ramp the chamber voltages down in the event of a change in gas composition, a failure of gas supply or a large discrepancy between input and output gas flows to a sector of muon chambers.

2.6 The DELPHI Data Acquisition System

The objective of the Data Acquisition System (DAS) is to read out data from the individual sub-detectors at each beam crossing, store these data in memory while the trigger system decides whether to keep the event, and then to draw together the separate data blocklets into a single ZEBRA record (see Section 2.7) to be written onto magnetic tape. As all the DELPHI sub-detectors have different response and read-out times a large fraction of the messages passed between the components of the system are cross-checks to determine whether each sub-detector system is successfully reading out data and to keep the readout

[5] Costruzioni Apparecchiature Elettroniche Nucleari S.P.A

Figure 2.6: A schematic diagram showing the components of the MUB data acquisition system and how information is transferred among them. The flow of data from the muon chambers is picked out in a hatched style. A full description of this system can be found in DELPHI note 88-92 DAS 90.

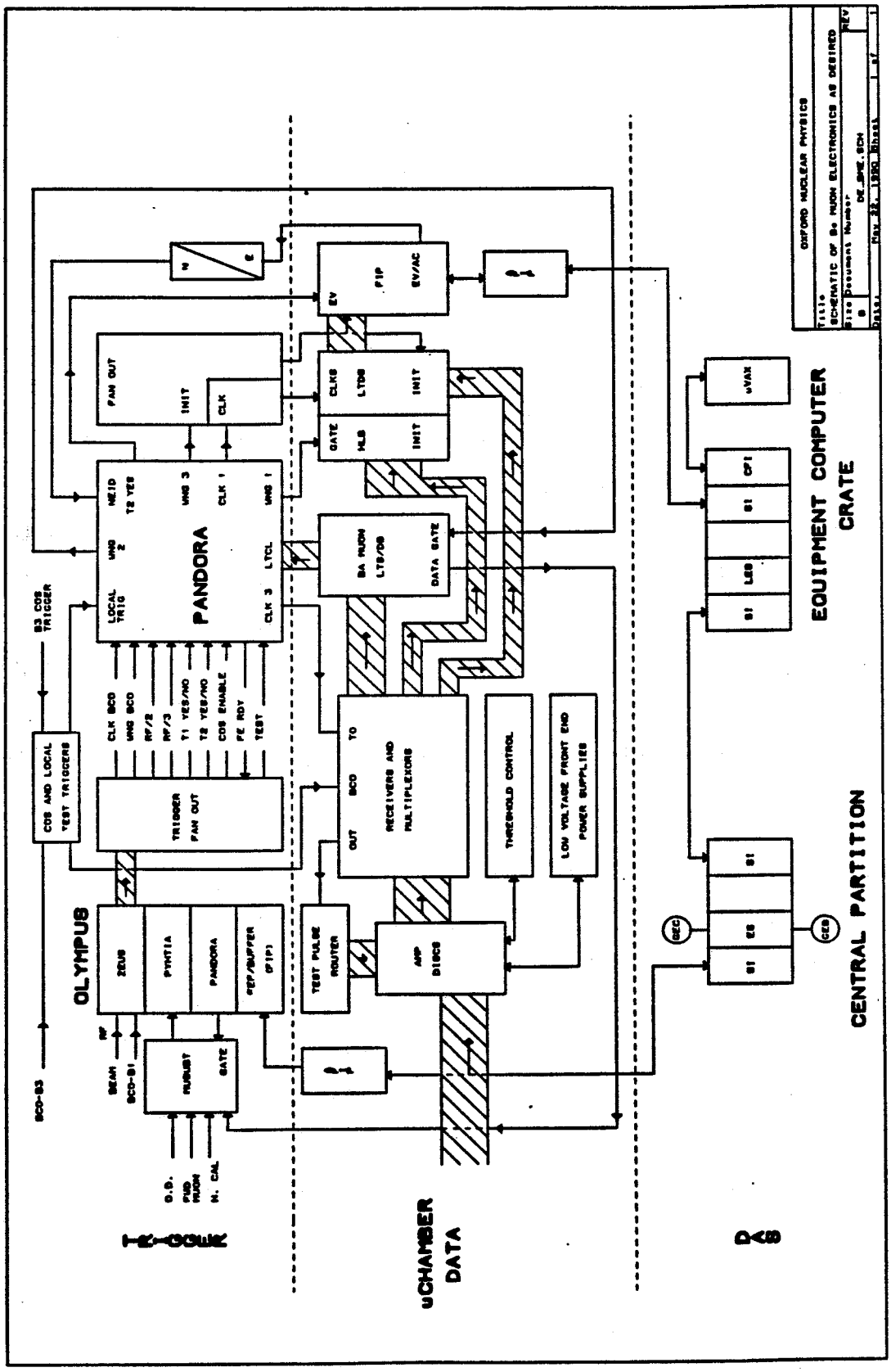

operation coherent; this prevents a situation arising whereby one detector is out of step and is reading out the signals from a different event to the others. If a single component fails like this, all readout is automatically inhibited until the problem is resolved. FASTBUS is the information transfer and processing system used and is a relatively new standardized system for high energy physics experiments (see ref.[34]). It is a modular data-bus system consisting of multiple bus segments that can operate independently, but link together for passing data and other information. An important characteristic of the system is therefore that processing power and database information is distributed rather than centralized. The DELPHI DAS system can be envisaged as a large number of linked but self-contained read-out systems; each one assigned to a particular sub-detector. As an example of this, a schematic diagram of the barrel muon chamber sub-system is shown in detail in Fig. 2.6. Each self-contained system can be operated independently of the main readout if, for example, a problematic sub-detector needs to be tested without interfering with the primary data taking. FASTBUS has a 32-bit address and data field and a typical duration for the transfer of information between units of the same bus-segment is of the order of 100nsec in DELPHI. The readout time for an entire event in DELPHI is limited by the response time of the detectors rather than the FASTBUS transfer time.

2.7 DELPHI Data Management and Analysis

The set of routines that is used to process the raw data, whether real or from simulation, is called DELANA (for **DELPHI Analysis**); this is described fully in ref. [27]. The stages in this analysis are closely linked to the way the data are managed in DELPHI which is explained below. It should be noted that DELANA is highly modular, thereby ensuring that software development is carried out in a structured and safe way. In addition the different DELPHI teams provide the subroutines for analysis of data coming from the sub-detectors for which they are also responsible.

A diagramatic outline of the principal steps involved in the processing of the raw detector data is shown in Fig. 2.7; a description of these steps is given below.

Figure 2.7: A diagramatic summary of the principal steps involved in DELPHI data processing. The RAW DATA consist of ZEBRA banks (see text) of digitized detector signals. The TANAGRA data are subdivided into six bank types of increasing association of particle signals from different detectors into tracks and vertices. The DST data contain the event summary including the final results of particle identification.

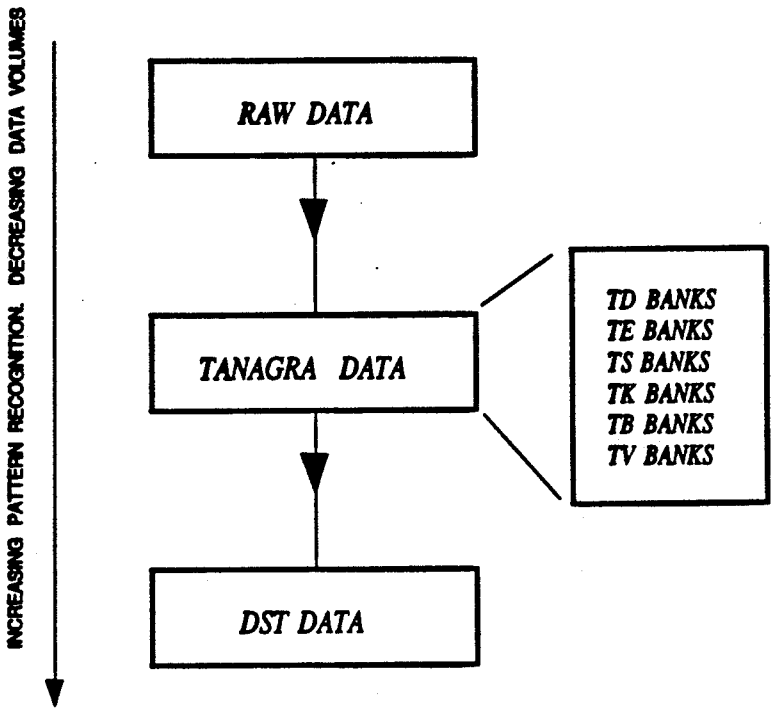

For data management DELPHI makes extensive use of the data structure program library known as ZEBRA (see ref. [28]) which was developed at CERN. Its principal use is in allowing flexibility during execution in the length of an array in memory allocated to a particular use (e.g for storing the data for an event from one of the DELPHI sub-detectors). This is achieved by storing the data in a single vector array and assigning some of its values to be *pointers* i.e they point to the addresses of particular pieces of data elsewhere in the array. This is the key feature of ZEBRA, allowing dynamic data storage where the address of a data structure is not determined according to a preset plan. This enables a program written in FORTRAN, by accessing ZEBRA, to emulate a feature of C software.

Individual logical data structures are called *banks* and these are arranged in

hierarchical fashion. In DELPHI what is called the *partition master bank* contains the addresses of the detector banks - with the data for each sub-detector. These may in turn contain addresses of other banks holding convenient sub-units of data.

ZEBRA provides the basic data storage framework at three different stages in the acquisition and processing of data in DELPHI. First of all the *raw data* from the detectors are arranged in ZEBRA format with the data from individual detectors being stored in assigned blocklets accessed by a hierarchy of pointers from the partition master bank. This raw data structure for the MUB is shown as an example in Fig. 2.8. Secondly, it is used after first stage processing by the offline analysis program DELANA. Here a special program library called **TANAGRA** (see ref. [30]) has been developed by the DELPHI collaboration which sits 'above' ZEBRA. Its importance to DELPHI is such that it is worth explaining this package in some detail. TANAGRA stands for the Track Analysis and Graphics package. It has several purposes:

- to provide a 'backbone' for the off-line analysis programs, making sure that the information which is relevant for physics analysis is stored in a precisely defined way.
- to provide an interface between the event and the interactive analysis system flexible enough to cope with the specific requirements of this type of work.
- to allow the data to be easily updated. If the software of a given detector component is improved, results from an earlier version can be removed and the new results inserted and integrated with the rest of the information independently i.e without re-running the rest of the detector software.
- to provide reasonable data protection by checking for inconsistencies and testing whether interventions by users are permissible at each stage in the processing.

The TANAGRA data structure is itself organized into a hierarchy of data types. As the DELANA analysis progresses the data at each level are *reduced* in physical size but represents an increasingly sophisticated level of pattern recognition. The list of the data types serves to illustrate this.

Figure 2.8: The structure of the raw data blocklets generated for the MUB. The address of the MUB data is stored in the partition master bank (PMB). This points to a list containing the addresses of the crate event buffers (CEBs); one for each side of the barrel. These in turn contain the addresses of the data blocklets for each of the seven time digitizers (LTDs) which hold the timing information for channels with signals, and the address of the hit latch buffer blocklet (HLB) which contains the list of all the MUB channels registering in the event.

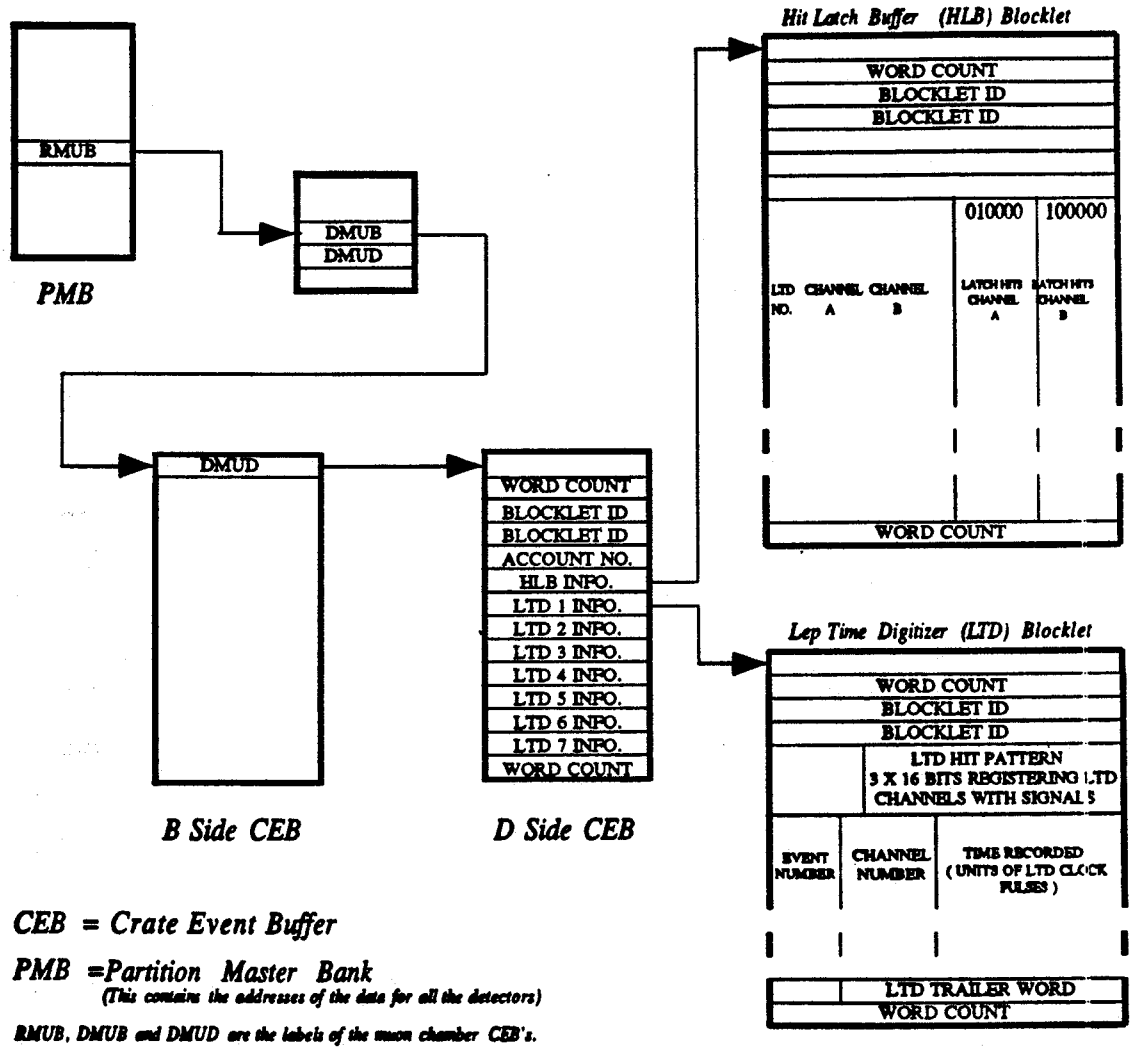

- **Detector data (TD banks)**: this is the most primitive type of TANAGRA data. They are the output of the detector software modules in DELANA operating on the raw data to produce space points (for tracking detectors) or clusters and pulse heights (for calorimeters) in the local ge-

ometry frame of the sub-detectors.

- **Track elements (TE banks)**: these are information banks in a form which allows their subsequent combination into track banks. The *type* of data varies according to the sub-detector. In the TPC, for example, the TE's describe short tracks formed from the analysis of the previously generated TD banks which describe single hit points. In the MUB the TE's describe space points in the DELPHI coordinate system, but where an attempt has been made to sort out the left-right ambiguity of hits in single drift chambers by comparing these with hits in adjacent layers of chambers.

- **Strings (TS banks)**: these banks are the result of collecting track elements together into 'strings'. They consist of lists of track elements compatible with being signals from single charged tracks, or fragments of these tracks. However, if a situation arises where multiple solutions are possible to the track search, TANAGRA allows all concurrent solutions to be kept at this stage.

- **Tracks (TK banks)**: at this stage of data processing by DELANA the strings are combined and the most probable original track solutions are stored in TK banks.

- **Bundles of tracks (TB banks).**: a list of tracks that may have originated from the same vertex are stored by TANAGRA as a list called a TB bank; any track may be included in more than one bundle.

- **Vertices (TV banks)**: starting from one or several bundles of tracks, a global vertex fit is performed by DELANA to determine both the vertex position and the track parameters at the vertex. At this processing level the ambiguities and contradictions existing for the bundles are required to be resolved. After the vertex has given a successful fit, a kinematics fit can be performed to improve the track parameters further. TANAGRA stores these final results in TV banks.

The third stage of analysis during which a ZEBRA data structure is used is in the formation of **DST's** or **D**ata **S**ummary **T**apes. At the time of writing the DST structure is less well defined than the TANAGRA structure, but it represents the ultimate reduction in data to the important essentials and will eventually be the only form in which long term data storage can take place. The DST structure consists of one or more ZEBRA banks containing primary or secondary vertex information. Pointers corresponding to each track from a particular vertex point to separate data banks where the information for that track is stored. As well as information about angles and momenta of tracks, information is also stored about the final decision from each relevant sub-detector concerning the kind of particle that formed the track. To be able to trust these decisions requires an accurate calibration of each sub-detector which is currently an ongoing process within DELPHI. For the leptonic analysis of this thesis the TANAGRA data are supplied to a specially written DST program called GEDTAN which contains only very basic initial assumptions about how the sub-detectors are functioning. This is explained in greater detail in Chapter 4.

2.8 DELPHI Simulation Programs

The operation of the DELPHI detector is simulated in a program called DELSIM (for **DELPHI Sim**ulation) (see ref. [25]). It is designed so that the response of the detector to physical interactions may be tested and used to serve as a reference to the events coming from real life. The DELSIM software is divided into four main parts.

- Physics Simulation: physics routines are available to generate most of the predicted interactions at LEP, for example the string fragmentation model from the Lund group (see ref.[29]) for modelling quark fragmentation. External event generators provided by the user may also be used. The information about the characteristics of the generated particles is stored in a ZEBRA data structure (see Section 2.7).

- Detector Description: a package of routines track particles through the detector and produce secondary interactions in the material.

- Detector Simulation: this is an interface to the detector software which treats the behaviour of the particles in the detector components in detail and produces space points and electronics signals. Subroutines to simulate the behaviour of a particular detector component are provided by the same group responsible for building that component.

- Output Routines: the output, from the detector dependent software, is converted into the form in which it appears as raw data in a real data taking situation.

A great deal of flexibility on the control of the running conditions is available to the user. The event generator, types of secondary particle decays, geometrical distributions of generated particles, and detailed tracking of particles through particular sub-detectors are examples of changeable options. Minimal tracking of particles through the detector includes a track following routine with multiple scattering and energy loss only. The following secondary processes can also be switched on: delta rays, bremsstrahlung, pair production, Compton scattering, particle decays, nuclear interactions, positron annihilation and the photoelectric effect.

The full simulation of an event in DELPHI is extremely time consuming; most of the time being spent in the detector simulation modules. For some situations the required level of accuracy in the detector simulation is not so stringent. Therefore a program called FASTSIM (for **Fast Simulation**) has also been developed (see ref. [26]). It uses the same event generation routines as DELSIM but has special simplified routines for particle tracking and detector simulation. It is suitable for use in those situations where the exact details of secondary processes and detector response are not required.

Chapter 3

Calibration and Testing of the Barrel Muon (MUB) Detector

Preamble

This chapter details calibration work done on the barrel muon chambers, the testing of the components of the MUB detector and read-out system in the HFM test-beam experiment in August 1988, and the design and operation of the online system analysis program for which I was responsible (MUONLINE) in the final installed detector in DELPHI. Finally a calculation is made of the level of background noise in the MUB detector.

3.1 Cosmic Ray Calibration Work

The Barrel Muon Chambers were manufactured at the Oxford University Nuclear Physics Laboratory over the period from 1986 to 1988. A cosmic ray test rig was set up to calibrate them; once a chamber was constructed it was put into the rig to determine its drift and delay line parameters. The layout of the rig is shown in Fig. 3.1.

A coincidence trigger was generated using the layers of scintillators at the top and bottom of the rig, while 25 chambers whose properties were already determined and stable were used to provide position information on the cosmic rays. Over the course of several runs, the parameters of the chambers under test were gradually refined until the positions of the tracks matched those extrapolated from the calibrated chambers.

The drift distance (D) for each particle track is assumed to vary as

$$D = a_0 + a_1 t_{dr} + a_2 z_{pos} t_{dr} + a_3 t_{dr}^2, \tag{3.1}$$

where t_{dr} is the drift time and z_{pos} is the displacement along the delay line direction. The reconstructed z_{pos} is assumed to vary as

$$z_{pos} = b_0 + b_1 T + b_2 T^2 + b_3 T^3, \tag{3.2}$$

Figure 3.1: The layout of the muon chamber cosmic ray test rig. The drift and delay line parameters of the test chambers are obtained by comparing the reconstructed positions of cosmic ray tracks to those obtained from the the calibration chambers and then improving these iteratively.

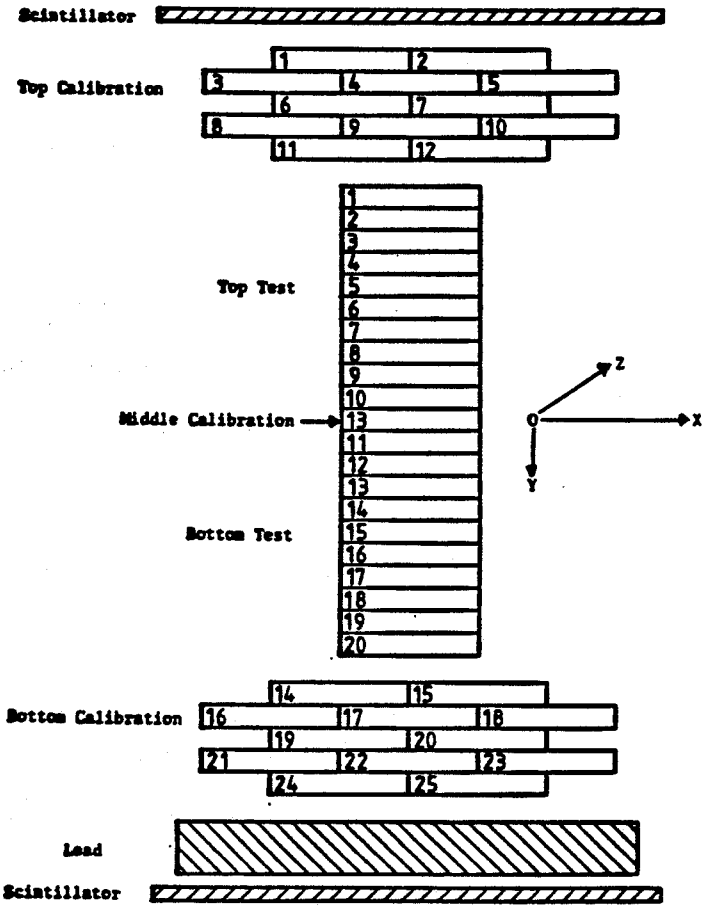

where

$$T = (t_2 - t_3)/2 \tag{3.3}$$

and t_2 and t_3 are the delay line times recorded at either end of the chamber.

For both expressions, the linear (constant velocity) components always make the dominant contributions; the mean drift speed is 4.7cm/μsec while the mean delay line propagation speed within the chambers is 0.44cm/nsec. However the delay line propagation speed depends on the capacitance of the delay line with the chamber wall which in turn depends on their relative separation. This cannot be guaranteed to be accurate to better than 1mm in the manufacturing process, and

thereby introduces the non-linear components. The drift speed is also non-linear in the vicinity ($\leq$ 2cm distant) of the anode wire.

The average drift speed was found to vary inversely with air pressure in the test rig as expected by the theory. There were also two general parameter changes that took place over several months. Firstly the drift speed increased to reach an asymptotic value, and secondly the linear change in the drift speed *along* the length of the chamber - the slope of which was dependent on the gas flow direction - was slowly reduced to zero. These observations are compatible with the theory of a contaminant that is slowly flushed from the chamber after manufacturing. Although a spectroscopic analysis was carried out on the chamber gas the contaminant could not be identified, although a hydrocarbon vapour emitted from the glue used in the manufacturing process was considered as a possibility.

The discovery of this long term time dependence demonstrated the need to re-calibrate the drift parameters in situ after installation in DELPHI. This is an on-going task at the time of writing. However, by observation of the calibration drift chambers that had been in the test rig for two years it was found that the final drift speed settled down to a constant from chamber to chamber within 0.2% and a constant in time in the same chamber within 1.0% [1]. This shows that the use of a universal drift constant for a large number of chambers can be a good approximation if insufficient statistics are available for individual chamber calibration.

3.2 The HFM Test Beam Experiment

A large scale test of components of three of the DELPHI detectors was carried out in the North Area of CERN over July and August 1988. Modules of the forward electromagnetic calorimeter (FEMC), the endcap hadron calorimeter (HCAL) and the barrel muon detector (MUB) were placed in the H6 beam which provided tertiary pion and positron beams of momenta 10, 20 and 40GeV/c. Beam halo muons were also present at a contamination level of between $\sim$ 50%

[1] This indicates that the parameters of different chambers at a particular time are highly correlated, as might be expected since they share the same gas supply and are subjected to the same atmospheric pressure.

at 40GeV/c and $\sim$ 200% at 10GeV/c. The experiment, originally proposed by Dr. A. Segar, became known as the HFM Experiment after the names of the component detectors; the experimental configuration is shown in Fig. 3.2.

Figure 3.2: The HFM test beam experiment.

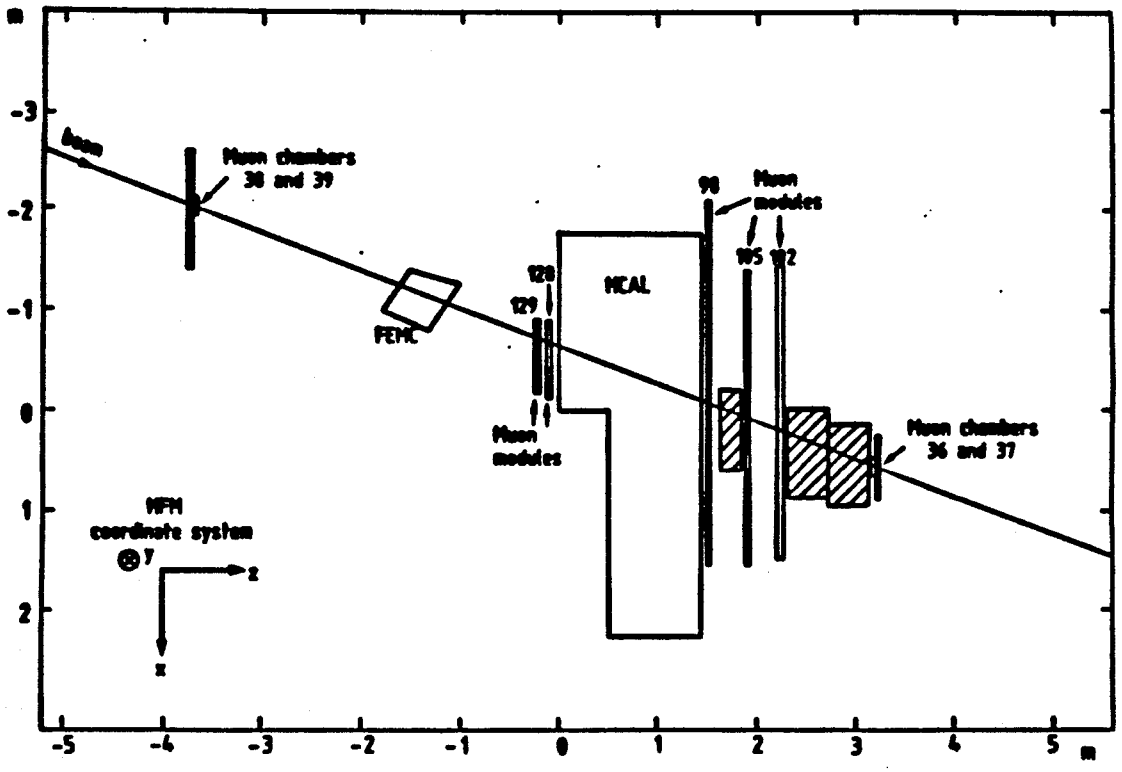

The detectors intercepted the beam in the order FEMC, HCAL and MUB. The MUB detector was split into a module of chambers behind the HCAL, followed by a further 20cm of iron and then two more modules. This corresponded to the order of inner, outer and peripheral modules in DELPHI. Two more sets of muon chambers were also added; one placed upstream to fix the incoming particle track and one placed downstream of the rest of the experiment and behind a further 80cm of iron. This constituted a muon veto shield to positively separate muons from pions.

A full report of the analysis and results of the experiment can be found in ref. [35], so only a brief summary is presented here. The aims of the experiment were as follows:

- to investigate the performance of components of the DELPHI data acquisition system in the environment of a real physics experiment: the LTD time digitizers; the front-end electronics; the FASTBUS readout software and on-line monitoring programs.

- to test and calibrate the response of the two calorimeters to particles of different types and energies,

- to estimate the rates of hadronic contamination of the muon signals, and to improve the rejection efficiency of hadronic punchthrough by using the particle identification capabilities of HCAL,

- to investigate further ways of improving the particle identification algorithms.

The results of the experiment were as follows:

- A problem with the transfer of LTD data in the FASTBUS system was found. For some LTD's, the least significant four bits (up to the 16nsec bit) were being logically ORed with a random bit pattern during data transfer. This degraded the position resolution of tracks along the delay line direction and was found to be due to a software fault in the FASTBUS system; this was corrected subsequently in the DELPHI software.

- There were problems with the muon chamber data. First of all, the drift velocities turned out to vary from the values calculated in the test rig back in Oxford; they were typically 25% slower. In addition, some extensive afterpulsing appeared. The primary signal from a chamber would be followed by several echoes [2] ; it is important to note that this effect was significantly reduced when the muon chambers were operational in DELPHI

[2]The time delays between subsequent pulses were of the order of 200nsec (though with a considerable fluctuation of $\sim \pm 100$nsec about this value). The hypothesis was that the drifting electrons were exciting gas molecules in the avalanche region close to the anode; upon de-excitation these were generating U.V. photons that were striking the cathode strip and liberating photo-electrons from the copper. These photo-electrons were then drifting to the anode and initiating a new avalanche. This led us to believe the cause of the problem was an incorrectly balanced gas mixture which reduced the ability of the gas to absorb the excess photons. A study of this effect has been done for the Oxford group in [36].

a year later. This underlined the importance of recalibration of the drift parameters in situ. Although the gas supplied was the same as that for the test rig in Oxford, insufficient purging of the chambers may have been the cause.

- Using the veto shield for muon identification the experiment showed that $3.2 \pm 1.1\%$ of 10GeV/c pions, rising to $10.5 \pm 0.6\%$ of 40GeV/c pions could give rise to signals in both layers of the first module of muon chambers. $2.9 \pm 0.3\%$ of 40GeV/c pions could also generate signals in the second module, behind the additional 20cm iron block. These were identified as muons using a simple algorithm based on counting hits in layers. When the distribution of energy deposited in the HCAL was folded into the identification procedure, the percentage of hadronic contamination dropped from $2.4 \pm 1.0\%$ at 10GeV/c to $0.14 \pm 0.07\%$ at 40GeV/c in the first module, and from $< 1.5\%$ at 10GeV/c to $< 0.2\%$ at 40GeV/c (at the 90% confidence limit) in the second module as well. This underlined the advantage of combining the muon chambers, whose mis-identification rate is low at low energy, with the hadron calorimeter whose mis-identification rate is low for high energy particles. The HFM setup did not correspond to the precise setup in DELPHI but demonstrated that hadronic contamination would probably be significant at the 1-2% level.

- Angular discrimination was also tested as a means of reducing pion background. The fact that pions are more likely to be scattered through large angles than muons in the iron can be used in a veto procedure. However, although a sample set of distributions were examined that confirmed this, the experimental setup was too crude to allow a precise study.

In conclusion, all of the aims of the experiment were realized to a degree. However, as the experimental setup only crudely corresponded to the final DELPHI configuration of these detectors, the physics results could only be regarded as partially relevant to the final system. However many operational improvements were made to the DELPHI DAS system as a result of this experiment and one of

the most useful additional benefits was the opportunity for the people involved to gain experience of DELPHI equipment operating in a real experimental environment. Much of the experience gained of using software for fault diagnosis in the HFM experiment was used in planning and writing the muon detector online analysis program MUONLINE described in Section 3.3 below.

3.3 MUONLINE Online Data Analysis Program

The DELPHI barrel muon detector, as described in Section 2.5, consists of 1372 drift chambers with 3 data channels per chamber, front-end electronics to read these, a signal multiplexing system, 14 LTD's and local FASTBUS computers to control the data flow. MUONLINE, which stands for Muon Chamber Online Analysis, is designed to rapidly diagnose faults in this complex system to ensure that the barrel muon detector operates with high efficiency. The program is designed to reconstruct hits in the muon chambers in a similar way to the offline software and many of the subroutines are identical; however as the objective is *system analysis* rather than *data analysis* a large number of diagnostic facilities have been added; these, together with the operational history and results are detailed in the sub-sections below.

3.3.1 Method of Analysis

MUONLINE is a stand-alone program that can be run in both offline and online modes; an outline of the data processing is given here and the major steps of the analysis are shown schematically in Fig. 3.3.

Data are supplied by the MUB DAS system in a series of ZEBRA data blocklets (see Section 2.7). On each half of the barrel one data blocklet summarizes the information from the HLB (see Section 2.5.2), while seven data blocklets store the information coming from each of the seven LTD's. These data blocklets are either supplied in the form of a file on disk when running in offline mode or is accessed directly in the memory of a DEC μVAX computer when running in 'spy' (online) mode. A diagram of an LTD data blocklet is shown in Fig. 2.5 in Chapter 2. Once the different blocklets are located in the

Figure 3.3: Diagramatic representation of the MUONLINE data analysis program.

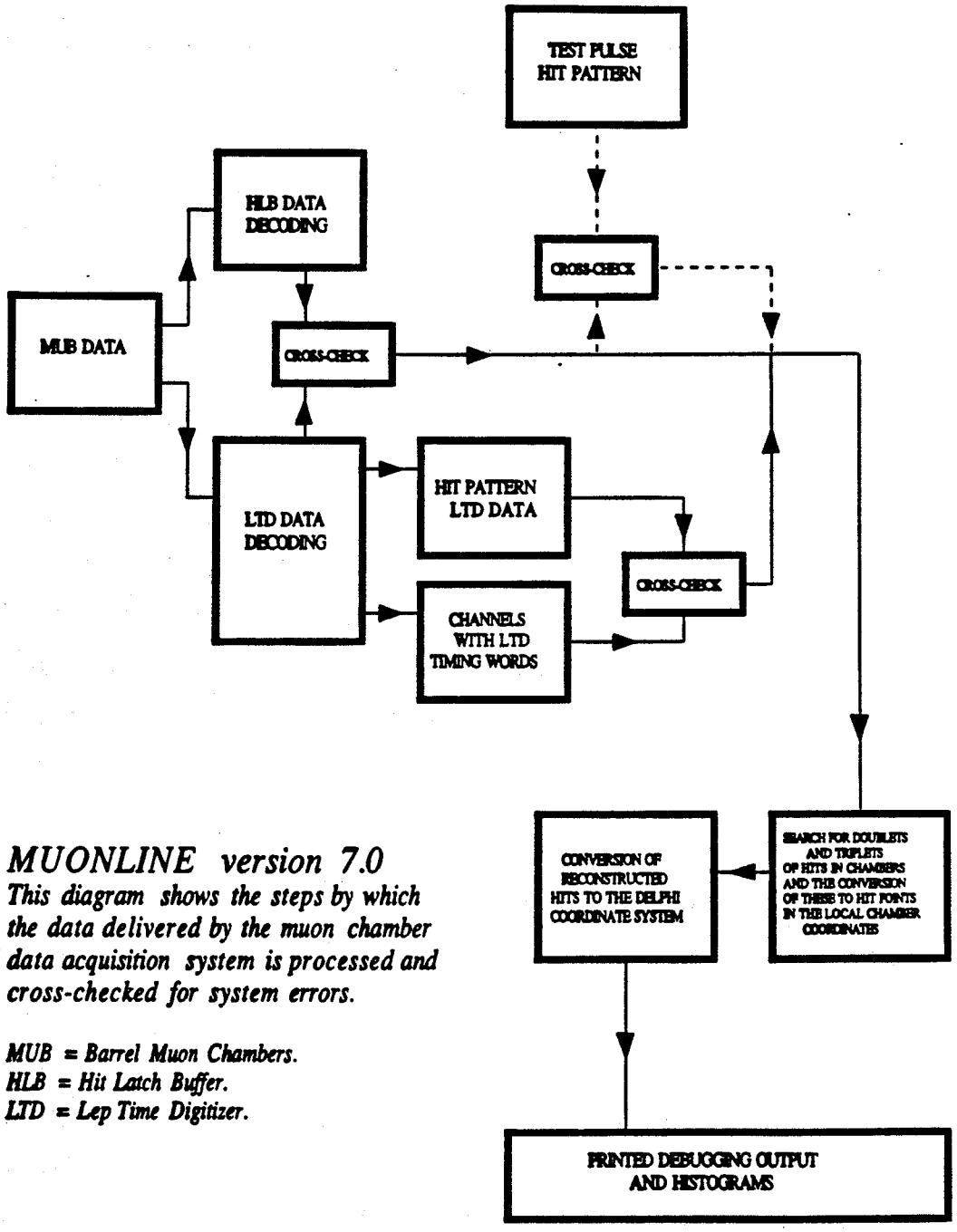

MUONLINE version 7.0
This diagram shows the steps by which the data delivered by the muon chamber data acquisition system is processed and cross-checked for system errors.

MUB = Barrel Muon Chambers.
HLB = Hit Latch Buffer.
LTD = Lep Time Digitizer.

data stream, separate subroutines process the HLB and LTD data. The HLB blocklet contains a large bit pattern indicating unambiguously which channels of which muon chambers received hits, while each LTD blocklet contains a small bit pattern indicating which channels of the LTD have received signals, and data

words containing the times at which the signals were received since the start of the clocks. Since the signals to the LTD channels are multiplexed an attempt is then made to match up HLB hits with hits on LTD channels to create a list of muon chamber channels with hits with the corresponding times these were received.

A search is made for triplets and doublets of signals (see Section 2.5.1) from individual chambers (each one should supply up to three signals after the passage of a particle) and if there is ambiguity in the LTD data because of the multiplexing, the time sum condition of Equation 2.4 is used to find the correct signal combination. Once the full timing information from each muon chamber is known, the database parameters measured from the cosmic ray test rig (see Section 3.1) are used to determine the particle track positions. However an ambiguity remains concerning which side of the anode wire the particle passed; the information from hits in adjacent layers of muon chambers is used to resolve this ambiguity, and the hits are converted to space points in DELPHI coordinate space.

During the course of this processing diagnostic algorithms are in operation to locate system faults; these are outlined in Section 3.3.2 below.

3.3.2 Diagnostic Facilities

Four techniques which are employed in the identification of system faults are listed below:

- cross-checks of all data supplied to the program whenever there is redundancy;
- comparisons of the behaviour of identical system units (e.g sectors of muon chambers, time digitizers) during the course of a run;
- comparisons of the run-to-run behaviour of system units to identify time-dependent variations;
- measurements of the response of the system to controlled input signals.

MUONLINE's cross-checks are made possible because any chamber signal should set an HLB bit, an LTD hit pattern bit and generate an LTD data word; LTD errors show up for example when the hit latch buffer records hits but the LTD data word is missing. Errors of this kind are recorded in 2-D histograms of LTD number and LTD channel number on the y and x axes of the plot, in order to identify errors common to one LTD or a particular set of channels; an example is shown in Fig. 3.4.

Figure 3.4: A MUONLINE diagnosis histogram of one type of signal loss in the MUB readout system. This shows HLB hits that are missing the corresponding LTD data words over a long cosmic run plotted on a 2-D histogram of LTD number against LTD channel number. This type of plot is invaluable for finding patterns in particular types of faults - for example a large number of problems in the same LTD. Missing HLB hits are only plotted here if they can be matched up with two others as coming from the same muon chamber. This reduces the contribution of any random background noise.

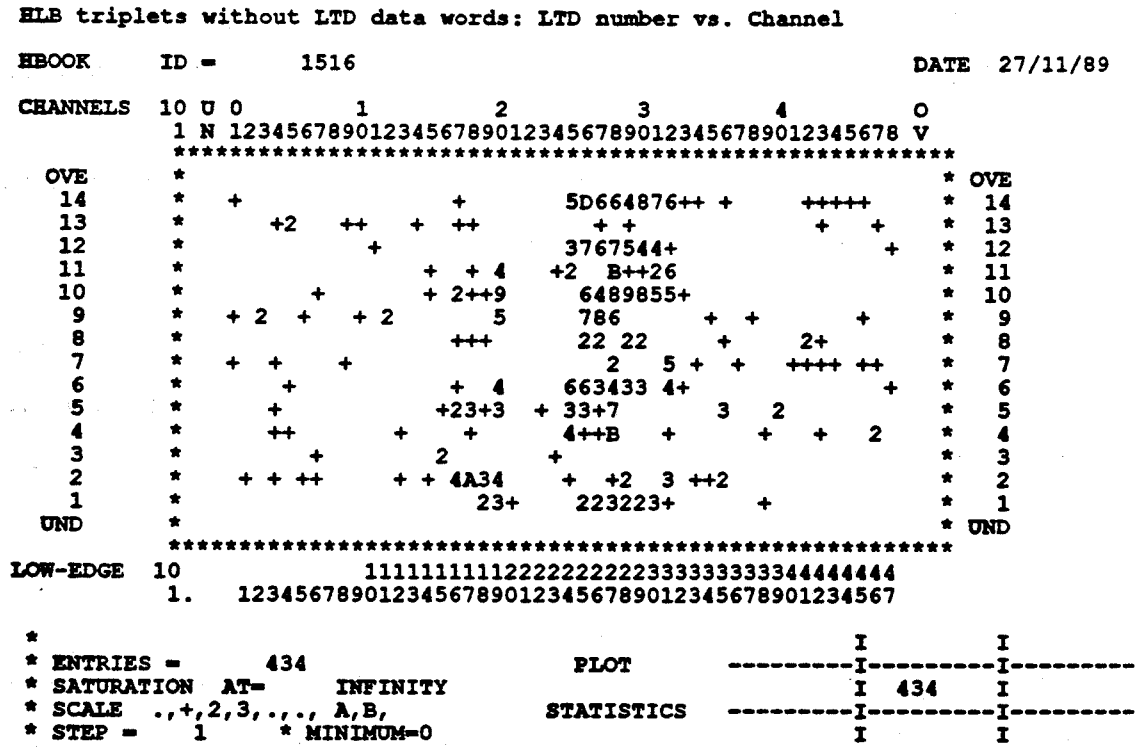

Comparison studies of the behaviour of identical system units include plots such as a 1-D histogram of the number of hits recorded versus muon chamber sector number, and the total number of LTD timing words plotted on a 2-D plot of LTD number versus LTD channel number. All the 2-D plots in this category

are automatically scanned whenever a run summary is printed and a warning message is printed if the total number of hits on a channel differs from the mean value by more than three standard deviations. Other comparison histograms in this category are **bit distribution histograms** of an LTD, either the integrated distribution for the whole digitizer or for individual channels. The principle applied here is that each bit of a time data word should be set for 50% of the time if the measured times are random. Therefore a histogram where each channel represents each bit should be flat with a height equal to half the number of data words in each LTD in a run; deviation from this behaviour indicates a digitizer malfunction.

A compact summary of the results of MUONLINE processing is printed on the completion of its analysis of a run. These summaries enable rapid run-to-run behaviour comparisons of system characteristics to be made.

Two kinds of controlled input signals may be supplied to the system. A known pattern of input signals can be fed into the front end electronics and made to pass through the entire analysis chain during a special run; this **test pulse** system was constructed by J.Bibby and M.Flinn. The output may be compared by MUONLINE to the input pattern and warning messages printed in the event of discrepancies. The missing signals are also plotted on 2-D plots of LTD number versus LTD channel number. A second controlled input which operates during ordinary running is a signal fixed in time relative to the BCO (beam crossover signal) that is fed to the first channel of the first LTD on each side of the barrel during every event; failure to detect this signal signifies failure in the read-out system.

Diagnosis reports can be generated at regular intervals during a run, and the stages in the processing of each event can also be printed over a user-selected event range for detailed studies; a labelled example is shown for one event in Fig. 3.5.

To complete this overview Tables 3.1 and 3.2 summarize the diagnostic facilities of MUONLINE and the main objectives of each type of analysis.

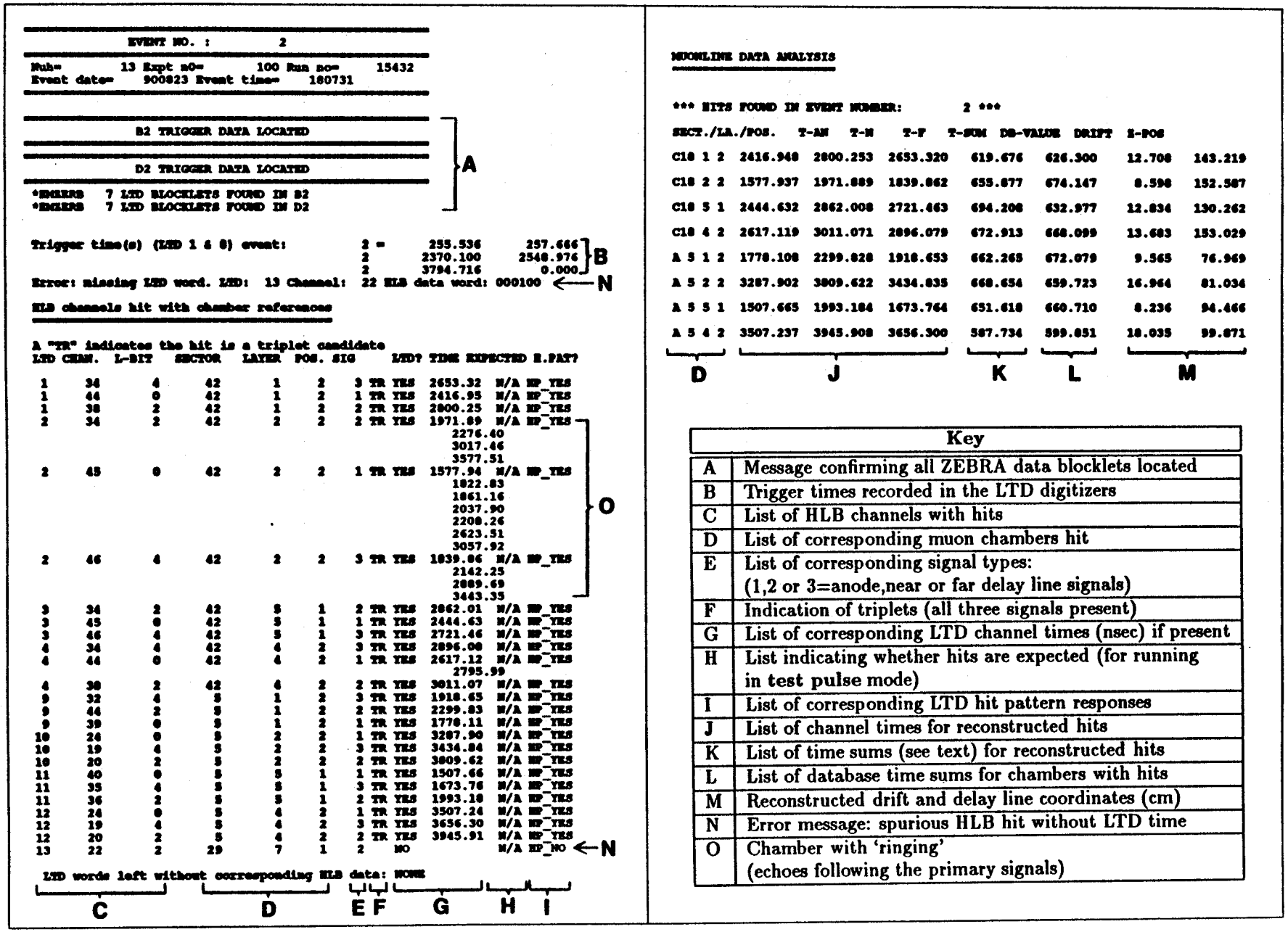

Key	
A	Message confirming all ZEBRA data blocklets located
B	Trigger times recorded in the LTD digitizers
C	List of HLB channels with hits
D	List of corresponding muon chambers hit
E	List of corresponding signal types: (1,2 or 3=anode,near or far delay line signals)
F	Indication of triplets (all three signals present)
G	List of corresponding LTD channel times (nsec) if present
H	List indicating whether hits are expected (for running in test pulse mode)
I	List of corresponding LTD hit pattern responses
J	List of channel times for reconstructed hits
K	List of time sums (see text) for reconstructed hits
L	List of database time sums for chambers with hits
M	Reconstructed drift and delay line coordinates (cm)
N	Error message: spurious HLB hit without LTD time
O	Chamber with 'ringing' (echoes following the primary signals)

Figure 3.5: MUONLINE diagnosis output for one event.

Table 3.1: Diagnosis histograms supplied by MUONLINE.

Category	Descriptions	Objectives
Digitizer	Global bit distribution histograms; individual bit distribution histograms for user-selected channels; 2-D plots of LTD number versus channel showing the the total number of timing data words, and the number of hit pattern hits recorded.	Fast diagnosis of LTD malfunction.
HLB	2-D histograms recording the total number of HLB hits on different channels; separate equivalent histograms for doublets and triplets of signals coming from the same physical chamber; and a histogram for unassociated signals.	Fast diagnosis of HLB malfunction; identification of high random noise channels.
Discrepancy	2-D plots of LTD channel versus LTD number: HLB hits without LTD data; LTD hits without HLB bits set; LTD hit pattern hits without data times; HLB triplet hits and LTD hit pattern bits both set without LTD data times.	Identification of system data discrepancies.
Test pulse	2-D plots of LTD channel versus LTD number: channels hit but not expected by the test pulse input pattern; test pulse input signals unrecorded by the system; time delay histograms between input test pulses and output signals.	Identification of cabling errors; electromagnetic interference between read-out channels; LTD/HLB failure; measurement of cable delays.
Sector	Number of reconstructed hits versus sector number (1-50); 7 histograms of the number of hits versus sector number for layers 1-7; number of sectors fired per event.	Identification of muon module or sector malfunction.
Time sum	Plots of $t_{dln} + t_{dlj} - (2 \times t_a)$ for each muon chamber (*taken over many runs*).	Identification of broken connections to chambers or cabling errors; chamber calibration.
DELPHI hit position	Plots of reconstructed hits in the x-y plane and z-R space of DELPHI.	Identification of muon module or sector malfunction.
Total hit number	A plot of the total number of reconstructed hits per event when the number exceeds zero - dimuon events give ~ 6.7 hits per event.	Identification of run-to-run changes in system behaviour.
Echo	Afterpulsing (echo) studies: number of afterpulses versus sector number; time delay between primary and echo signals.	Identification of sector gas contamination.

3.3.3 Operational History and Results

Three stages may be defined in the operational history of this program and the muon detector it is designed to analyze:

- **Phase 1:** MUB installation and commissioning (April-August 1989);

Table 3.2: Non-histogram diagnosis available with MUONLINE

Name	Description	Output	Objectives
Event debug	Summary of the data of an event at different stages of processing (see Fig. 3.3 for an example).	Printed over a user-selected range of events.	Detailed check of data processing chain.
Data blocklet debug	A display of the ZEBRA blocklet output of the HLB's and LTD's in binary format.	Printed over a user-selected range of events.	Detailed check of raw data blocklets.
Run diagnosis reports (general information)	Run summary including number of events with data on either side of the barrel; listings of any LTD bit parity or overflow errors.	Printed at the the end of a run, and every N events; N is a user-selected number.	General system check.
Missing 'warning BCO' signal count (BCO = 'beam cross-over)	The 'warning BCO' signal is fed into the first channel of the first LTD on each side of the barrel for *every* event; if this is missing the DAS is malfunctioning.	Printed in run diagnosis reports	Identification of read-out system failure.
Automatic histogram scanner	Scans histograms of HLB hits and LTD hits searching for channels with hit numbers more than 3σ from the average value.	Warning message in run diagnosis report.	Fast diagnosis of LTD/HLB malfunction.

- **Phase 2**: MUB calibration and early running (September-October 1989);
- **Phase 3**: stable running (from November 1989);

During phase 1, the installation and commissioning phase, the test pulse system was used to supply input signal patterns to the front end electronics as the read-out equipment became operational. These data were processed by MUONLINE to identify cabling faults and component failure, and by August system faults of this type, with the exception of two dead channels, had been reduced to zero.

During phase 2, the early running period, several subtle problems were identified. The front-end chips of the LTD's change state at a high rate (every few nsec) and dissipate considerable heat; a single LTD generates $\sim$ 0.1kW in total. Occasionally one of the chips failed in a localized heat build-up during the early running. This fault was identified by the rate of filling of some of the time bins dropping to zero in the bit distribution histograms. The acceptance time gates of the LTD's and the HLB's also differed marginally at first which resulted in data

sometimes appearing in the HLB's but not the LTD's until this was resolved. An internal discrepancy was also manifest in the LTD's as the LTD hit pattern sometimes recorded data hits without the LTD timing data words appearing; this data loss, running initially at (3.6±0.4)%, vanished when the polarity of the input clock pulses was reversed. However, despite these difficulties, which were quickly resolved, many other aspects of the system worked extremely well from the start. The level of random system noise was, and to date remains extremely low, as Table 3.3 shows. This shows that 97.6% of the data in the HLB for this example

Table 3.3: An analysis of signals appearing in the Hit Latch Buffer (HLB) for a sample run 6224 (December(1989)). Triplets and doublets are signals that can be identified with others as coming from the same muon chamber.

Signal Type	Number	% Of Total
All	13107	100.0
Triplets	12426	94.8
Doublets	366	2.8
Singlets (*mainly background noise*)	315	2.4
Singlets (*excluding the worst channel*)	179	1.4

run can be grouped into triplets or doublets of signals identified as coming from the same physical muon chamber. The level of additional background noise is therefore very low, and 43% of this in fact comes from a single channel (LTD 13, channel 22, latch bit 2). This table also shows that in 97.1% of the muon chamber data all three signals (anode, near and far delay line) are picked up (a minimum of an anode signal and one delay line signal are needed for particle position reconstruction).

During phase 3, the period of stable running, the main objective was to rapidly identify sudden faults, such as a digitizer chip failure. However a long term analysis was also carried out using time sum histograms - plots of $t_{dln}+t_{dlf}-(2\times t_a)$ (see Equation 2.4) for each muon chamber; two of these are shown in Fig. 3.6. This required accumulated statistics over several weeks of running. Since this expression should yield a nearly constant value for any muon chamber, these plots were used to track down instances of chamber failure and broken cable

Figure 3.6: Calibration work with MUONLINE: The signal combination (see Equation 2.4) $t_{din}+t_{dif}-(2\times t_o)$, which should be nearly constant for a particular chamber, is plotted for two example chambers with the December 1989 data.

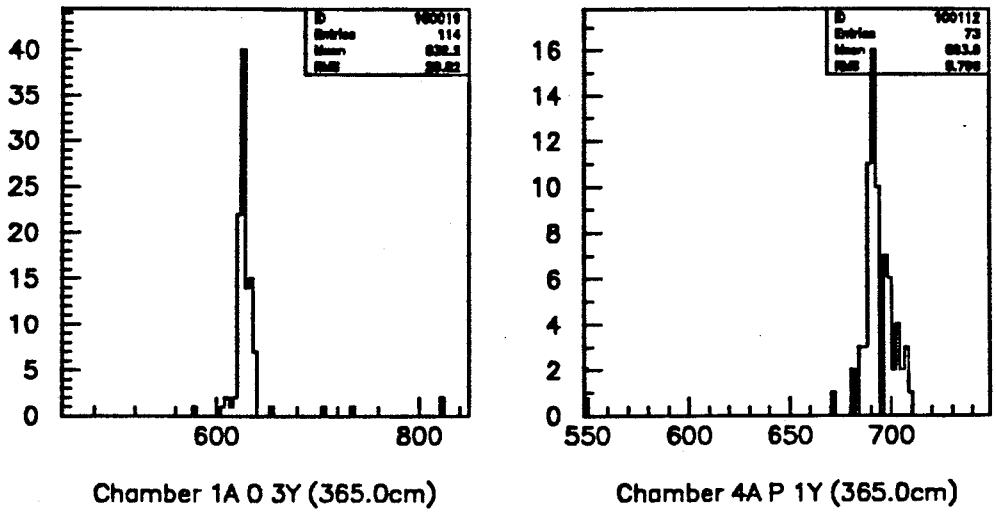

connections. These were repaired during the winter shutdown (January - March 1990)

Certain measurements of the MUB performance require combined information with other DELPHI detectors; for instance a measurement of the overall muon detection efficiency in a leptonic analysis. These cannot be done with the MUONLINE program; however with MUONLINE it is possible to diagnose the individual system faults that contribute to the overall inefficiency figures.

3.4 Chamber Noise Calculation

An estimate of the total noise in the MUB system over the 1989 running period was made in the following way using the leptonic data sample and the GEDTAN program of Chapter 4. Events were selected with two charged tracks and scanned for MUB hits that were more than 0.3rad in ϕ in a straight line extrapolation from either track; the results are shown in Table 3.4.

A total of 34 noise hits were counted using this method. It should be noted that these were distributed uniformly around the barrel. Assuming a statistical error of 5.6 on the figure of 34 in 408 events, the estimated number of noise hits

Table 3.4: Reconstructed MUB hits associated and unassociated with tracks in a two-track event sample from the 1989 data.

Number of two track events	408
Number of events with MUB hits > 0.3rad in ϕ from either track	33
Total number of MUB hits > 0.3rad in ϕ from either track	34
MUB hits within 0.15rad in ϕ	1412

that would have fallen *within* the acceptance region of ± 0.15rad is

$$\frac{2\pi}{2\pi - 1.2}(34 \pm 5.6)\frac{0.6}{2\pi} = (4.0 \pm 0.7). \tag{3.4}$$

Out of 408 two-track events, if the criterion of a *single* hit within 0.15rad in ϕ of *one* charged track is used for muon identification, this would result in mis-identification in a total of (0.98 ± 0.17) % of the events. Since all the selection procedures used for muons are generally more demanding and require at least two hits in the muon chambers, the percentage of mis-identified events due to noise drops to (0.0096 ± 0.0024) maximum.

The signal-to-noise ratio is equal to the (corrected number of noise hits over all the barrel)/ (corrected number of hits within 0.15rad of the track) which gives (42.0 ± 7.2 / 1408 ± 37.5) = (0.030 ± 0.0005) or a ratio of (33.5 ± 1.0) : 1

In conclusion the noise levels in the muon chambers during the 1989 running are expected to have a negligible effect on muon event selection. However, in order to be able to model their effect correctly these noise estimates are used in the MUB component of the DELSIM35 detector simulation, which provides the simulation data for the analysis of Chapter 4.

Chapter 4
Leptonic Analysis of the 1989 Data

Preamble

Chapter 4 presents a detailed study of the data collected during 1989 by the DELPHI detector over 10 c.m. energies in a scan across the Z° resonance peak; the partial width ratios Γ_{had}/Γ_{ee} and $\Gamma_{had}/\Gamma_{\mu\mu}$ are computed to be $(20.3 \pm 1.4(\text{stat.}) \pm 0.9(\text{syst.}))$ and $(20.3 \pm 1.3(\text{stat.}) \pm 0.6(\text{syst.}))$ respectively. The ratio $\Gamma_{\tau\tau}/\Gamma_{\mu\mu}$ is estimated to be $(0.85 \pm 0.14(\text{stat.}))$. The data sample used and the method of analysis are explained, and the leptonic selection cuts are derived from studies of the real data. The numbers passing these cuts are then corrected to the idealized numbers for a perfect detector using correction factors derived from real and simulation data studies, and the computed backgrounds to each sample are subtracted. Finally these numbers are compared to the reconstructed numbers of hadrons from the hadronic data analysis of DELPHI analysis team IV, and the photon exchange corrections added to obtain the final partial width ratios for Z° decays.

4.1 The Data Sample

The raw detector data were processed by DELANA31. A subset of dilepton [1] candidates from the total data sample was obtained by extracting those events with the following characteristics in the resulting TANAGRA data banks:

- $1 \leq N_T < 9$ where N_T is the total number of tracks;
- at least one track with a minimum r (distance to the beam axis) of less than 8cm;
- a displacement (z) from the centre of DELPHI at the position of minimum r of less than 10cm;

[1] The term 'dilepton event' is used as an abbreviated expression for the production of a pair of charged lepton/antilepton particles (l^+l^-) in this and subsequent chapters, as are the expressions 'dimuon event' (specifically for $\mu^+\mu^-$ production) and 'ditau event' (specifically for $\tau^+\tau^-$ production). These are used in an analagous way to the term 'Bhabha event', which refers to the process $e^+e^- \rightarrow e^+e^-$. The words 'dilepton','dimuon', 'ditau' and 'Bhabha' are sometimes used on their own for convenience.

- a total measured energy in the event of more than 8GeV.

A perfect event sample should then, in principle, contain all the dilepton events, except a negligibly small ditau sample either generating 10 secondary tracks ($\sim$ 3/1000000) , or with $>$ 82GeV carried away by neutrinos, and some background beam gas and cosmics. However two facts must also be taken into account:

- the dilepton triggers and the detectors used for track reconstruction and particle identification have an efficiency $<$ 100% and have geometrically restricted active regions;
- there were running periods during which one or more of the key detectors were not operational.

As a consequence of this second point, those runs where the TPC, the HPC, the MUB and the detectors in the trigger were not all operational were excluded from the data sample.

The dileptonic trigger consisted of an OR of the following:

- coincident hits in back-to-back TOF sectors;
- coincidences between ID and OD hits requiring back-to-back tracks;
- The HPC scintillator system set to a threshold of $\sim$ 2GeV.

These are all barrel detectors. The forward detectors in DELPHI did not in general perform well enough during the 1989 data taking to generate reliable triggers, and were still giving some problems in 1990. Therefore all this analysis is restricted to the barrel region of DELPHI where all the trigger, tracking and particle identification detectors are available: $50° \leq \theta \leq 130°$. The trigger efficiencies were measured by using the final data sample and *assuming* the triggers were independent. The efficiency of the combination of ID/OD and TOF for triggering on dimuon events was found to be (97 ± 2)% in 1989 and that of the ID/OD and HPC combination for Bhabhas was found to be $>$ 99.7% in 1989 (see ref. [37]). The cause of the difference was the much smaller efficiency of the TOF for dimuons compared to the HPC for Bhabhas.

A weakness of any analysis with a digital detector such as DELPHI where the particle tracks are reconstructed by computer, rather than seen directly in a device such as a bubble chamber, is that the analysis is dependent on efficient tracking detectors and reliable track reconstruction algorithms. The data set of this analysis has already passed through a track selection procedure where at least one reconstructed track was demanded to be present. In November and December 1989 an extensive program of interactive event scanning on 3-D workstations by members of the DELPHI analysis team II was set up with the aims of examining the general characteristics of dilepton events, checking software algorithms used for particle identification, and searching for instances of detectors responding to the passage of a particle without tracks being reconstructed. This led to an interesting discovery. The scanning team found 245 dimuon candidates in total by looking by eye for hits in the muon chambers, and/or minimum ionizing tracks in the HPC and HCAL that seemed to line up. Six of these had only one compatible track in the TPC. However in all of these six the projection of the line in z of the missing track, as seen by the hits in the calorimeters and MUB, passed through a crack between the TPC end-cap readout pads. An example of this is shown in Fig. 4.1; no evidence of track loss in events was found in regions of the TPC away from the cracks between the readout pads.

Having found this problem arising from the gaps in the TPC read-out pads, a further study can be carried out to compare the efficient and inefficient angular regions for lepton track reconstruction. A plot of modulo$(\phi, 60)$ can be made of tracks in events passing a set of standard lepton track and identification cuts in such a way that the TPC cracks line up in the centre of the plot. Assuming that the true ϕ distribution is uniform, the missing number of events can be estimated by dividing the plot into equal slices and comparing the number of events in the central slice to the mean number in the others. These results are presented in Section 4.13 after the selection cuts for dimuons and Bhabhas have been determined.

4.2 The GEDTAN Analysis Program

GEDTAN is a pattern recognition program for the identification and analysis of leptonic events. The authors are N.C.E. Crosland and myself. The input

Figure 4.1: An example of track reconstruction failure in the 1989 data.

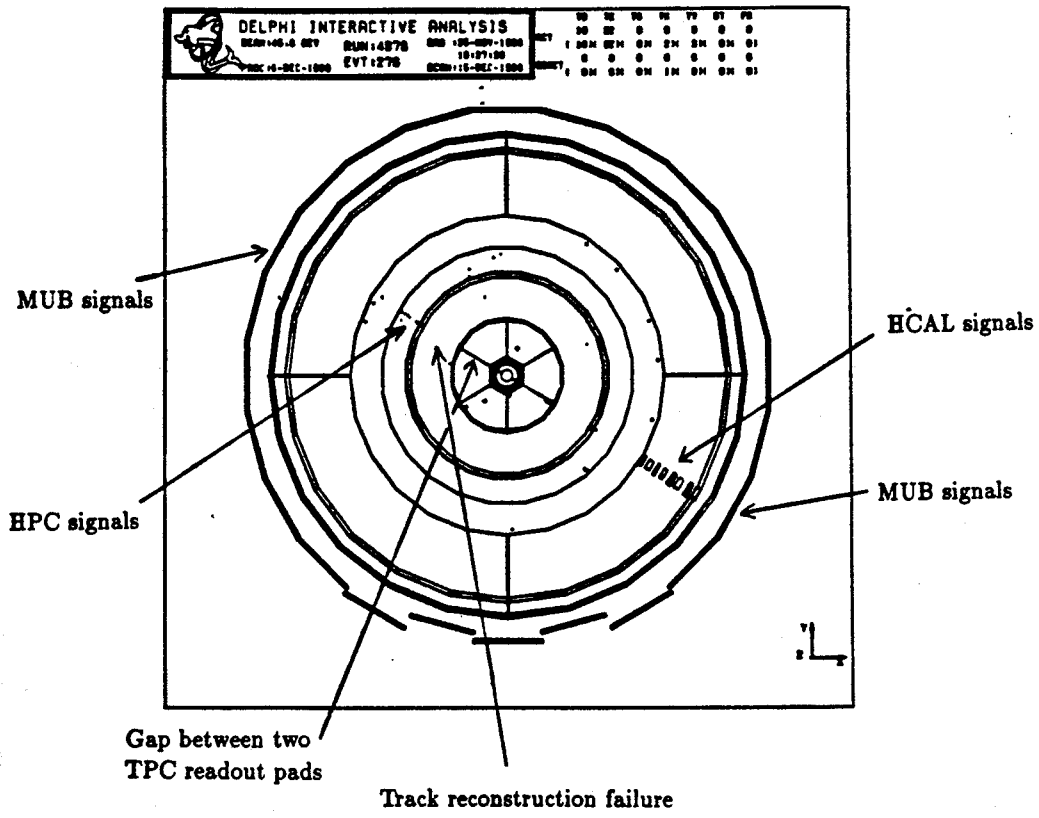

consists of the TANAGRA banks generated when raw data are processed by DELANA. GEDTAN produces a large NTUPLE as its primary output. This is a single column array of information for each event which is accessed after processing by the Physics Analysis Workstation (PAW) package (see ref. [38]) for the purpose of doing interactive event analysis. The advantage of this approach is that only crude assumptions need to be made about the characteristics of the data during the primary processing. The information about the each event is stored in the NTUPLE and the initial processing, which requires considerable computer time, only needs to be done once. After the NTUPLE, which summarizes the information on every event, is formed, event selection cuts can be added by the PAW user, and the behaviour of variables in the resulting event sample can be plotted in histograms. The plots used in this thesis are all produced in this way.

The program operates in the following way. The TANAGRA TK banks, which contain the track segments formed in the initial DELANA processing, are made

available for each event. GEDTAN then extrapolates the tracks back towards the beam-axis of DELPHI. This is done by obtaining the position and momentum vector at minimum r (the distance from the beam axis) of the track segment, by drawing a cylinder around the beam-axis of incrementally smaller radius, and then calculating whether the extrapolated track intersects this smaller cylinder, taking into account the behaviour of the particle in the magnetic field. If it does then the momentum and position vector of the extrapolated track on the cylinder are recalculated and the process is repeated until the extrapolated track no longer intersects the cylinder. GEDTAN then stores the coordinates and momentum of the track at this new minimum r. The quantity r is minimized, rather than z (the displacement along the beam axis from the centre of DELPHI) because the measurement of r is designed to be considerably more accurate in DELPHI than that of z[2]. This analysis is concerned with two-track events, and therefore the next step is to store information on the two tracks with the highest momenta in the event. A limiting minimum value of 1GeV/c is also a requirement. The acolinearity of these two tracks is then calculated and stored, along with the other track parameters, in the NTUPLE. The next step is to test the response of the HPC and MUB to the tracks. A search is made for hits within different angular displacements of the tracks in both the HPC and the MUB. The integrated HPC energy within a range of different cone opening radii about each track is stored in the NTUPLE and the summed number of hits in different layers of the MUB is also stored in a similar way. A picture of this process applied to an event is shown in Fig. 4.2.

The program is also capable of decoding the initial state information about all the particles generated in DELSIM simulation studies and an attempt is made to match up the initial generated tracks to the final reconstructed tracks. This information can also be stored in the NTUPLE. This is a powerful use of the simulation data, as it is possible to study backgrounds and losses of signals in detail as information is available about the kinds of generated particles that form

[2]The magnetic field causes particle trajectories to change in the x-y plane, and accurate measurements are therefore required in this plane to determine the track curvature and hence the momentum; the component of a particle velocity along the magnetic field direction (the z direction) is unaffected by the field. In addition the particle collision point is less well defined along the z axis (see Chapter 2).

Figure 4.2: The analysis of a dimuon event by the GEDTAN program.

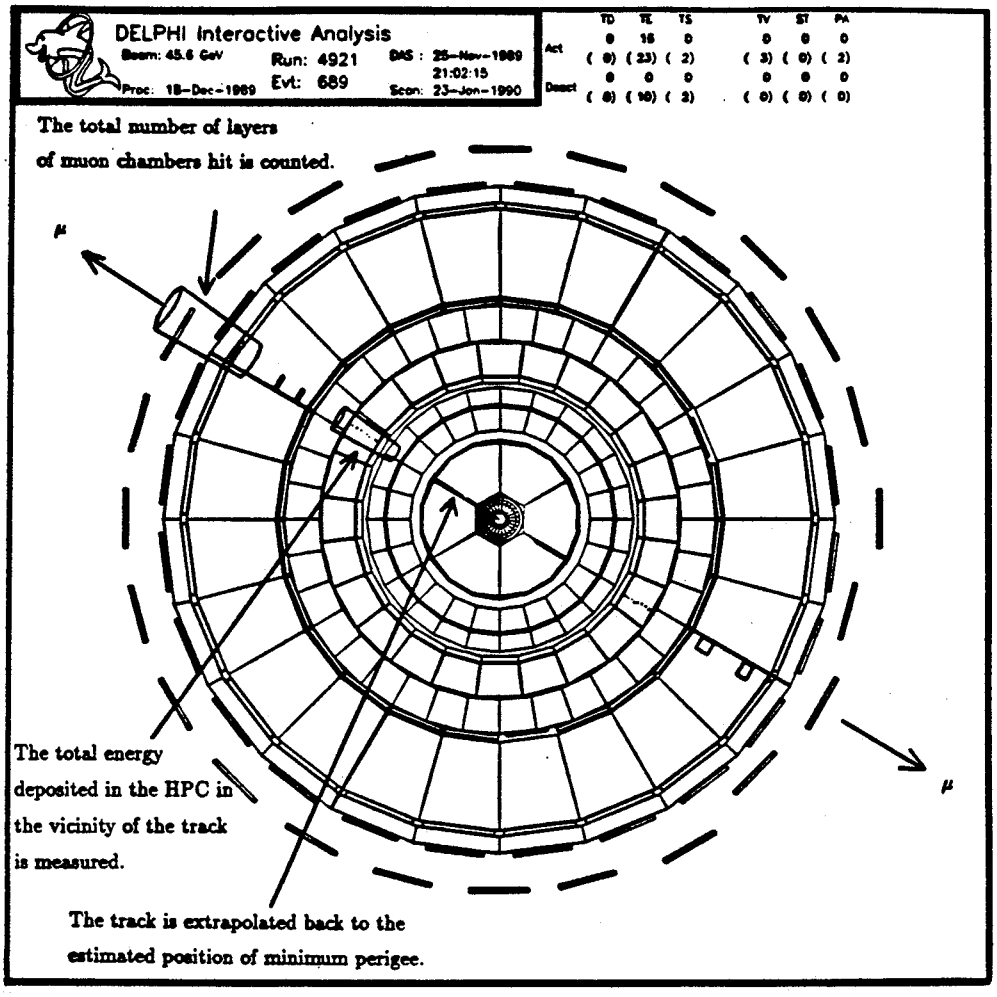

the backgrounds and the geometrical regions of DELPHI they penetrated. In this way, more can be learned about how to improve the cut criteria for event selection, rather than simply computing an overall percentage figure for the background and efficiency.

4.3 Simulated Data Samples

Three simulated data samples have been prepared for this analysis: 8639 events over the full solid angle generated using the DYMU3 dimuon generator; 8998 events over the full solid angle with the KORALZ ditau generator and 4098 Bhabha events generated using the BABAMC generator with both outgoing electrons within the angular range $43° \leq \theta \leq 137°$ (3846 of these being within

the active analysis region of $50° \leq \theta \leq 130°$). These generators are discussed briefly at the end of Chapter 1. The simulated samples have been passed through the DELSIM35 full DELPHI simulation program with all secondary decays and interactions with the detector material simulated and then through DELANA31 and the GEDTAN leptonic program to produce PAW NTUPLES for interactive analysis; the simulation data have therefore been processed in an identical way to the real data. The version of the DELSIM program used, version 35, has modifications based on studies of the 1989 data within it, for example the MUB noise levels calculated in Chapter 3, so it is the most suitable simulation program currently available for this work.

4.4 Characteristics of Dilepton Events

The selection of cuts used in the event selection procedures is essentially an iterative process, so it is worth listing some general characteristics of dilepton events to use as a starting point; example pictures are shown in Figs. 4.3, 4.4 and 4.5 of a Bhabha event, a dimuon event and a ditau event respectively using the DELPHI event display program to illustrate some of the points discussed below. Dimuon events are characterized by two back-to-back tracks with combined momenta equivalent, or nearly equivalent, to the centre-of-mass energy of the colliding beams. They are not perfectly acolinear because of electromagnetic interactions with the material of the detector and because of final state bremsstrahlung. However the acolinearity tends to be small - less than 1°. The muons in general pass through all the material of the detector and deposit only small fractions of their energy in the calorimeters, the value being close to the theoretical minimum possible for a charged particle in the Bethe-Bloch formula; they are consequently described as *minimum ionizing particles.* If the projected track of the muons pass through muon chambers on the perimeter of DELPHI they should generate hits in these to mark their passage. Although muons are unstable particles having a mean lifetime before decaying to electrons and neutrinos of about 2.2μsec [39], a time dilation factor of about 426 at 45GeV means that the probability of a muon decaying within 4.5m of the centre of DELPHI is about 1.6×10^{-5}, and can be safely ignored as a source of background.

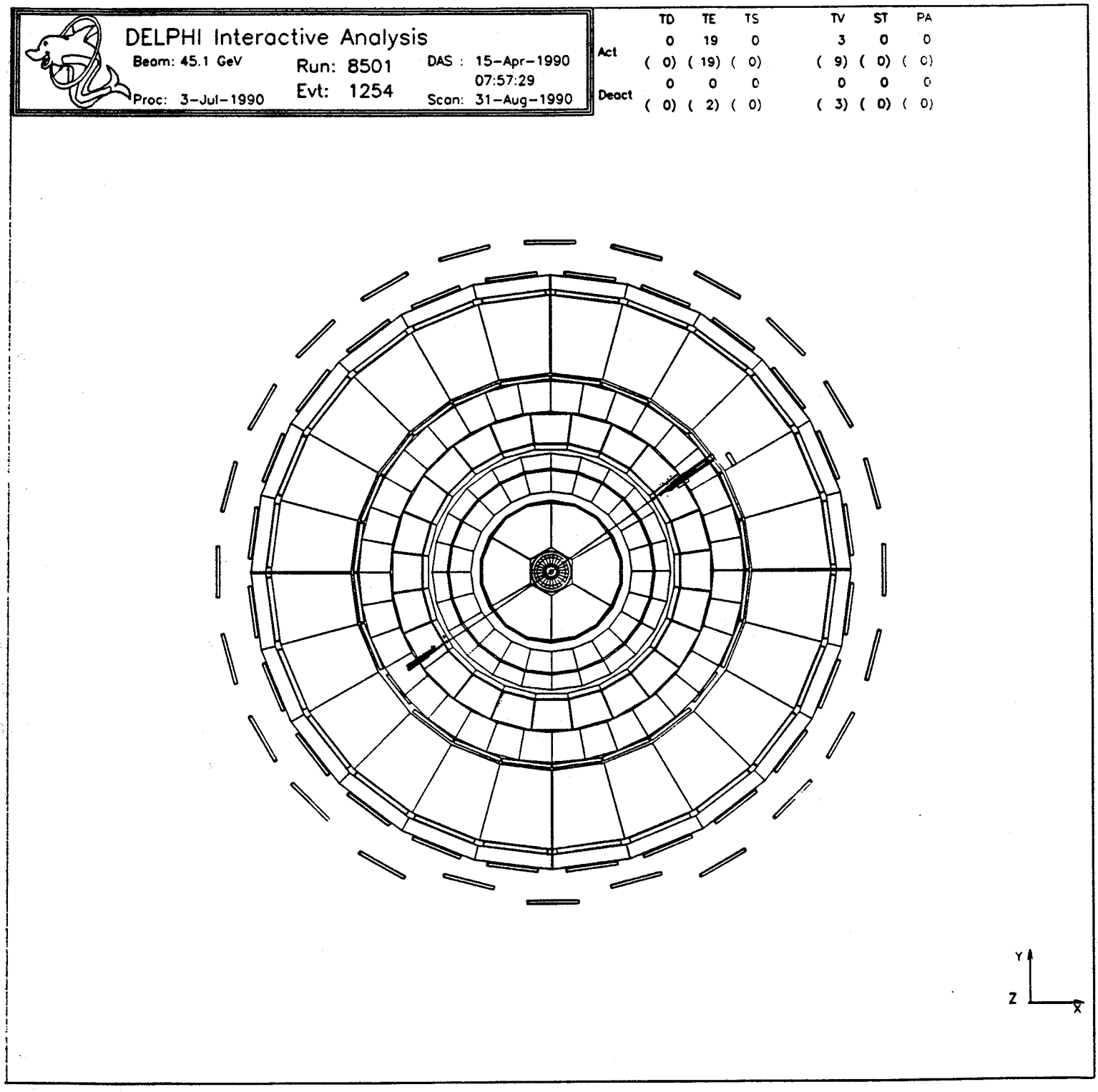

Figure 4.3: An example of a Bhabha event. Two back-to-back electrons have been projected from the centre of DELPHI and have undergone bremsstrahlung interaction with the lead of the HPC, thereby generating distinctive electromagnetic showers.

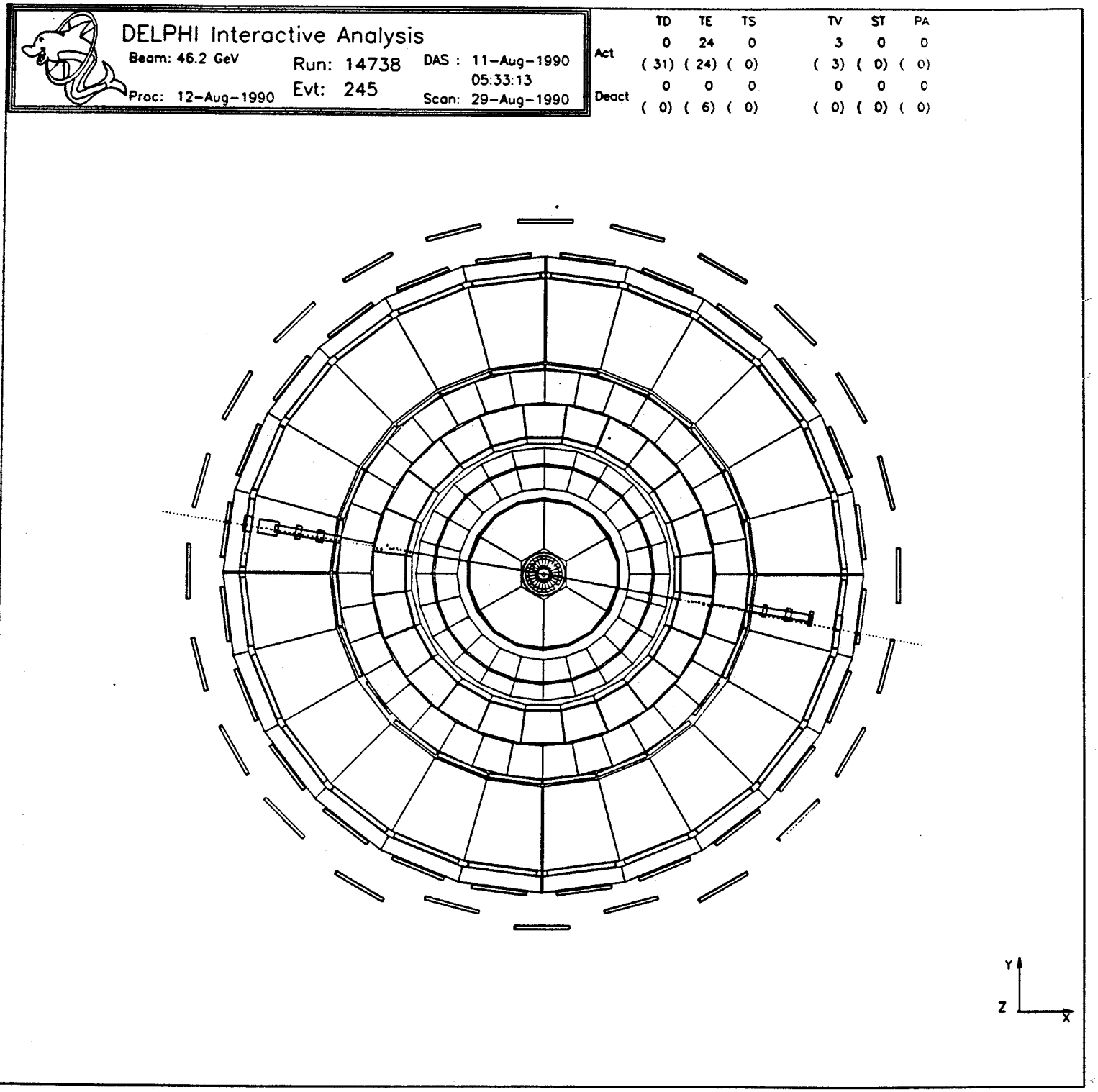

Figure 4.4: An example of a dimuon event. Two back-to-back muons have been projected from the centre of DELPHI and have passed, with minimal interaction, through the HPC and HCAL. They have generated signals in the MUB, on the outside of DELPHI, to mark their passage. The dotted lines mark the extrapolated track positions.

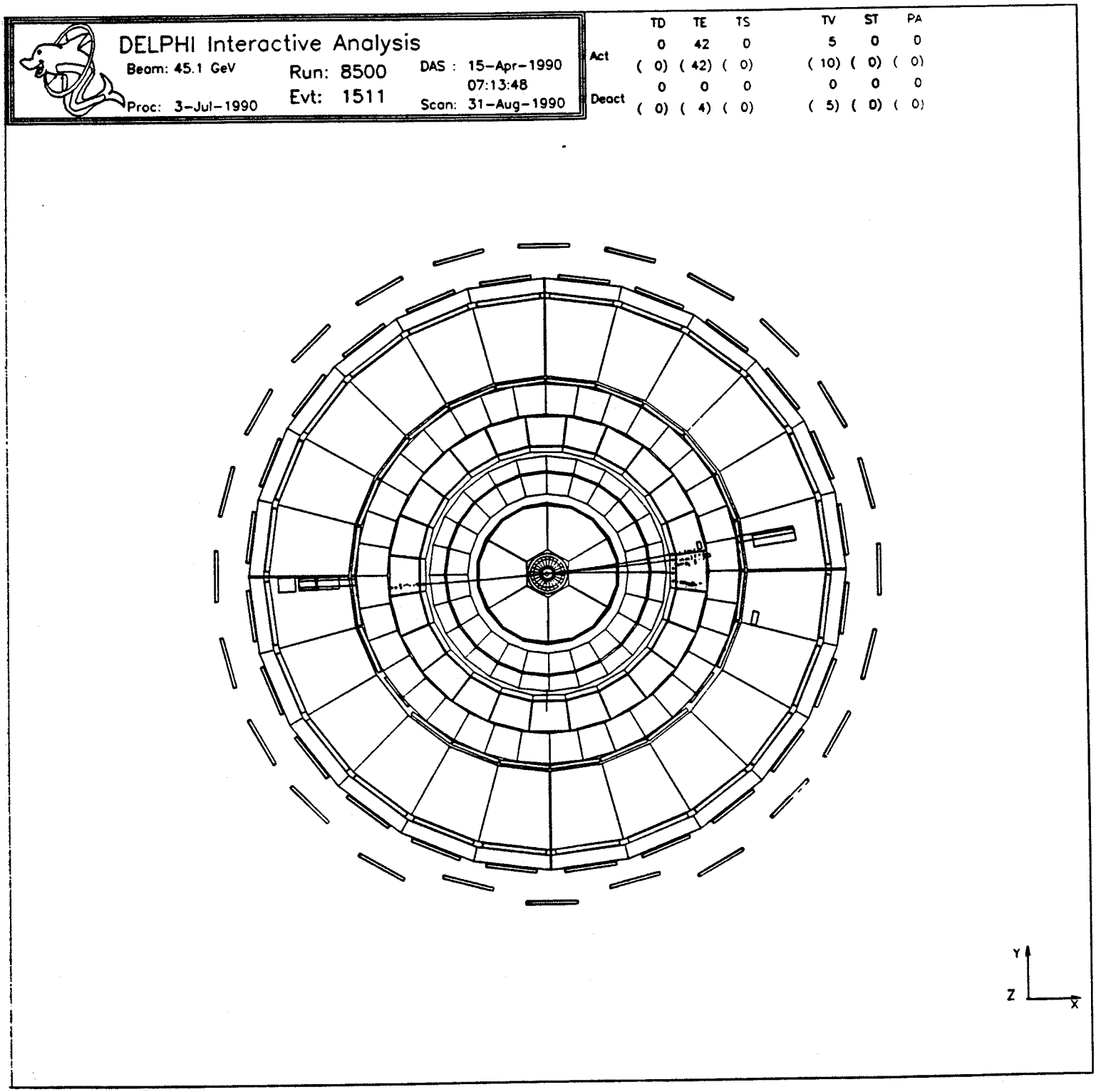

Figure 4.5: An example of ditau production. One tau has decayed to a single charged pion, the other to three charged pions. These have been absorbed by nuclear interactions with the material of the HCAL.

Bhabha events also produce two charged tracks. However the probability of final state radiation is greater so there is a higher average acolinearity and probability of secondary tracks from photon pair production. Electrons interact powerfully with the lead in the HPC through bremsstrahlung interaction and generate large and distinctive showers of secondary particles. Ditau events come in several categories depending on the decay products. Taus have a mean lifetime of $(3.04 \pm 0.09) \times 10^{-13}$sec [39] and a time dilation factor of 25.22 at 45GeV. They will therefore travel an average distance of 2.3mm in DELPHI before decaying. At least one neutrino is generated in this process that can carry away energy and momentum, and so even those ditau events that produce two final state charged tracks will be characterized by a smaller combined absolute momentum and larger mean acolinearity than the Bhabha and dimuon events. The final state charged particle from a tau decay can be a muon, electron, pion or kaon. Three or five pions can also be produced. Charged pions are often produced in conjunction with neutral pions that decay to photons. These have an important consequence for particle identification in the HPC as studies in Section 4.10 show.

4.5 General Overview of Event Selection

There are two main sets of criteria used in the event selection. The first are cuts on the parameters (such as absolute momentum and angle) of the tracks, and the second are cuts on the results of particle identification procedures. The objective is to obtain samples that are as clean as possible without sacrificing statistics. Even more importantly it must be possible to reliably compute the efficiencies and backgrounds obtained with the selection cuts. The cuts used in this analysis are labelled by the dagger symbol $\dagger_n$ where n labels the cut number.

Particle identification is made in the following way. A cone of a few degrees opening angle is made about the track angle at the point of minimum r to the interaction point in DELPHI, and the signal from the relevant particle identifying detector within the cone is measured. This is a relatively simple technique, and does not involve the need for track extrapolation out to the detector itself. It is therefore straightforward and less prone to errors in the software. It works provided the deviation of the track in the DELPHI magnetic field is small and if

the background noise in the detector is low. The radius of curvature,a, of a single charged track in a constant magnetic field of 1.2T is given by

$$a(\text{cm}) = (1000/3.6)p_T, \tag{4.1}$$

where p_T is the momentum transverse to the field in units of GeV/c. The total angular deviation from the original straight line projection after having travelled from a radius of 0 to a radius D is given by:

$$\rho = \arctan(D/\sqrt{4a^2 - D^2}), \tag{4.2}$$

which gives a deviation of about 2.17° at 210cm (the radius of the HPC) for a 10GeV/c p_T particle, and 0.008° for a 45GeV/c p_T particle. Muons will not be deflected further once they have penetrated the superconducting coil at about 300cm and will be deflected back closer to their original path as they pass through the return yoke. This is not intended to show the validity of a straight line assumption, but merely to show that it is plausible as a good approximation - when the opening angle of the cone about the initial angle of the track is of the order of 10°. The demonstration of the validity of this method is shown later in the study of the events themselves.

The particle identification of muons is done primarily by the MUB. Here the basic technique is to search for hits within the cone drawn about the track. The test for electrons is to sum the energy within the cone in the HPC and to test whether it is larger than some limiting value. A test for muons in the HPC can also be done by testing whether the energy deposited is less than some limiting value. The HCAL can in principle be used for pion selection, but for the data sample considered here, was not operating reliably. Therefore in this analysis it is not used, even though this does give rise to slightly larger backgrounds in the muon and electron samples by tau decays to pions.

4.6 Track Selection: First Iteration

The first cut to be made is to demand the two highest momenta charged tracks to be within the barrel region of $50° \leq \theta \leq 130°$ within which the triggers and detectors are active. The channels studied in this analysis are all channels

where two principal tracks result. For electrons and muons these tracks should both have a momentum about 45GeV, while for two track tau events the tracks should have a large range of momenta. Initially muon and electron identification is considered only as these have more constrained characteristics. The difficulty with momentum selection is that the accuracy will tend to decrease with the momentum of the track as it is the track *curvature* that is being determined, for which the uncertainty will increase as the track straightens out, and initially the sensitivity of DELPHI is unknown. The answer is to use the characteristics of dimuon and Bhabha events to determine their own cut selections when examining the real data. The following restrictions are used as a starting point and applied to the leptonic sample:

$\dagger_{A1}$: The two tracks with the highest momenta satisfy $50° \leq \theta \leq 130°$.
$\dagger_{A2}$: The two tracks with the highest momenta are within 10° of being acolinear i.e. perfectly back-to-back.
$\dagger_{A3}$: A maximum number of two charged tracks have a momentum greater than 1GeV/c. (4.3)

A complication is that 1/3 of the data taking in the 1989 runs was with a reduced strength magnetic field, and is therefore expected to have a degraded momentum resolution. Distributions from data generated under both field conditions during 1989 are shown in Fig. 4.6. Both are plots of the inverse momentum since it is the radius of curvature that is actually measured in DELPHI. The first plot is for those runs with the reduced field strength of 0.7T; the second for those runs with the full 1.2T magnetic field strength. Both plots are generated from the leptonic sample applying cuts $\dagger_{A1}$,$\dagger_{A2}$ and $\dagger_{A3}$ listed above. The important point to notice is that there is a broad peak at about 0.0225 GeV^{-1}. This corresponds to tracks with momenta of about 44.4GeV, which is compatible with the momenta of characteristic tracks in dimuon or Bhabha events. There is a low-momentum tail compatible with the known kinematics of ditau events. Events in the peak appear to be restricted in both cases to an inverse momentum of less than 0.1GeV^{-1}, so a first iteration cut for the track momenta in dimuon and Bhabha events could be,

Figure 4.6: The inverse momentum distribution for the two highest momenta tracks in events selected using the first iteration cuts on the 1989 data. Plots (a) and (b) show the distributions in the reduced strength and full strength magnetic fields respectively.

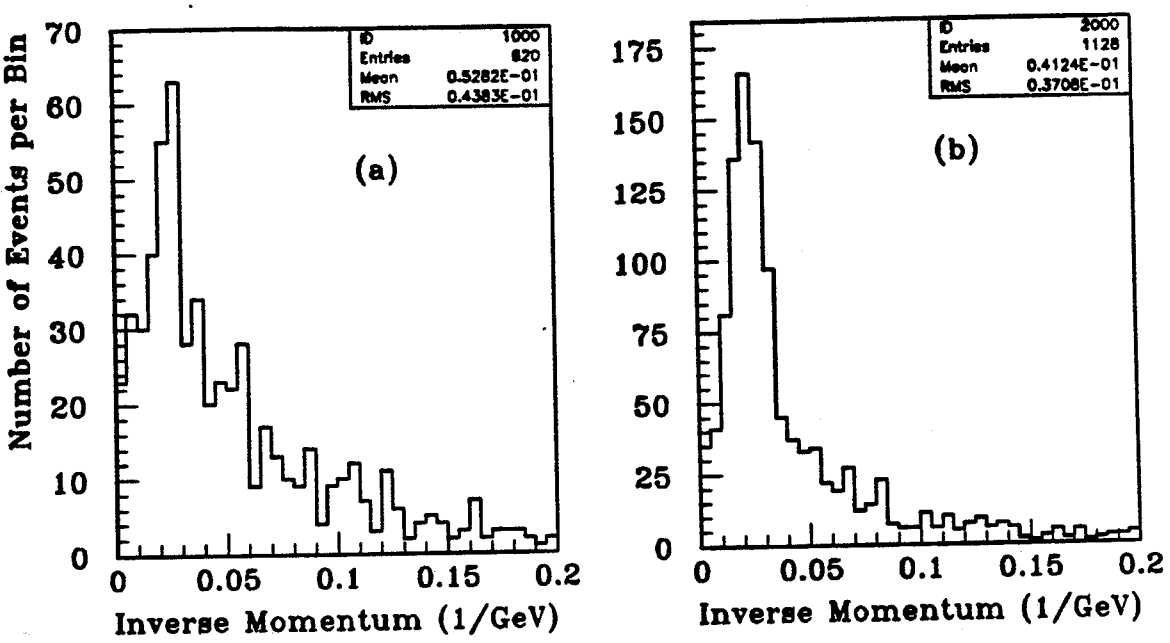

Analysis Conditions	
0.7T field data sample	Runs 3302 - 3983
1.2T field data sample	Runs 4157 - 6057
Analysis package	DELANA31,GEDTAN
Selection cuts	$\dagger_{A1}$,$\dagger_{A2}$,$\dagger_{A3}$

$\dagger_{A4}$: $P_1 \geq 10.0$GeV/c and $P_2 \geq 10.0$GeV/c where P_1 and P_2 are the momenta of the two highest momenta tracks. (4.4)

4.7 Muon and Electron Identification

It is now necessary to try to identify the particles produced. It has been shown in Section 4.5 that particles with 10GeV/c or more transverse momentum to the magnetic field will not be deflected by the field more than a few degrees in ϕ. Using cuts $\dagger_{A1}$,$\dagger_{A2}$, $\dagger_{A3}$ and $\dagger_{A4}$, plots are shown in Fig. 4.7 of $\Delta\phi = \phi_M - \phi_{TK}$, $\Delta\theta = \theta_M - \theta_{TK}$ and $\Delta\rho$ from the 1989 data sample. 'M' denotes a hit in the MUB, 'TK' denotes one of the two tracks, and $\Delta\rho$ is the absolute angular difference. The $\Delta\phi$ distribution is smeared in the plots because of charged particle deflection,

Figure 4.7: The differences between the angular coordinates of hits in the MUB compared to tracks extrapolated back to their minimum r in DELPHI. Plots (a) and (b) show the differences in the θ and ϕ coordinates. Plot (c) shows the magnitude of the overall angular difference.

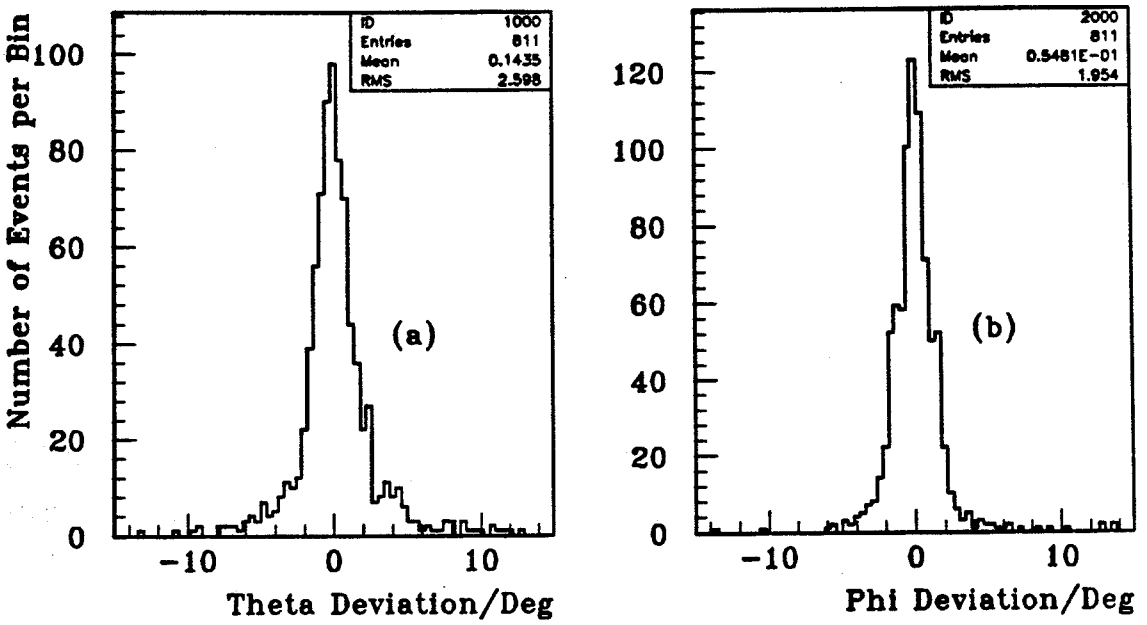

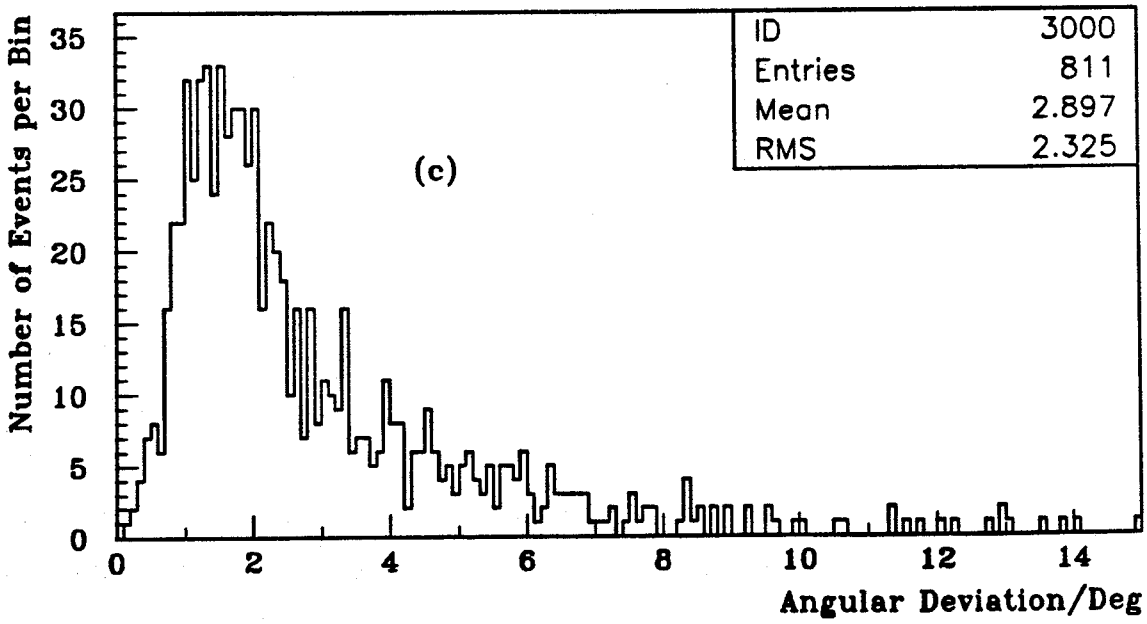

Analysis Conditions	
Data sample	Runs 3302 - 6057
Analysis package	DELANA31,GEDTAN
Selection cuts	t_{A1},t_{A2},t_{A3}, t_{A4}

whereas the $\Delta\theta$ distribution is smeared owing to a poorer z-resolution along the delay line of the chambers. It would appear that to ask for a hit in the MUB with $\Delta\rho \leq 10°$ would be a valid identification of a particle being compatible with a muon. Noise levels are very low in the MUB (see Chapter 3) and by asking for both tracks to have hits the noise contribution to the event selection will be negligible. This cut will be called $\dagger_{A5}$.

$\dagger_{A5}$: $N_1 \geq 1$ and $N_2 \geq 1$, where N_1 and N_2 are the number of layers of MUB chambers hit within 10° of each of the two highest momenta tracks. (4.5)

The electron selection cut relies on summing the HPC energy inside a cone about the track. The HPC is designed to cause electrons to shower and most of their energy to be deposited within it. Electrons from Bhabha events should have about 45GeV of energy. From interactive event scanning it seems that most of the energy is deposited within 1° or 2° of the charged track. Therefore the integrated energy within 10° should be a safe estimate of the deposited electromagnetic energy of an track.

The plots in Fig. 4.8 are the following. An assumption is made that one particle in a two track Bhabha event impacts with the HPC and deposits most of its energy, most of which is picked up and exceeds 15GeV within 10°. This cut may be too high or too low, but the sample should then at least be mainly Bhabhas, with a small ditau contamination. The energy of the *other* particle in the decay is then examined. The standard cuts $\dagger_{A1}$,$\dagger_{A2}$,$\dagger_{A3}$ and $\dagger_{A4}$ have also been applied. The results show the most of the events have an energy within the 10° cone of $\geq$ 25GeV. However, a small number, particularly of the reduced field data, go down to nearly 10GeV. Therefore a cut for Bhabha selection could be:

$\dagger_{A6}$: $E^A{}_{HPC} \geq 25$GeV and $E^B{}_{HPC} \geq 10$GeV where $E^A{}_{HPC}$ and $E^B{}_{HPC}$ are the energies deposited within 10° of each of the two highest momenta tracks. (4.6)

Figure 4.8: The measured energy deposition within 10° of a charged track in the 1989 data. The acolinear track in the event must itself deposit at least 15GeV of energy for the event to be plotted. Plots (a) and (b) show the distributions in the reduced strength and full strength magnetic fields respectively.

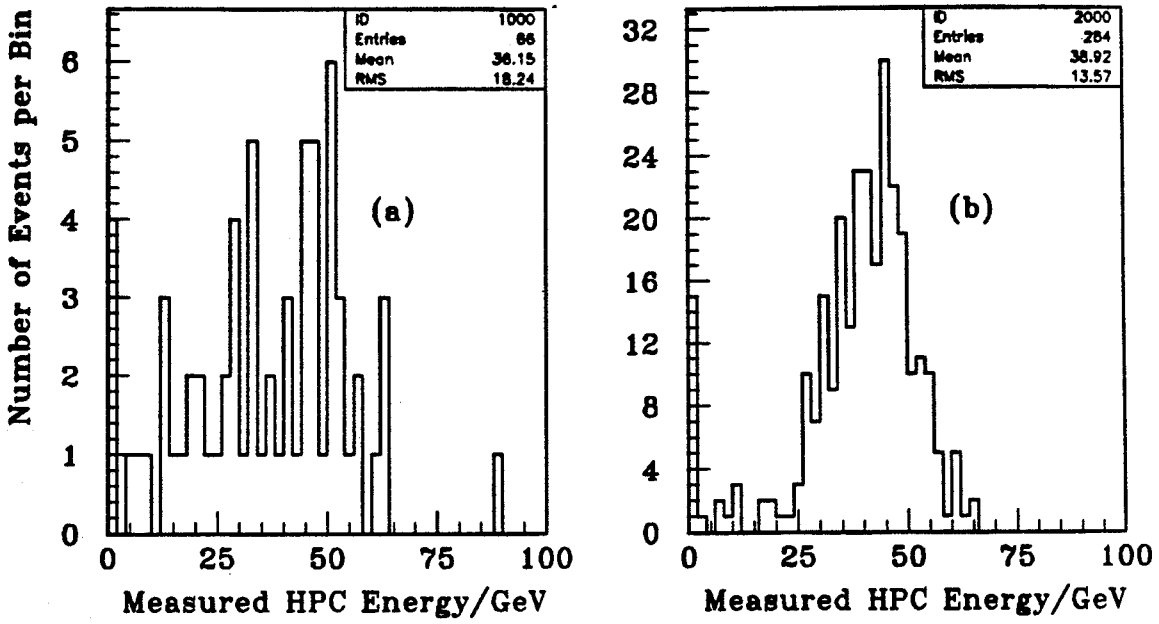

Analysis Conditions	
0.7T field data sample	Runs 3302 - 3983
1.2T field data sample	Runs 4157 - 6057
Analysis package	DELANA31,GEDTAN
Selection cuts	$\dagger_{A1}$,$\dagger_{A2}$,$\dagger_{A3}$,$\dagger_{A4}$ and acolinear track has $\geq$ 15GeV associated with it

The HPC can also be used as an alternative means of muon identification. Fig. 4.9 shows the normalized distributions, for both the 1989 data and the simulation data, of the HPC energy recorded within 10° of a MUB identified dimuon event. The cuts applied are $\dagger_{A1}$,$\dagger_{A2}$,$\dagger_{A3}$ and $\dagger_{A4}$ and $\dagger_{A5}$ to both data sets. The energy is also required to exceed zero to indicate the HPC has actually responded to the passage of a charged particle.

The plot shows that a maximum energy of 2GeV associated with a track would be a possible alternative muon identification method. It is interesting to note that the tails of these distributions are partly due to photons being radiated and converting in the HPC. From the shape of these plots a cut $\dagger_{A7}$ may be defined for selection by the HPC alone:

Figure 4.9: The normalized measured energy distribution in the HPC within 10° of MUB identified muon tracks. The plots of the 1989 data and simulation data are shown superimposed. Errors bars are plotted on some bins to indicate the statistical errors for the real and simulation data.

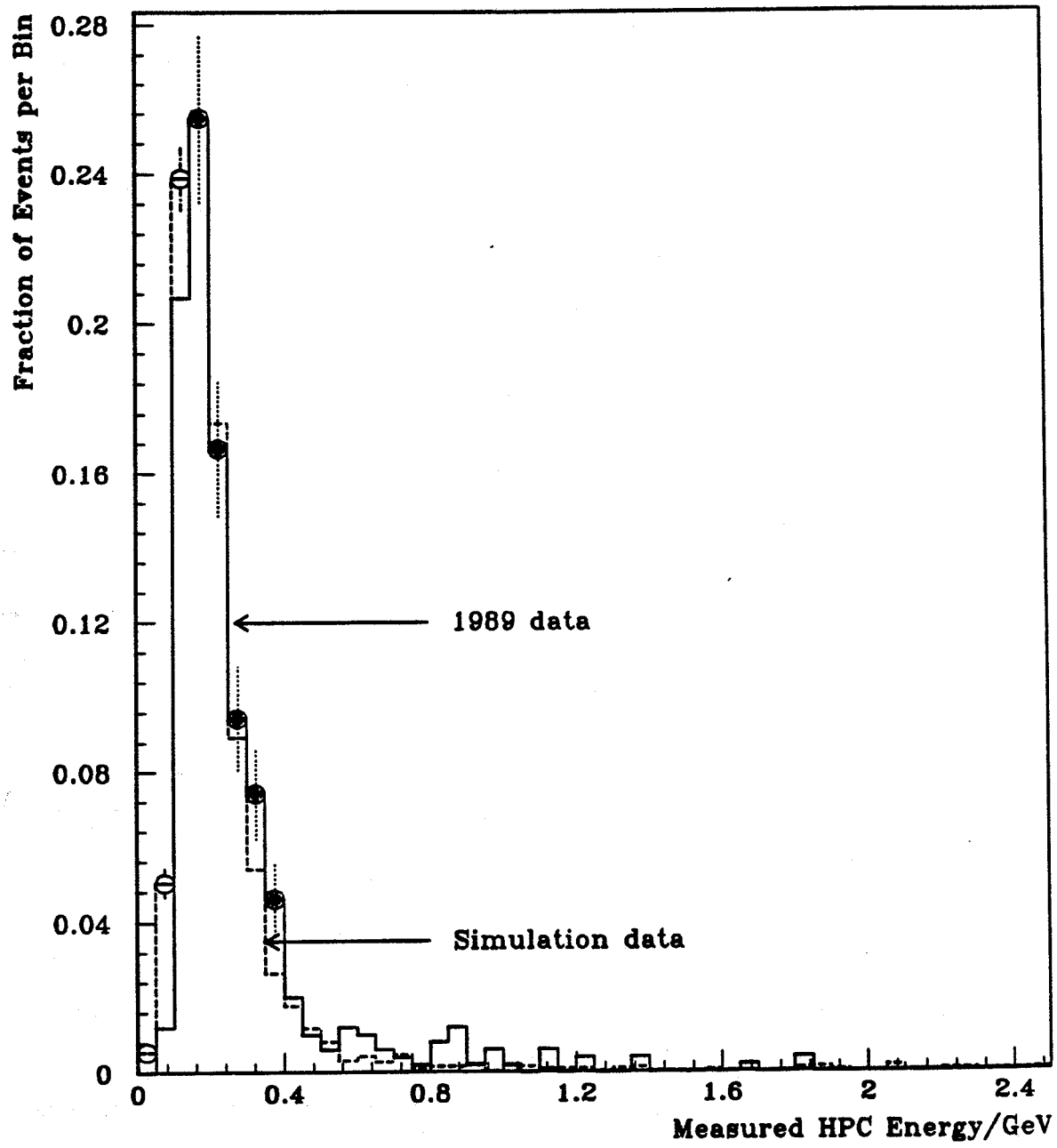

Analysis Conditions	
1989 data sample	Runs 3302 - 6057
Analysis package	DELANA31,GEDTAN
Detector simulation	DELSIM35
Muon generator and sample size	DYMU3: 3900 events
Selection cuts	t_{A1},t_{A2},t_{A3},t_{A4} t_{A5} and deposited energy exceeds zero

$\dagger_{A7}$: $0 < E^A{}_{HPC} < 2\text{GeV}$ and $0 < E^B{}_{HPC} < 2\text{GeV}$ where $E^A{}_{HPC}$ and $E^B{}_{HPC}$ are the energies deposited within 10° of each of the two highest momenta tracks. (4.7)

It is also possible to combine the muon selection criteria with the MUB and HPC so that each track separately must be identified as a muon, but that this identification may be done with either detector. This method of selection increases the efficiency by increasing the permutations of signals that give a positive identification of a dimuon event:

$\dagger_{B7}$: $[0 < E^A{}_{HPC} < 2\text{GeV}$ or $N_A \geq 1]$ and $[0 < E^B{}_{HPC} < 2\text{GeV}$ or $N_B \geq 1]$ where $E^A{}_{HPC}$ and $E^B{}_{HPC}$ are the energies deposited within 10° of each of the two highest momenta tracks, and N_A and N_B are the number of MUB chambers hit within 10° of each of these tracks. (4.8)

4.8 Track Vertex Cuts

One background to dimuon events in DELPHI are cosmic rays, and it is necessary to make a vertex cut to eliminate some of this background. The plots of Fig. 4.10 show the results of vertex studies.

The cuts $\dagger_{A1}$,$\dagger_{A2}$,$\dagger_{A3}$ and $\dagger_{A4}$ have been applied to all of them. The hashed plots are the events also satisfying cut $\dagger_{A6}$ (and are therefore mainly electrons): the clear plots are of those events satisfying cut $\dagger_{B7}$ (and are therefore mainly muons). The two left hand plots are of the value of z when r is at a minimum. The two right hand plots are of the minimum value of r itself. Two points are immediately clear. There is a background to the dimuon distribution beyond the peak (the cosmic ray background) and there is no Bhabha background of this kind. Therefore a vertex cut is only necessary for dimuons. Plots (a) and (b) have no addition cuts other than those already mentioned. However from plot (b) a 1.5cm cut in the value of r has been obtained as a safe first order vertex

Figure 4.10: Vertex studies of the 1989 data. r is the minimum distance of the extrapolated charged track from the beam axis. z is the value at r of the displacement along the beam axis from the centre of DELPHI. Plot (c) has an additional constraint on the tracks of $r \leq 1.5$cm, and plot (d) had an additional constraint of $|z| \leq 4.0$cm.

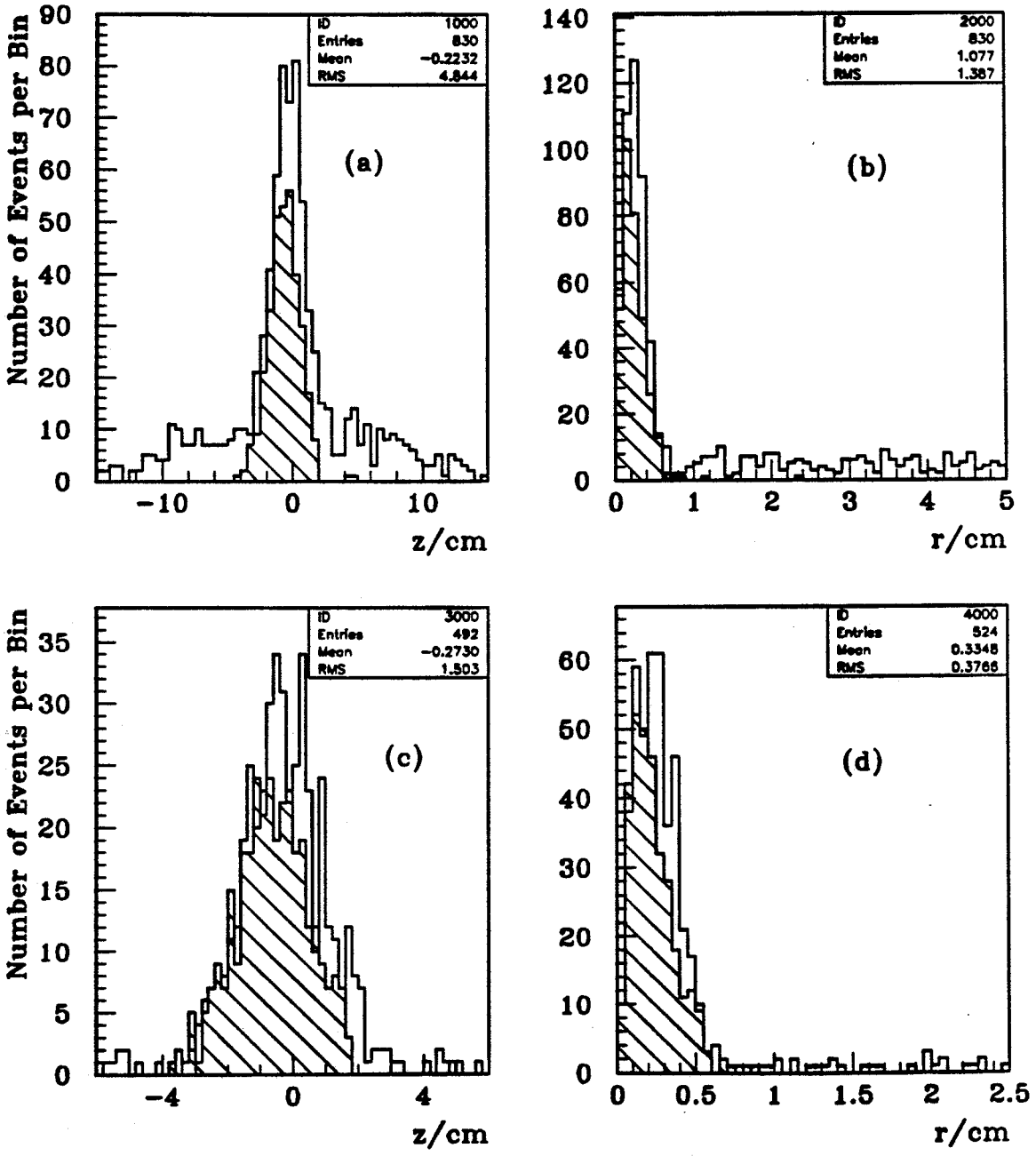

Analysis Conditions	
Data sample	Runs 3302 - 6057
Analysis package	DELANA31,GEDTAN
Selection cuts	$\dagger_{A1}$,$\dagger_{A2}$,$\dagger_{A3}$,$\dagger_{A4}$, $\dagger_{B7}$(clear plots - mainly dimuons) $\dagger_{A6}$(hashed plots - mainly Bhabhas)

cut. This has then been applied to plot (c) which is less well defined to clean it up. This distribution in z is in fact slightly skewed. It is not symmetric about the origin, and the mean value for the muon sample in plot (c) falls at about -0.27cm. The cut in z that is then obtained from this plot and which includes the whole peak is $-4.3 \leq z \leq +3.7$. This has then been applied back to the r distribution in plot (d), from which a second order cut of 0.8cm is obtained. Therefore the vertex cut for the 1989 data can be set as

$$\boxed{\dagger_{AS}\text{: } r \leq 0.8\text{cm and } (-4.3 \leq z \leq 3.7)\text{cm for both the highest momenta tracks.}} \tag{4.9}$$

However, there is one other point to note from these plots. The cosmic ray background can be estimated within the selected sample by extrapolating the flat distribution that exists outside the vertex cuts. This needs to be done after the whole final cut selection has been made.

4.9 Angular Acceptance: Second Iteration

The basic tools now exist for track selection and particle identification. It is now necessary to see what can be learned from them in order to improve the selection criteria. It is necessary to examine the angular region $50° \leq \theta \leq 180°$ in more detail where it is expected that there might be problems originating from the DELPHI geometry. There are two problem areas in particular. In the region around 90° in θ most DELPHI sub-detectors have a least some dead space, and problems may also be encountered in the regions near 50° and 130°, which are close to the geometric gap between the barrel and end-cap parts of DELPHI.

The results are shown in Fig. 4.11. There is some indication of a small gap of about $\pm 1°$ about 90° for muon identification, though the statistics are too low to be sure. It is expected that a small gap should exist where tracking fails between the two halves of the TPC, and where there is a gap between the muon chamber modules. There is a very marked gap of about $\pm 4°$ for electron identification. The physical reason for this is a substantial gap in the HPC module coverage in this region because of equipment for the magnet. This zone

Figure 4.11: Theta distributions of tagged tracks in the 1989 data. Plot (a) is of tracks identified with cut $\dagger_{B7}$, and consists mainly of muons, while plot (b) is of tracks identified with cut $\dagger_{A6}$, and consists mainly of electrons. The arrows mark the limits of proposed theta cuts about 90° in the data selection.

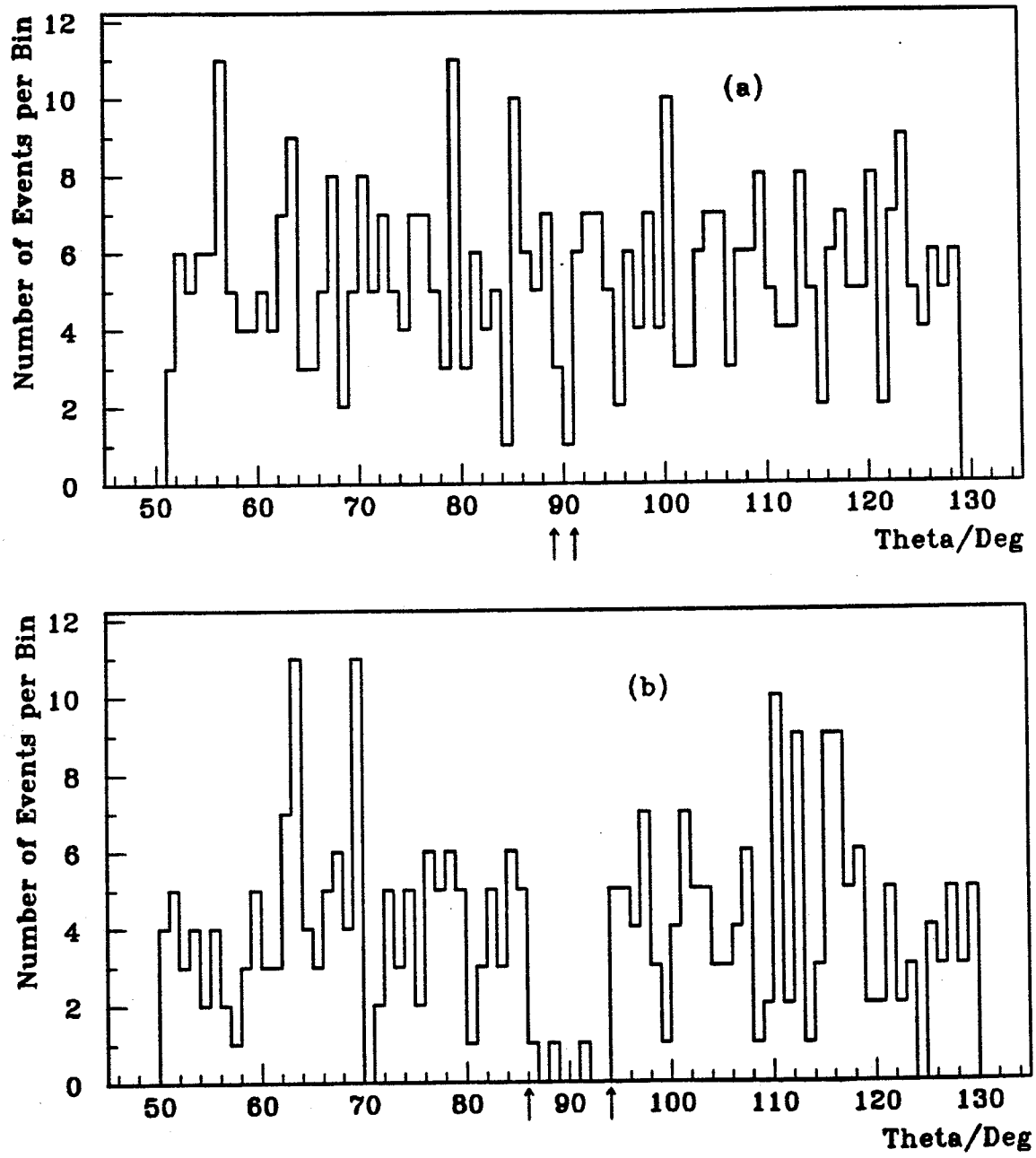

Analysis Conditions	
Data sample	Runs 3302 - 6057
Analysis package	DELANA31,GEDTAN
Selection cuts	$\dagger_{A1}$,$\dagger_{A2}$,$\dagger_{A3}$,$\dagger_{A4}$, $\dagger_{B7}$(plot (a)),$\dagger_{A6}$(plot (b))

is covered by scintillator/lead sandwich blocks, designed to provide only crude shower information and identification of minimum ionizing particles. However, this equipment was not functioning correctly during the 1989 runs. It is necessary, therefore, to add a further cut for the Bhabha sample,

$$\boxed{\dagger_{A9}\text{: } |\theta - 90°| \geq 4° \text{ for both the highest momenta tracks.}} \tag{4.10}$$

and a cut will also be added for the dimuon sample of

$$\boxed{\dagger_{A10}\text{: } |\theta - 90°| \geq 1° \text{ for both the highest momenta tracks.}} \tag{4.11}$$

This will restrict the data to regions of positive particle identification.

4.10 Simulation Data Studies using the Dilepton Selection Cuts

It is now instructive to see the effect of these cuts that have been deduced from the *real* data on the three simulated data samples discussed in section 4.3. The Tables 4.1 and 4.2 show how the data samples are cumulatively reduced by the cuts defined previously.

Table 4.1: The effects of the first pass dimuon selection cuts on the dimuon and ditau simulated data samples.

Cuts applied	$\mu\mu$	$\tau\tau$
Total Sample Size	8639	8998
$\dagger_{A1}$	4351	3964
$\dagger_{A1},\dagger_{A10}$	4263	3869
$\dagger_{A1},\dagger_{A2},\dagger_{A10}$	4186	3314
$\dagger_{A1},\dagger_{A2},\dagger_{B7},\dagger_{A10}$	4173	496
$\dagger_{A1},\dagger_{A2},\dagger_{A3},\dagger_{B7},\dagger_{A10}$	4136	381
$\dagger_{A1},\dagger_{A2},\dagger_{A3},\dagger_{A4},\dagger_{B7},\dagger_{A10}$	4108	196
$\dagger_{A1},\dagger_{A2},\dagger_{A3},\dagger_{A4},\dagger_{B7},\dagger_{A8},\dagger_{A10}$	4108	196

Table 4.2: The effects of the first pass Bhabha selection cuts on the Bhabha and ditau simulated data samples.

Cuts applied	ee	$\tau\tau$
Total Sample Size	4098	8998
$\dagger_{A1}$	3537	3964
$\dagger_{A1},\dagger_{A9}$	3220	3525
$\dagger_{A1},\dagger_{A2},\dagger_{A9}$	3147	3028
$\dagger_{A1},\dagger_{A2},\dagger_{A6},\dagger_{A9}$	2957	183
$\dagger_{A1},\dagger_{A2},\dagger_{A3},\dagger_{A6},\dagger_{A9}$	2872	136
$\dagger_{A1},\dagger_{A2},\dagger_{A3},\dagger_{A4},\dagger_{A6},\dagger_{A9}$	2730	52

This analysis points out an interesting feature. It is apparent that the dimuon events are 'cleaner' than the Bhabha events. The cuts $\dagger_{A3}$ and $\dagger_{A4}$ which demand a maximum of two charged tracks above 1GeV/c and that both these tracks have momenta greater than 10GeV/c, reduce the dimuon sample passing the $\dagger_{A1}$ cut by a further 1.4%, after the other cuts have been applied, but reduce the Bhabhas by 6.4%. Under the same conditions the ditaus passing the $\dagger_{A1}$ cut are

reduced by 6.7% and 3.3% after all the other dimuon and Bhabha cuts have been applied respectively. If the *assumption* of an approximate lepton universality in the Z° decay products is made, then the application of cuts $\dagger_{A3}$ and $\dagger_{A4}$, after the other cuts have been made, is *beneficial* to the dimuon analysis, since the fractional reduction of the ditau background is greater than the loss of signal, but is *detrimental* to the Bhabha analysis where the reverse effect takes place. These cuts will therefore not be used for Bhabha selection.

4.11 Momentum Cuts: Second Iteration

Now that cut $\dagger_{B7}$ for muon identification has been defined it is instructive to look back at the real data to see if the momentum cut $\dagger_{A4}$ may be improved for the dimuon sample. Fig. 4.12 shows the normalized inverse momentum distributions for the 1989 data and the simulated data.

The inverse momentum is plotted because the quantity actually measured in DELPHI is the radius of curvature of the tracks in the magnetic field, which is inversely proportional to the particle momenta. All the muon selection cuts have been applied *except* for the momentum cut itself, and the inverse momenta of both the highest momenta tracks have been plotted for each event. The simulated distribution has been produced by combining the normalized distributions from the dimuon simulation and the ditau simulation in the ratio (0.923 : 0.077), which is the ratio predicted when the other cuts are taken into account, *assuming* an approximate lepton universality. The distortion from cosmic background muons is assumed to be small. The plots show that the dimuon peak lies well within the 10GeV/c cut, and this can easily be tightened to 15GeV/c. The plots also show that the real and simulation data converge at lower momenta. However the dimuon peak is considerably broader for the real data, which indicates that the momentum resolution of high momenta tracks is poorer than that modelled in the simulation. One third of the real data plotted were taken under the condition of a half strength magnetic field, and this is partially responsible for the degradation of the performance. The final alignments of the tracking detectors have not yet been determined either in this early data which also contributes a detrimental effect. However the plots show that the precision obtained is sufficient to identify

Figure 4.12: Normalized inverse momentum distributions for the 1989 data (full line) and simulation data (broken line) over the ranges (0.032 to 0.136)GeV^{-1} (plot(a)) and (0 to 0.190)GeV^{-1} (plot(b)). The dimuon contribution to the simulated distribution is separately picked out in a hashed distribution on plot (a). Statistical error bars are also added to some of the real data points. The 10GeV/c and 15GeV/c momentum cuts are indicated.

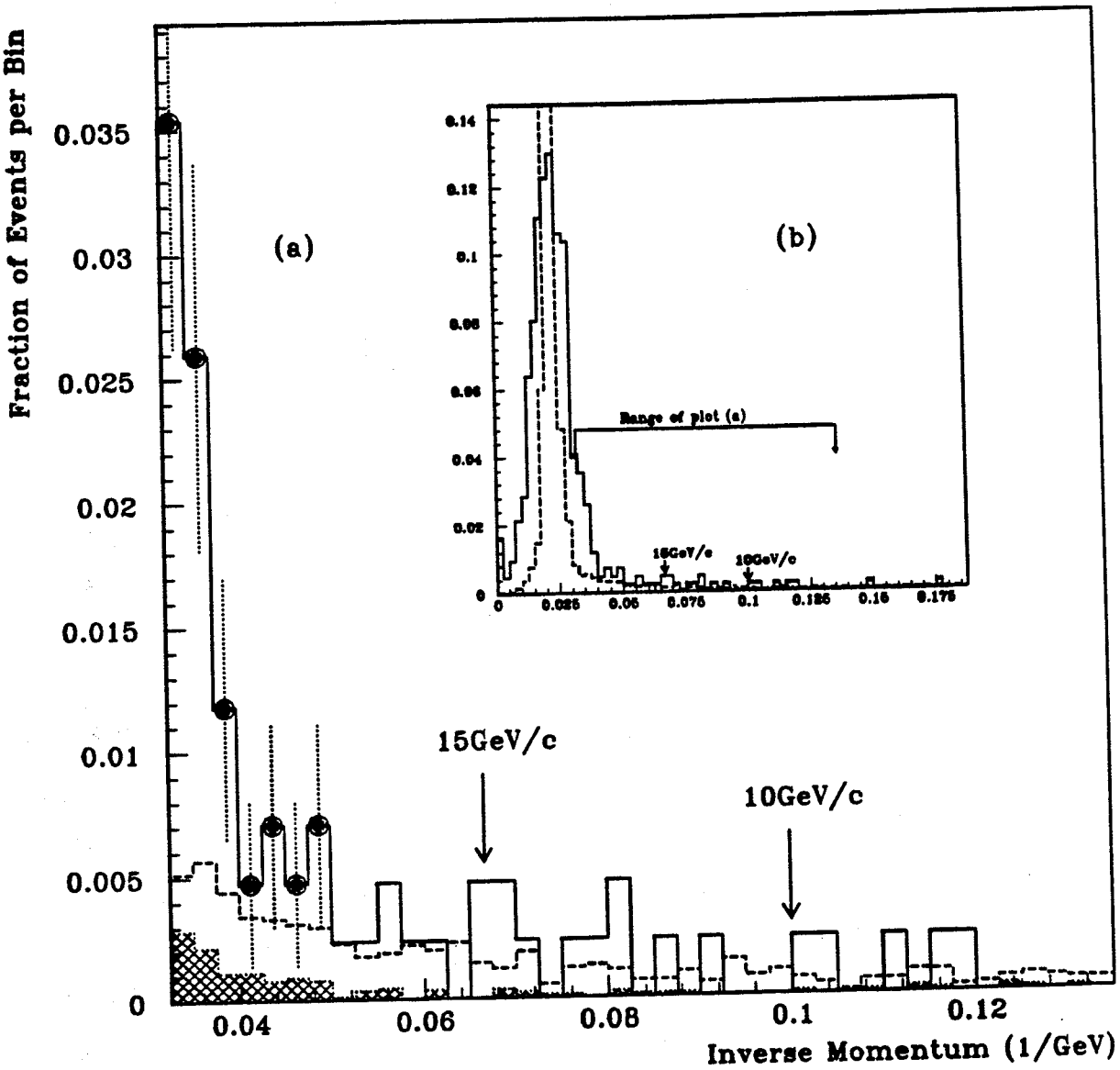

Analysis Conditions	
Real data sample	Runs 3302 - 6057
Analysis package	DELANA31,GEDTAN
Selection cuts	$\dagger_{A1}$,$\dagger_{A2}$,$\dagger_{A3}$, $\dagger_{B7}$,$\dagger_{A8}$,$\dagger_{A10}$
Detector simulation	DELSIM35
Dimuon generator and sample size	DYMU3: 8639 events
Ditau generator and sample size	KORALZ: 8998 events

dimuons above 15GeV/c, and the agreement with the simulation below 15GeV/c gives confidence in the simulation for modelling the background and signal loss. The fraction of tracks with momenta less than 15GeV/c in the real data is for this sample (0.050 ± 0.011), whereas for the simulation data it is (0.072 ± 0.002) - where the errors are statistical in both cases. Therefore, within the resolution of these samples the real and simulation data are in agreement (within 2σ) and a new momentum cut may therefore be defined for the dimuon selection:

$\dagger_{B4}$: $P_1 \geq 15.0$GeV/c and $P_2 \geq 15.0$GeV/c where P_1 and P_2 are the momenta of the two highest momenta tracks. (4.12)

4.12 Studies of the Simulated Ditau Background

The GEDTAN analysis program decodes the original simulated event generation banks and it is instructive to examine the *kinds* of ditau decays that constitute the background that will pass the two different dimuon identification cuts and the Bhabha selection cuts. This can be used as a means of checking whether the background in the simulation makes physical sense. Four tables are shown below in which the two tau's decay to any combination of two charged track final states. Table 4.3 shows all the decay combinations that take place in 8998 simulated events. Table 4.4 shows decays passing the selection cut $\dagger_{A5}$ (positive MUB identification) as means of muon identification as well as the other standard dimuon cuts. Table 4.5 shows decays passing the the selection cut $\dagger_{A7}$ (positive HPC identification), Table 4.6 shows those decays passing the combined $\dagger_{B7}$ dimuon selection cut and Table 4.7 shows those passing the Bhabha selection cuts.

Many of the results of this analysis are what is expected. For the dimuon cuts with MUB identification only (Table 4.4), out of 69 ditaus passing the cuts 62 (89%) have at least one tau decaying to a muon, and 29 (42%) are events in which both taus decay to muons. The only other particles identified by the MUB in this analysis are pions. This is to be expected since pion punchthrough at the

Table 4.3: Numbers in each category of 1-1 topology simulated $\tau^+\tau^-$ decays.

$\tau^+\tau^- \rightarrow$	$\rho^\pm$	$\mu^\pm$	$e^\pm$	$\pi^\pm$	$K^\pm$	$\pi^\pm\pi^0\pi^0$	$\pi^\pm\pi^0\pi^0\pi^0$
$\rho^\pm$	469	726	742	457	55	317	193
$\mu^\pm$		301	604	382	49	258	168
$e^\pm$			300	363	57	237	167
$\pi^\pm$				117	23	171	106
$K^\pm$					4	23	20
$\pi^\pm\pi^0\pi^0$						67	70
$\pi^\pm\pi^0\pi^0\pi^0$							25

Table 4.4: Numbers in each category of 1-1 topology simulated $\tau^+\tau^-$ decays passing dimuon cuts with MUB identification only. The selection cuts applied are $\dagger_{A1}$,$\dagger_{A2}$,$\dagger_{A3}$, $\dagger_{B4}$,$\dagger_{A5}$,$\dagger_{A8}$,$\dagger_{A10}$.

$\tau^+\tau^- \rightarrow$	$\rho^\pm$	$\mu^\pm$	$e^\pm$	$\pi^\pm$	$K^\pm$	$\pi^\pm\pi^0\pi^0$	$\pi^\pm\pi^0\pi^0\pi^0$
$\rho^\pm$	1	5	0	4	0	0	0
$\mu^\pm$		29	0	20	0	5	3
$e^\pm$			0	0	0	0	0
$\pi^\pm$				1	0	0	1
$K^\pm$					0	0	0
$\pi^\pm\pi^0\pi^0$						0	0
$\pi^\pm\pi^0\pi^0\pi^0$							0

level of 1 - 2% was seen in the HFM test beam experiment, and there are only 4 - 5 hadronic absorption lengths provided by the HCAL before the first layer of muon chambers. This background may be reduced by demanding hits in the outer and peripheral layers of muon chambers or by demanding that the muon chamber hits line up along a straight line passing through the centre of DELPHI. Pions will tend to be scattered to a greater extent and will fall outside this cut

Table 4.5: Numbers in each category of 1-1 topology simulated $\tau^+\tau^-$ decays passing dimuon cuts with HPC identification only. The selection cuts applied are $\dagger_{A1}$,$\dagger_{A2}$,$\dagger_{A3}$, $\dagger_{B4}$,$\dagger_{A7}$,$\dagger_{A8}$,$\dagger_{A10}$.

$\tau^+\tau^- \rightarrow$	$\rho^\pm$	$\mu^\pm$	$e^\pm$	$\pi^\pm$	$K^\pm$	$\pi^\pm\pi^0\pi^0$	$\pi^\pm\pi^0\pi^0\pi^0$
$\rho^\pm$	1	8	0	1	0	0	0
$\mu^\pm$		28	0	40	3	1	0
$e^\pm$			0	0	0	0	0
$\pi^\pm$				7	2	0	0
$K^\pm$					0	0	0
$\pi^\pm\pi^0\pi^0$						0	0
$\pi^\pm\pi^0\pi^0\pi^0$							0

Table 4.6: Numbers in each category of 1-1 topology simulated $\tau^+\tau^-$ decays passing dimuon cuts with HPC or MUB identification. The selection cuts applied are $\dagger_{A1}$,$\dagger_{A2}$,$\dagger_{A3}$, $\dagger_{B4}$,$\dagger_{B7}$,$\dagger_{A8}$,$\dagger_{A10}$.

$\tau^+\tau^-\rightarrow$	$\rho^\pm$	$\mu^\pm$	$e^\pm$	$\pi^\pm$	$K^\pm$	$\pi^\pm\pi^0\pi^0$	$\pi^\pm\pi^0\pi^0\pi^0$
$\rho^\pm$	2	13	0	5	0	0	0
$\mu^\pm$		31	0	43	3	5	3
$e^\pm$			0	0	0	0	0
$\pi^\pm$				7	2	0	1
$K^\pm$					0	0	0
$\pi^\pm\pi^0\pi^0$						0	0
$\pi^\pm\pi^0\pi^0\pi^0$							0

Table 4.7: Numbers in each category of 1-1 topology simulated $\tau^+\tau^-$ decays passing Bhabha selection cuts. The selection cuts applied are $\dagger_{A1}$,$\dagger_{A2}$,$\dagger_{A6}$,$\dagger_{A9}$.

$\tau^+\tau^-\rightarrow$	$\rho^\pm$	$\mu^\pm$	$e^\pm$	$\pi^\pm$	$K^\pm$	$\pi^\pm\pi^0\pi^0$	$\pi^\pm\pi^0\pi^0\pi^0$
$\rho^\pm$	25	0	34	9	1	15	4
$\mu^\pm$		0	0	0	0	0	0
$e^\pm$			19	5	1	18	11
$\pi^\pm$				0	0	3	1
$K^\pm$					0	1	0
$\pi^\pm\pi^0\pi^0$						5	8
$\pi^\pm\pi^0\pi^0\pi^0$							5

(see ref. [35] on the HFM experiment). However the background is already low and these criteria will not be applied since the strategy at this early stage of running, when the detector is still being calibrated and statistics are low, is to maintain loose cuts, and try to accurately estimate the background.

In the case of the dimuon cuts with HPC identification only (Table 4.5) out of 91 ditaus passing the cuts 80 (88%) have at least one tau decaying to a muon, and 28 (31%) are events in which both taus decay to muons. Most of the other particles identified by the muon cuts are pions, although 5 kaons also pass the cuts. An interesting feature though is that when π^0's are produced in conjunction with $\pi^\pm$'s the fraction passing the selection cuts is greatly reduced: 50/1619 (3.1%) with at least one $\tau \rightarrow \pi^\pm$ decay; 10/2959 (0.3%) with at least one $\tau \rightarrow \rho^\pm \rightarrow \pi^\pm\pi^0$ decay; 1/1143 ($\sim$ 0.1%) with at least one $\tau \rightarrow \pi^\pm\pi^0\pi^0$ decay; and none where $3\pi^0$'s are generated. The explanation for this is that π^0's subsequently decay within about 10^{-16}sec to $\gamma\gamma$. These high energy photons are projected through DELPHI within a few degrees of the charged particle track and are picked up in

the HPC causing a large energy deposit which then vetos the charged pion as a muon candidate. This also has an effect on the Bhabha background as is seen in Table 4.7, as it can cause a sufficient energy deposition to identify the pion as an electron. Two plots of the high energy photons generated within 25° of the final state charged track in a tau decay are shown in Fig. 4.13. These are

Figure 4.13: A study of the photons emitted in simulated ditau events. The plots show the photon parameters of energy and angular deviation from the final state charged track in the tau decay. Plot (a) is a scatter plot; plot (b) is the same plot smoothed and then displayed as a contour map.

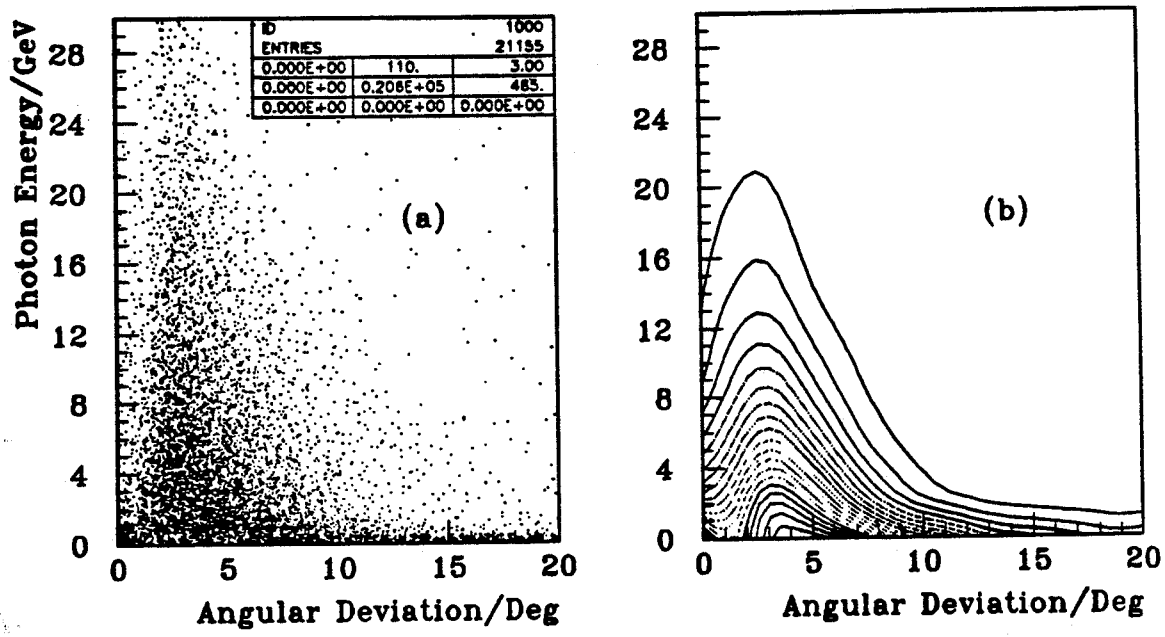

Analysis Conditions	
Analysis package	DELANA31,GEDTAN
Detector simulation	DELSIM35
Event generator and sample size	KORALZ: 8998 events
Selection cuts	The photon is emitted less than 25° from the charged track

two-dimensional plots of the photon energy versus the angular deviation from the tracks and show that most of the photons are projected within about 3° of the charged track, and have energies that can range up to 20GeV and more. Therefore this is the effect responsible for vetoing pions in muon identification, and increasing the pion background in the Bhabha identification.

4.13 Track Reconstruction Failure

As mentioned in Section 4.1, tracks appear to be lost in the ϕ regions near the TPC cracks. Now that the selection criteria have been chosen it is worth checking this effect and testing whether or not it is correctly modelled by the simulation. A plot can be made of modulo$(\phi, 60)$ so that all the cracks in the TPC read-out pads line up at 30°. This is done for the 1989 data and the simulation data in Fig. 4.14.

An estimate of the data loss within the crack can be done by splitting the plot into five equal sections in modulo$(\phi, 60)$ and comparing the number within the central segment to the average of the the other four. The difference between these is an estimate of the loss due to the crack assuming the true distribution of generated particles is uniform. The real data have an estimated loss of $(6.3 \pm 1.2)\%$ while the simulated data have an estimated loss of $(5.72 \pm 0.37)\%$. It is therefore not possible to resolve a difference between them with these statistics and it will be assumed, since this loss depends on the detector geometry rather than the calibration constants, that the simulation correctly models the detector behaviour.

4.14 Summary of the 1989 Event Selection

The cuts to be used in event selection for the 1989 data are now summarized in Tables 4.8 and 4.9.

The number of events that pass the cuts at each energy in the 1989 data is shown in Table 4.10.

4.15 Cosmic Background

The cosmic background at each energy can be calculated in the following way. A plot of r against the z value at the minimum r of a track for all events passing the dimuon cuts *except* the vertex cut is shown in Fig. 4.15. There is, as expected, a concentration around the origin of DELPHI, and then a background distribution which is uniform up to about $|z| = 10$cm and $r = 8$cm. This is assumed to be the background cosmic distribution. By calculating its density over the r-z

Figure 4.14: The normalized distributions in modulo(ϕ, 60) of tracks that pass the dimuon selection cuts in the 1989 (solid line) and simulation data (broken line). A segment of DELPHI viewed over this angular range is also shown.] The gaps in the TPC read-out pads all lie at 30° in this plot. The region ±1.5° on either side of the crack is marked.

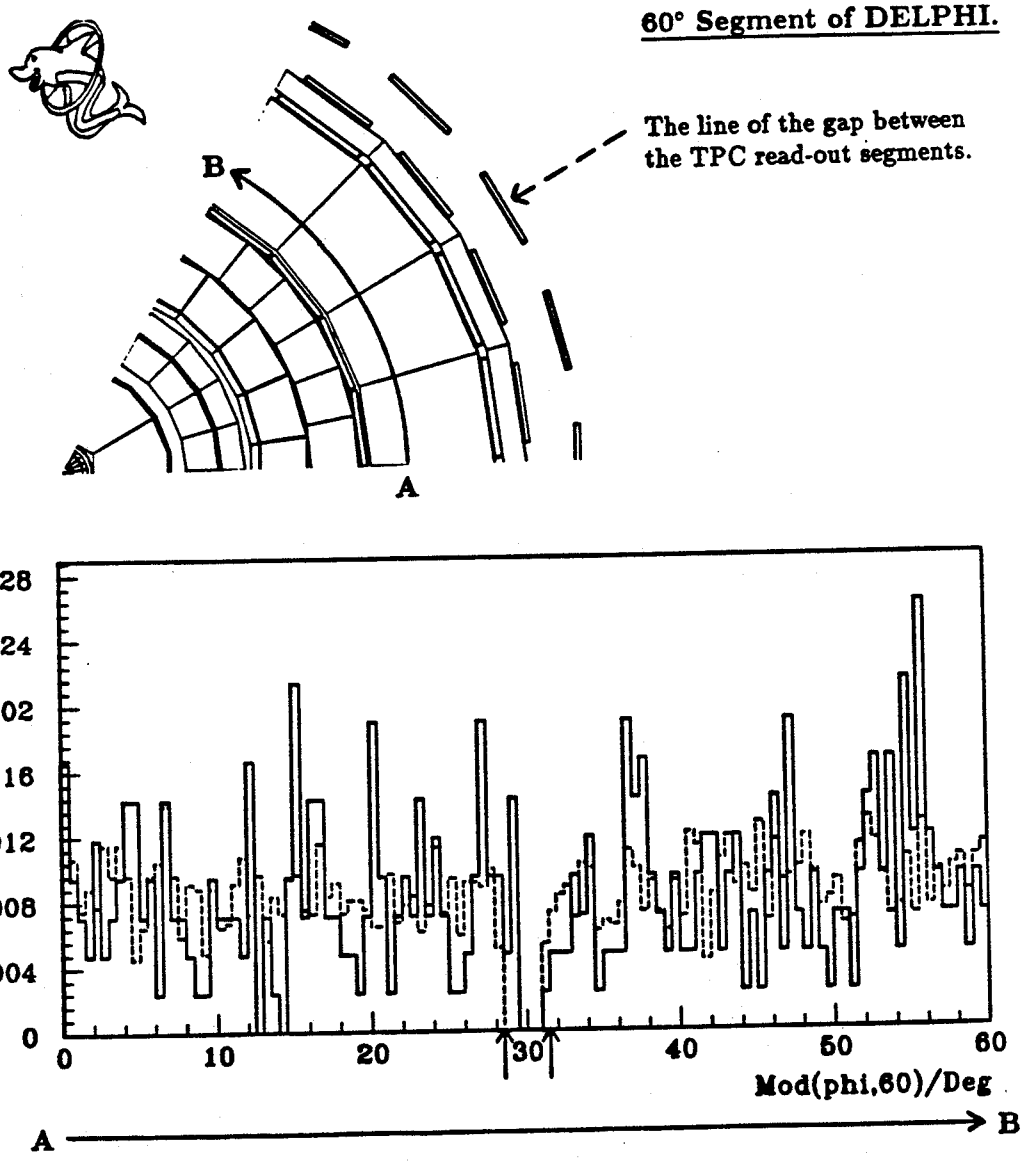

Analysis Conditions	
Data sample	Runs 3302 - 6057
Analysis package	DELANA31,GEDTAN
Detector simulation	DELSIM35
Dimuon generator and sample size	DYMU3: 8639 events
Selection cuts	$\dagger_{A1}$,$\dagger_{A2}$,$\dagger_{A3}$, $\dagger_{B4}$,$\dagger_{B7}$,$\dagger_{A10}$

Table 4.8: A summary of the dimuon selection cuts for the 1989 data. The cut $\dagger_\mu$ represents the combination of all the selection criteria.

$\dagger_{A1}$	The two tracks with the highest momenta satisfy $50° \leq \theta \leq 130°$.
$\dagger_{A2}$	The two tracks with the highest momenta are acolinear within 10°.
$\dagger_{A3}$	A maximum number of two charged tracks have a momentum greater than 1GeV/c.
$\dagger_{B4}$	$P_1 \geq 15$GeV/c and $P_2 \geq 15$GeV/c where P_1 and P_2 are the momenta of the two highest momenta tracks.
$\dagger_{B7}$:	$[0 < E^A_{HPC} < 2$GeV or $N_A \geq 1]$ and $[0 < E^B_{HPC} < 2$GeV or $N_B \geq 1]$ where E^A_{HPC} and E^B_{HPC} are the energies deposited within 10° of each of the two highest momenta tracks, and N_A and N_B are the number of MUB chambers hit within 10° of each of these tracks.
$\dagger_{A8}$	$r \leq 0.8$cm and $(-4.3 \leq z \leq +3.7)$cm for both the highest momenta tracks.
$\dagger_{A10}$	$\lvert\theta - 90°\rvert \geq 1°$ for both the highest momenta tracks.
$\dagger_\mu$	$\dagger_{A1} \cap \dagger_{A2} \cap \dagger_{A3} \cap \dagger_{B4} \cap \dagger_{B7} \cap \dagger_{A8} \cap \dagger_{A10}$

Table 4.9: A summary of the Bhabha selection cuts for the 1989 data. The cut $\dagger_e$ represents the combination of all the selection criteria.

$\dagger_{A1}$	The two tracks with the highest momenta satisfy $50° \leq \theta \leq 130°$.
$\dagger_{A2}$	The two tracks with the highest momenta are acolinear within 10°.
$\dagger_{A6}$	$E^A_{HPC} \geq 25$GeV and $E^B_{HPC} \geq 10$GeV where E^A_{HPC} and E^B_{HPC} are the energies deposited within 10° of each of the two highest momenta tracks.
$\dagger_{A9}$	$\lvert\theta - 90°\rvert \geq 4°$ for both the highest momenta tracks.
$\dagger_e$	$\dagger_{A1} \cap \dagger_{A2} \cap \dagger_{A6} \cap \dagger_{A9}$

plane the number of background cosmic events *within* the vertex region (defined by cut $\dagger_{A8}$) can be estimated assuming the density is uniform. The vertex region covers 6.4cm^2 while the rest of this area has 153.6cm^2. The estimated number of events within the vertex cut $N_{CV} = (6.4/153.6) \times N_C$, where N_C is the number of cosmics outside the vertex region. The results for different centre-of-mass energies are shown in Table 4.11.

Table 4.10: Events passing dimuon and Bhabha selection cuts at each centre of mass energy in the 1989 data.

Energy	$\dagger_\mu$	$\dagger_e$
88.28	7	9
89.28	7	11
90.28	14	29
91.04	25	30
91.28	40	29
91.54	70	67
92.28	11	13
93.28	21	11
94.28	6	4
95.04	3	4
TOTAL	204	207

Figure 4.15: The values of r (distance along the beam axis) and z (displacement along the beam axis) at minimum r for tracks passing the muon selection cuts in the 1989 data.

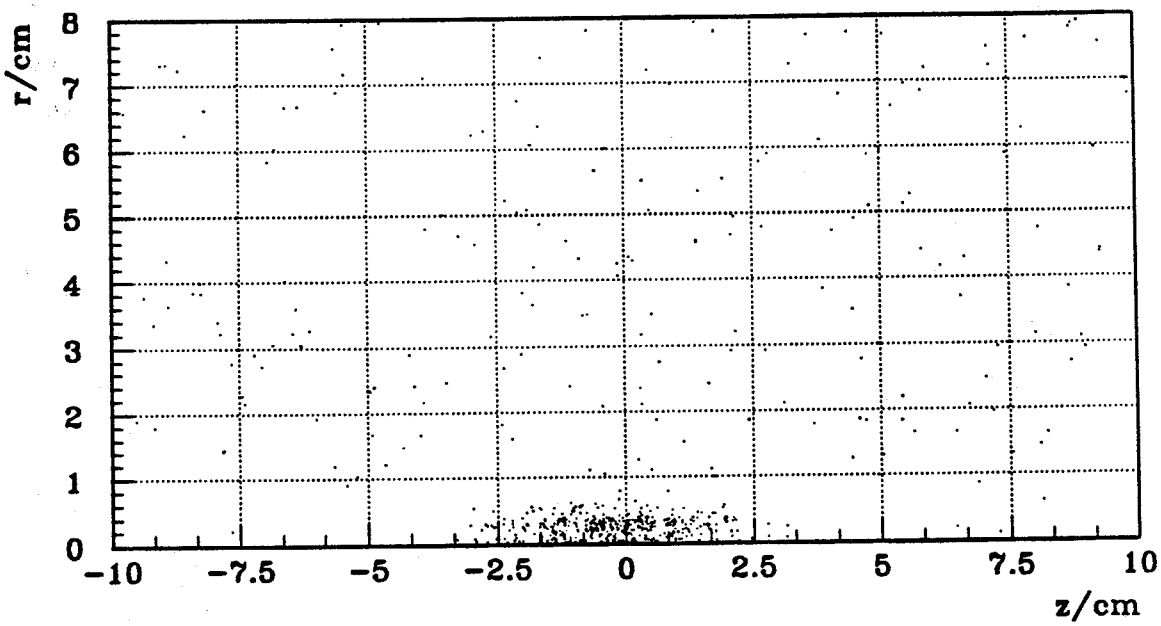

Analysis Conditions	
Data sample	Runs 3302 - 6057
Analysis package	DELANA31,GEDTAN
Selection cuts	$\dagger_{A1}$,$\dagger_{A2}$,$\dagger_{A3}$, $\dagger_{B4}$,$\dagger_{B7}$,$\dagger_{A10}$

Table 4.11: Cosmic background to the dimuon sample in the 1989 data.

Energy	Cosmics outside the $\dagger_{A8}$ vertex cut	Estimated cosmic contamination within the $\dagger_{A8}$ vertex cut
88.28	7	0.29 ± 0.11
89.28	2	0.08 ± 0.06
90.28	11	0.46 ± 0.14
91.04	17	0.71 ± 0.17
91.28	15	0.62 ± 0.16
91.54	22	0.92 ± 0.20
92.28	10	0.42 ± 0.04
93.28	6	0.25 ± 0.10
94.28	2	0.08 ± 0.06
95.04	3	0.12 ± 0.07
TOTAL	**95**	$\mathbf{3.96 \pm 0.41}$

4.16 Ditau Studies

In order to compute the ditau contamination in the Bhabha and dimuon samples it is necessary to be able to estimate the *fraction* of ditau events passing the dimuon and Bhabha cuts, and also the *absolute* number of ditaus produced. The normal procedure is to *assume* an approximate lepton universality which then circumvents the need to know the second variable. As the tau contamination is normally of the order of a few percent, the fact that this assumption is made is not of very great significance. However, as lepton universality is one of the hypotheses being tested by this analysis, it is as well not to fold it into any calculation without some attempt to make a first iteration test. The GEDTAN program is not designed for a ditau analysis, as it is primarily intended for two track events where both tracks have high momenta. However it is possible to use the information that is available to make a crude estimate of the number of ditau events. In fact the ratio of dimuons to ditaus will be calculated as it is then possible to use the simulated event samples directly, relying on most of the systematic problems arising from trigger efficiency or incorrectly simulated data samples to cancel out in the calculation.

One possibility is to use the analysis tools developed in previous sections to identify events corresponding to particular tau channels, and thereby estimate the total number of ditau events. A characteristic signal of a ditau event would be a

track identified as a muon or a single pion on one side of the barrel, giving a hit in the MUB or an energy deposition in the HPC in the range $(0 < E < 2)$GeV, and the acolinear track giving a large energy deposition in the electromagnetic calorimeter. (> 3GeV). This track would probably be an electron, or pion with associated hard photons. The standard cuts $\dagger_{A1}$ and $\dagger_{A9}$ can also be added to restrict the sample to active regions of the MUB and HPC, and an acolinearity cut of 20° to exclude unusual beam gas events. The vertex cut $\dagger_{A8}$ should also be added. This combination of cuts will be signified by the symbol $\dagger_\tau$. The number of events passing these cuts at each energy is shown in Table 4.12.

Table 4.12: The number of events passing the ditau selection cut at each energy.

Energy	Events found
88.28	2
89.28	2
90.28	5
91.04	13
91.28	13
91.54	25
92.28	6
93.28	3
94.28	1
95.04	0
TOTAL	**70**

The ditau sample obtained contains a small fraction of dimuons, and likewise the dimuon sample contains some ditaus. There is a smaller contamination of the ditau sample by Bhabhas as well. If this is discounted then all the possible constituents of the real and measured data samples are shown in the venn diagram of Fig. 4.16.

Areas outside the region of the real samples are background events such as beam gas and cosmics. Region **C** represents the cosmic background to the dimuon sample estimated in Section 4.15. Regions **H** and **F** are found to contain no events, as no cosmics are found to satisfy the $\dagger_\tau$ conditions. If τ_M and μ_M represent the measured number of events passing cuts $\dagger_\tau$,$\dagger_\mu$ and τ_R and μ_R represent the real number of ditau and dimuon events then:

Figure 4.16: A Venn Diagram showing the possible constituents of the dimuon and ditau measured event samples.

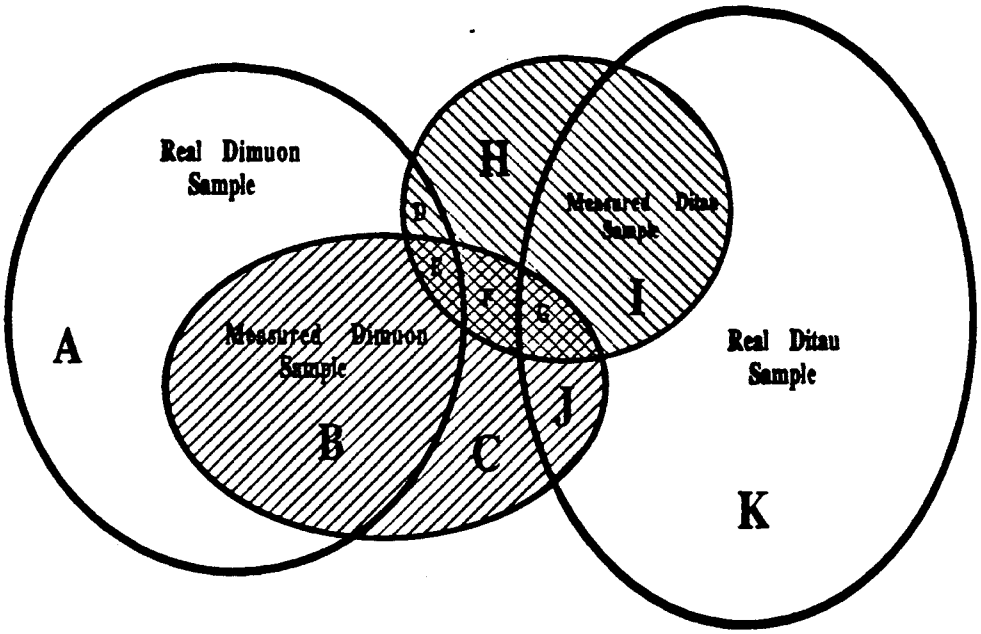

$$\begin{pmatrix} \mu_R \\ \tau_R \end{pmatrix} = \frac{1}{(S_3 S_4 - S_1 S_2)} \begin{pmatrix} S_4 & -S_2 \\ -S_1 & S_3 \end{pmatrix} \begin{pmatrix} \mu_M \\ \tau_M \end{pmatrix} \tag{4.13}$$

where the cosmic ray background has already been subtracted from μ_M. This equation makes no *a priori* assumptions about the relative numbers of ditaus and dimuons, each of which is a background to the other. S_1 is the fraction of ditau identifications in the real dimuon sample (the regions $\mathbf{(D + E)/(A + B + D + E)}$, S_2 is the fraction of dimuon identifications in the real ditau sample (the regions $\mathbf{(G + J)/(G + J + I + K)}$, S_3 is the fraction of dimuon identifications in the real dimuon sample (the regions $\mathbf{(B + E)/(A + B + D + E)}$, and S_4 is the fraction of ditau identifications in the real ditau sample (the regions $\mathbf{(G + I)/(G + J + I + K)}$. These four quantities may be estimated directly from the simulation data samples. The values for S_1, S_2, S_3 and S_4 are found to be 0.030,0.014,0.474 and 0.164.

When combined with the results from previous sections of the number of events in the dimuon sample after cosmic subtraction, Equation 4.13 becomes:

$$\begin{pmatrix} \mu_R \\ \tau_R \end{pmatrix} = \begin{pmatrix} 2.121 & -0.176 \\ -0.390 & 6.129 \end{pmatrix} \begin{pmatrix} (200 \pm 14(\text{stat})) \\ (70 \pm 8(\text{stat})) \end{pmatrix} \tag{4.14}$$

Therefore the computed real number of dimuons is 412 in a perfect event sample (4π coverage and 100% efficiency) and the real number of ditaus is 351. However there is a large statistical error on both these quantities:

$$\mu_R = (412 \pm 30); \tag{4.15}$$

$$\tau_R = (351 \pm 49). \tag{4.16}$$

This gives

$$\tau_R/\mu_R = (0.85 \pm 0.14). \tag{4.17}$$

This result is compatible with lepton universality, and for the purposes of calculating tau contamination of a few percent to the dimuon and Bhabha samples, any deviation from lepton universality within the limits allowed by this measurement will bias the corrected samples by less than 1%.

4.17 Comparative Behaviour of the 1989 and Simulation Data

An attempt is made here to evaluate the performance of the simulation, in particular in those areas where the simulation is crucial to measurement of the efficiencies and backgrounds of the leptonic samples. Already comparisons have been made between real and simulation data for the energy spectrum of muons in the HPC (Fig. 4.9), the inverse momentum distributions of events passing the dimuon cuts (Section 4.11) and the losses due to track reconstruction failure (Section 4.13). From these studies it appears that the simulation and the real data are in good agreement in the following cases: for the HPC in the regime of low energy deposition; for low track momenta (the inverse momentum spectra converge below about 20GeV/c); and for track reconstruction failure - where it is not possible to resolve any difference in terms of percentage track loss. However, no attempt has been made yet to compare the acolinearity distributions, the dimuon detection efficiency or the HPC simulation at high energies - which is important for the Bhabha studies. These studies are set out in the sections below.

4.17.1 Acolinearity

The acolinearity distributions of the two highest momenta tracks in the dimuon and Bhabha samples for both real and simulation data are shown in Fig. 4.17.

The dimuon distribution is obtained in the following way. The cuts $\dagger_{A1}$, $\dagger_{A3}$, $\dagger_{B4}$,$\dagger_{B7}$,$\dagger_{A8}$ and $\dagger_{A10}$ are applied to the real data sample and the dimuon and ditau simulated data samples. An acolinearity cut of 20° is also placed on the samples, which enables a study of the behaviour through the 10° region to be made, but which excludes any peculiar beam gas events. As the real dimuon sample is contaminated by cosmics at the 2% level, an analysis is also done on a sample of 2000 cosmics that would pass these cuts. The simulated data distributions are then normalized to unit area and combined in a ratio of dimuons,ditaus and cosmics of (0.955 : 0.025 : 0.020) which are the ratios predicted to pass the cuts assuming an approximate lepton universality. The Bhabha comparison is done in a similar way, with Bhabhas and ditaus being combined in the ratio (0.961 : 0.039)

Figure 4.17: The acolinearity distributions of 1989 (solid line) and simulation data (dashed line) using the cuts, except the acolinearity cut, for dimuon and Bhabha selection (plots (a) and (b)). Statistical error bars are added to a few 1989 data points.

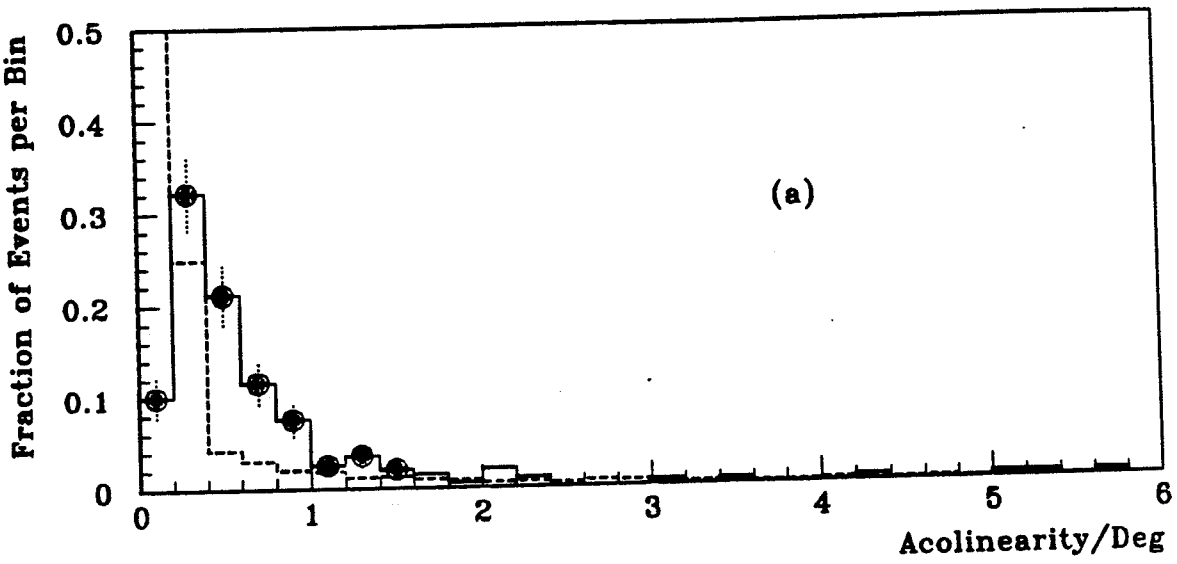

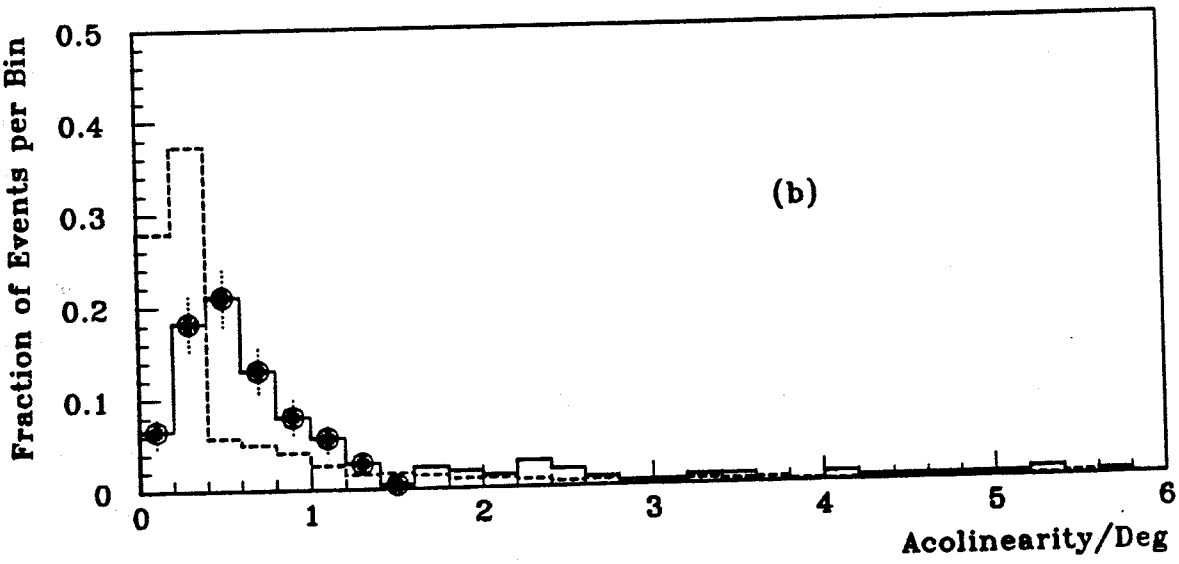

Analysis Conditions	
1989 data sample	Runs 3302 - 6057
Analysis package	DELANA31,GEDTAN
Detector simulation	DELSIM35
Bhabha generator and sample size	BABAMC: 4098 barrel events
Dimuon generator and sample size	DYMU3: 8639 events
Ditau generator and sample size	KORALZ: 8998 events
Selection cuts: plot(a)	$\dagger_{A1}$,$\dagger_{A3}$,$\dagger_{B4}$, $\dagger_{B7}$,$\dagger_{A8}$,$\dagger_{A10}$
Selection cuts: plot(b)	$\dagger_{A1}$,$\dagger_{A6}$,$\dagger_{A10}$,
Simulated dimuon:ditau:cosmic ratio (plot(a))	0.955 : 0.025 : 0.020
Simulated Bhabha:ditau ratio (plot(b))	0.961 : 0.039

to obtain the simulated distributions. Although the results show that the real and simulated distributions converge to one another and to zero after a few degrees, the simulated acolinearity very poorly models the real data below about 1.5°. This is primarily due to incomplete detector alignment and calibration in the 1989 data which particularly affects measurements in the z direction of DELPHI in many sub-detectors. While the effect of a tight acolinearity cut cannot be accurately simulated, the present cut at 10° is safe.

4.17.2 Muon Identification

This section deals with the efficiency of muon identification using selection cut $\dagger_{B7}$ after all the other dimuon cuts have been applied. The first objective is to obtain a very clean dimuon sample with which to measure the efficiency. This can be done by tightening the acolinearity cut, raising the momentum requirement, and using the HPC to veto electrons. The following cuts, an acolinearity of less than 2°, a minimum momentum on each track of 20GeV/c and an exclusion of events with more than 4GeV associated in the HPC on either track gives a sample of 185 events in the 1989 data. The standard vertex and angular cuts for dimuons have also been applied. These cuts could not be used for reconstructing the original number of the dimuons because of the divergence between the real and simulation data under these conditions. However, they are suitable for selecting a pure dimuon sample where the absolute size is unimportant. The simulation predicts a tau contamination for this sample of 1.0% and the effect of the simulation problems on this figure is likely to be small. The cut $\dagger_{B7}$, when applied to this sample, gives 176 events, with a predicted tau contamination of 0.9%. The problem with this method is that the HPC has already been used to veto out tracks with more than 4GeV in the HPC. However, because of the acolinearity and momentum cuts which remove most of the ditau events, the veto is only removing the Bhabhas. The probability of *both* electrons giving less than 4GeV in the HPC and thereby contaminating the dimuon sample is expected to be extremely small: the simulation predicts that no events pass these cuts. The efficiency for the identification of dimuon events can therefore be estimated as $(95.1 \pm 1.6)\%$, whereas in the simulation it is predicted to be $(99.7 \pm 0.1)\%$.

It is therefore necessary to apply a correction factor of (1.048 ± 0.018) to the reconstructed number of dimuons computed by the simulation.

4.17.3 Electron Identification

There are two problems to be solved to obtain the correction factors to the Bhabha sample. The first is to know the proportion of the sample that comes from the ditau background, and the second is to measure the HPC Bhabha identification efficiency. Other corrections are geometric in nature e.g correcting for the dead region about 90° and it will be assumed that the simulation correctly reproduces these effects. If the simulation is to provide the estimate of the ditau background it is useful to study the HPC energy spectrum of a sample of events in the real and simulation data and compare the two. The problem is in selecting a sample containing mainly Bhabhas without using the HPC itself - which would bias the sample. One solution is to use the muon chambers to cut out dimuons and some ditaus by demanding no hits in the MUB associated with either track. The other cuts are the standard ones used for selecting Bhabhas ($\dagger_{A1}$,$\dagger_{A2}$ and $\dagger_{A9}$) without the HPC cut $\dagger_{A6}$. Assuming an approximate lepton universality the resulting event sample from simulation should consist of Bhabhas, ditaus and dimuons in the ratio 0.698:0.285:0.017. The normalized spectra for simulation and real data are shown in Fig. 4.18.

The following conclusions can be drawn. The simulated energy spectrum is in reasonable agreement with the real energy spectrum up to about 25GeV. This is compatible with the earlier examination of the response of the HPC to muons where the simulation and real data also agreed well (see Fig. 4.9). Above 25GeV the electron peak at 47GeV in the simulation data is degraded to an average at about 42GeV and is smeared out to a greater extent than in the real data. This is at least partly due to the degradation of the HPC performance in the half strength magnetic field operating during one third of the data taking. Therefore the simulation does not accurately reproduce the real electron energy spectrum above 25GeV. However, for the selection of Bhabhas all that is required is that the detected energy is greater than 10GeV on one side and 25GeV on the other; the fact that a reconstructed energy is 47GeV in the simulation and 42GeV in

Figure 4.18: The spectrum of HPC energies of 1989 (solid line) and simulation data (dashed line) for a data sample of ~ 70% Bhabhas selected without the HPC. Plot(a) shows the original distributions. In plot(b) the real distribution has been smoothed. Statistical error bars are added to a few 1989 data points in plot (a).

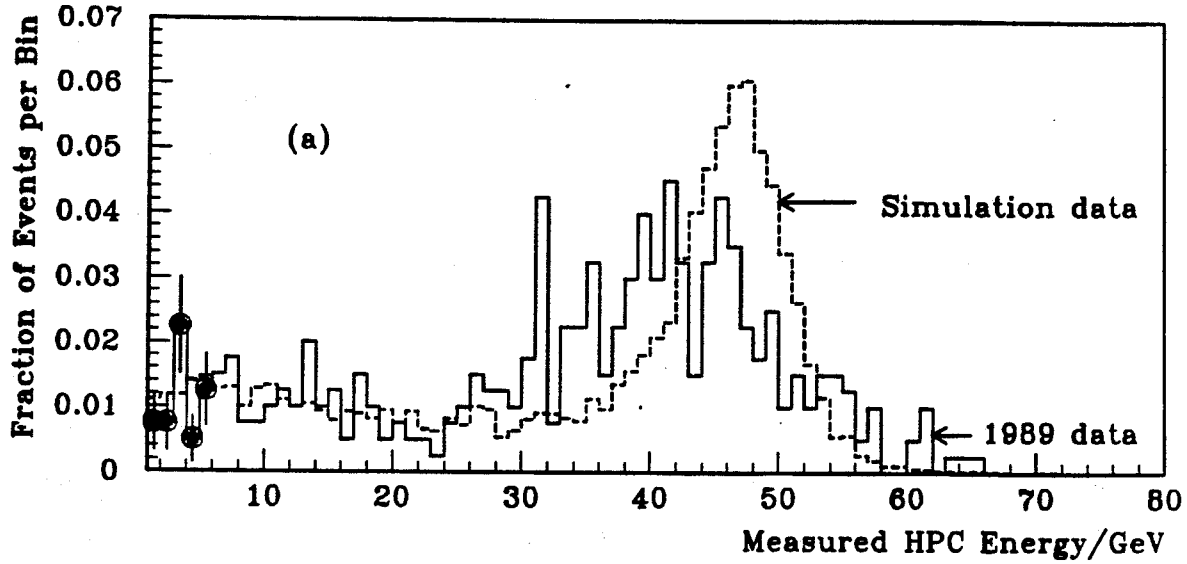

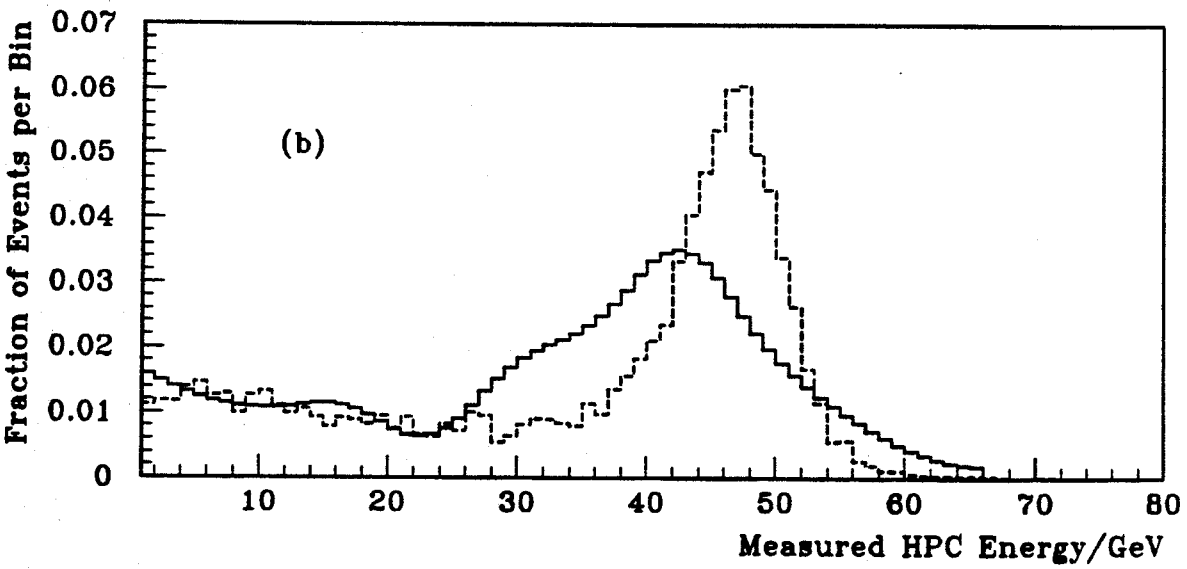

Analysis Conditions	
1989 data sample	Runs 3302 - 6057
Analysis package	DELANA31,GEDTAN
Detector simulation	DELSIM35
Bhabha generator and sample size	BABAMC: 4098 barrel events
Dimuon generator and sample size	DYMU3: 8639 events
Ditau generator and sample size	KORALZ: 8998 events
Selection cuts:	$\dagger_{A1}$,$\dagger_{A2}$,$\dagger_{A9}$ and no MUB hits associated with either of the highest momenta tracks
Simulated Bhabha:dimuon:ditau ratio	0.698 : 0.017 : 0.285

the real situation does not matter. This would imply that the simulation *may* be sufficiently accurate for the purpose of estimating the ratio of ditaus and Bhabhas passing the selection cuts. Any resulting error from relying on the simulation is, however, difficult to compute from this diagram as the condition for passing the Bhabha cut is $>$ 10GeV on one track and $>$ 25GeV on the other. The reconstructed energies may be coupled since the tracks are back-to-back and may simultaneously enter inefficient regions of the (symmetric) HPC. One solution is to use a wide variety of cuts on the HPC energies up to 25GeV and to see whether the simulation estimate of the real signal and background levels always gives the same number of reconstructed electrons. The results for this study are shown in Table 4.13.

Table 4.13: The reconstructed number of Bhabha events by the DELPHI simulation for a variety of HPC energy cuts on the 1989 data, over the angular region for which the positron scattering angle lies in the range $50° \leq \theta \leq 130°$.

Cut combination on the two charged tracks	Number of real events selected	Estimated tau contamination	Reconstructed number of Bhabhas
0 + 20GeV	248	16.1%	244.7
0 + 25GeV	234	11.3%	244.0
5 + 10GeV	238	14.0%	251.6
5 + 15GeV	230	12.1%	249.3
5 + 20GeV	221	9.4%	246.1
5 + 25GeV	215	6.7%	246.8
10 + 10GeV	219	9.3%	244.5
10 + 15GeV	214	8.6%	245.1
10 + 20GeV	210	7.0%	244.7
10 + 25GeV	207	5.0%	246.5

Over this wide range of cut combinations and estimated background levels the number of reconstructed Bhabhas converges to (246.3 ± 2.3); therefore the simulation will be taken to accurately reproduce the energy distribution of the real data in the low energy region necessary for the calculation of the Bhabha/ditau ratio.

This study resolves the problem of the ditau background, but not the absolute identification efficiency; this can in fact be *measured* from the real data in the following way. A pure Bhabha sample is obtained without the HPC by demanding

a 20GeV/c momentum cut on both tracks, an acolinearity of less than 2° and no hits in the MUB associated with either track. The standard angular cuts $\dagger_{A1}$ and $\dagger_{A9}$ and the vertex cut are also applied. These cuts give 124 events in the barrel, 103 of which also pass the standard HPC Bhabha selection cut $\dagger_{A6}$. This gives the percentage passing the HPC cut to be $(83.1 \pm 3.4)\%$. The simulation predicts the initial sample to be 96.0% Bhabhas, while the final sample is 99.7% Bhabhas. Therefore the measured HPC Bhabha identification efficiency, correcting for the larger background in the initial sample, is $(86.3 \pm 3.5)\%$. This compares to a simulated efficiency of $(94.0 \pm 0.4)\%$ within the measurement region. Therefore a factor of (1.089 ± 0.044) needs to be added to correct for the discrepancy between the simulation and real data over the 1989 running period.

4.18 T-Channel Correction in Bhabha Scattering

Bhabha events are more complex than dimuon events because the resulting particles are indistinguishable from the original ones and in calculating the cross-section there are a greater number of amplitudes to be taken into account; there are electron scattering (t-channel) as well as the annihilation graphs (s-channel). The ALIBABA program [21], briefly discussed in Chapter 1, is used here to predict the ratio of the cross-sections of an s and t-channel sample for both outgoing particles within the $50° \leq \theta \leq 130°$ region i.e the physical sample, to a computed s-channel only cross-section over 4π. This can then be multiplied as a correction factor to the real Bhabha sample which can later be compared directly to the other leptonic samples which are pure s-channel.

Five plots are shown in Figs. 4.19 and 4.20; these show the s and t channel cross-section predictions over some selected angle and energy ranges. An earlier program developed by M.Greco [40] has been used to obtain them for reasons of processing speed. The Greco model does not include all the radiative corrections of the ALIBABA program used for the analysis, but it is fast enough and accurate enough to be able to show the general characteristics.

The first plot shows the differential cross-section over $d\sigma/d\theta$, integrated over ϕ, of the Bhabha scattering with and without the t-channel contribution. The

Figure 4.19: The differential cross-section variation with θ for s-channel and combined s and t-channel Bhabha scattering in the Greco model.

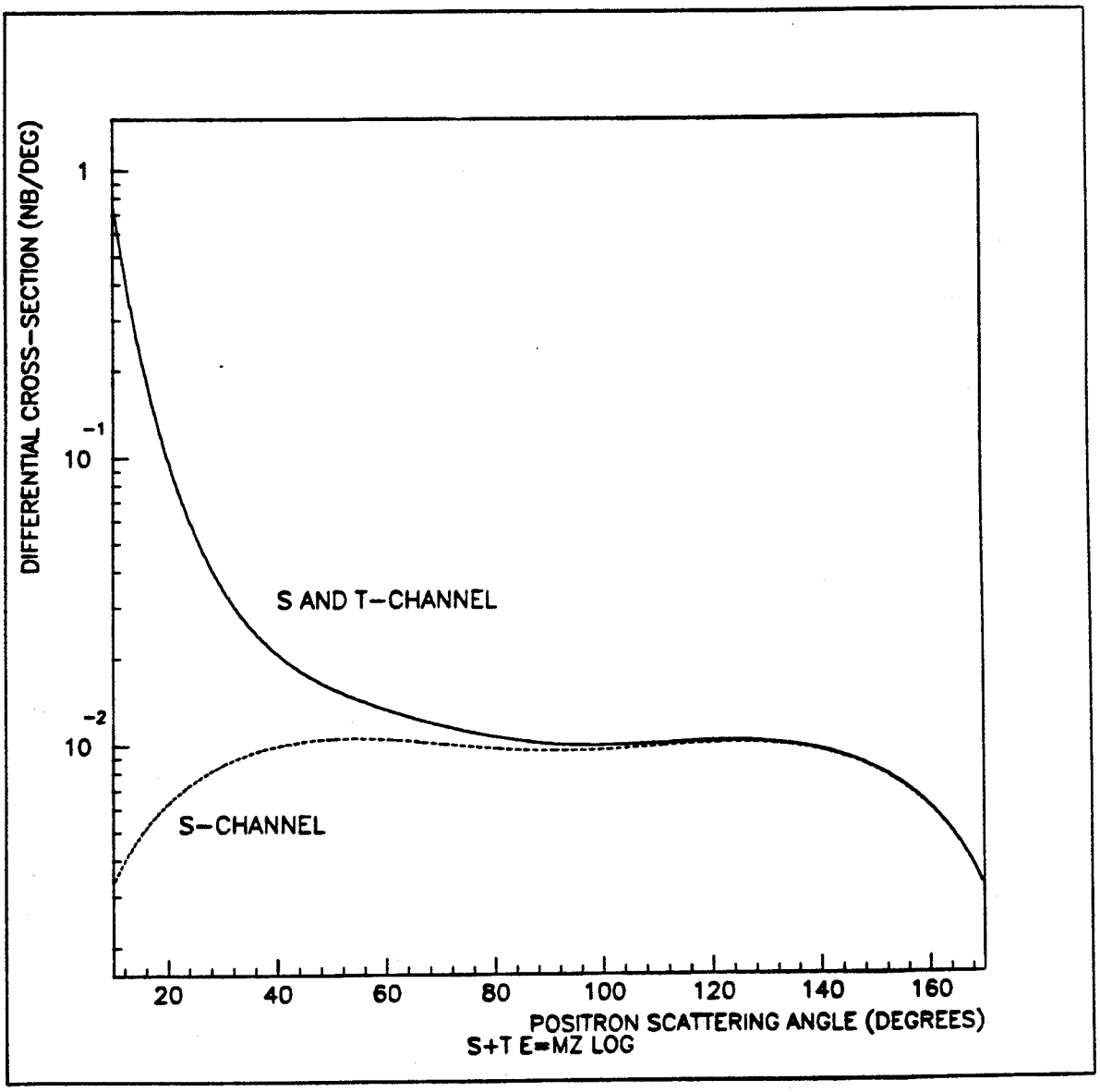

Analysis Conditions	
M_Z (Z° mass)	91.171
Γ_Z (Z° width)	2.511
$\sin^2(\theta_W)$	0.227

second figure shows four plots of the variation of the total cross-section with energy with and without the t-channel contribution for two angular regions: $50^\circ - 130^\circ$ and $90^\circ - 130^\circ$. The lower two plots indicate the ratio of the s-channel and total cross-sections for each of the two cases. An interesting feature

Figure 4.20: The variation with energy of the total cross-section integrated over selected angular ranges for s-channel and combined s and t-channel Bhabha scattering in the Greco model. The lower two plots show the ratios of the two distributions.

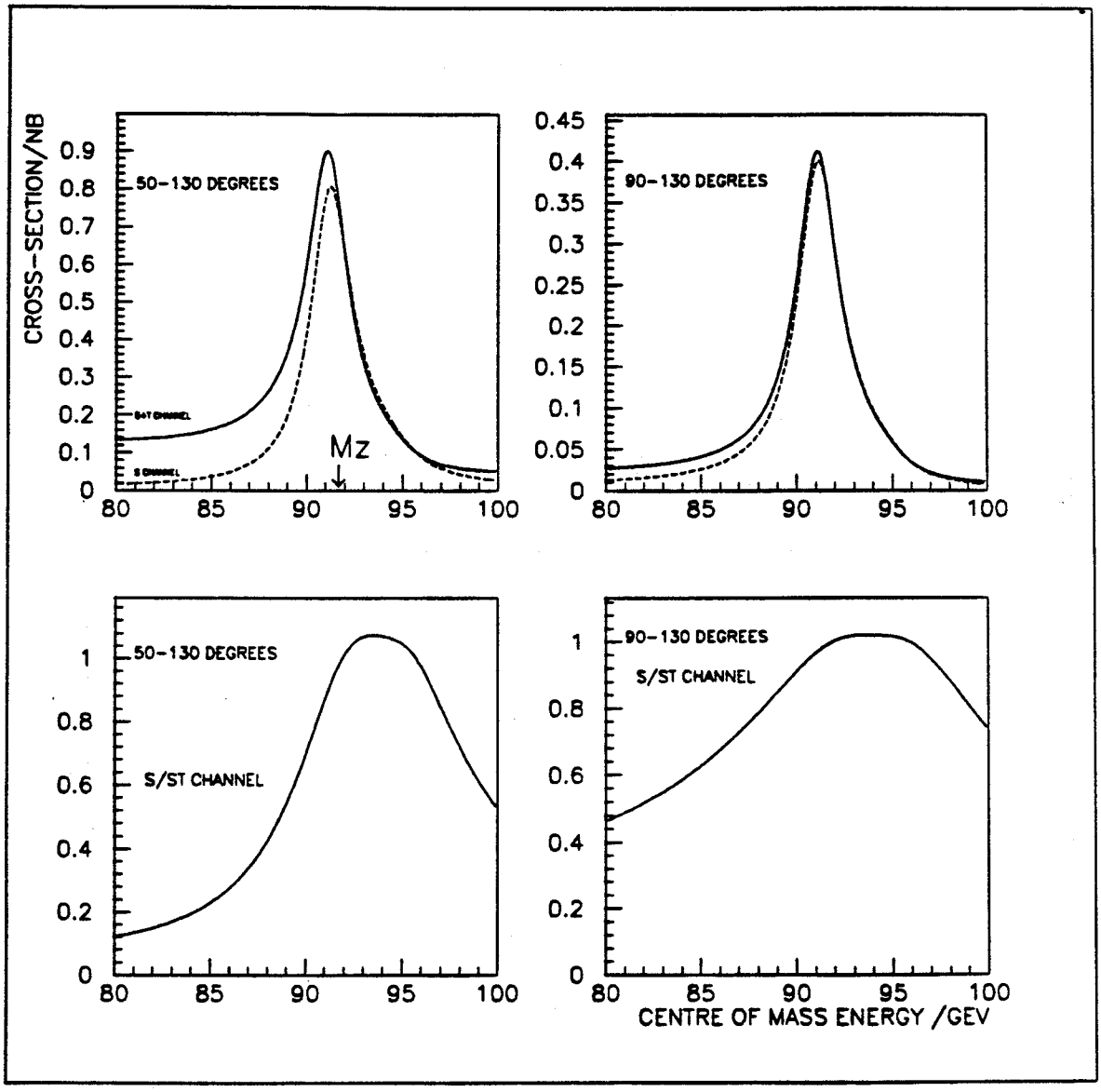

Analysis Conditions	
M_Z (Z° mass)	91.171
Γ_Z (Z° width)	2.511
$\sin^2(\theta_W)$	0.227

is that the t-channel contribution is very peaked in the forward direction; in fact it becomes infinite in the limit $\theta \rightarrow 0$ as expected as there is then an unscattered electron beam.

In Table 4.14 below the ALIBABA scaling factor to obtain the s-channel contribution over the barrel region and over the whole angular region is listed for each centre-of-mass energy in the analysis.

Table 4.14: ALIBABA computed scaling factors for obtaining the s-channel cross-section from the total cross-section in the barrel region and over the whole angular region.

C.M. Energy	$\frac{\sigma_S(50°-130°)}{\sigma_{ST}(50°-130°)}$	$\frac{\sigma_S(0°-180°)}{\sigma_{ST}(50°-130°)}$
88.28	0.435	0.803
89.28	0.562	1.033
90.28	0.725	1.328
91.04	0.856	1.566
91.28	0.895	1.637
91.54	0.930	1.702
92.28	0.999	1.834
93.28	1.018	1.879
94.28	0.982	1.829
95.04	0.939	1.760

When the correction factors are weighted for the numbers of electrons detected at each energy in Table 4.10, the mean correction factor for obtaining the number of s-channel Bhabhas over 4π is 1.567.

The theoretical ALIBABA error on this figure is 0.7% and there is an additional 0.5% error due to the uncertainty on the c.m. energy which can vary by $\pm$30MeV; the overall systematic uncertainty due to this correction factor is therefore 0.9%.

4.19 Reconstructed Event Numbers

It is now possible to estimate the real number of Bhabha and dimuon events in the data, using the results from the simulation studies and adding additional corrections where necessary. Table 4.15 shows the number of events in each simulated sample passing the different selection procedures.

The simulated Bhabha sample size given in the Table is the number of simulated events generated with both outgoing particles within the angular range 50° and 130°. From the results of Section 4.18 this number needs an additional correction of (1.567$\pm$0.014) to obtain the equivalent number of s-channel Bhabhas

Table 4.15: The number of simulated events passing the final Bhabha and dimuon selection cuts.

Event type	Sample size	$\dagger_\mu$	$\dagger_e$
e^+e^-	3846	0	2957
$\mu^+\mu^-$	8639	4093	0
$\tau^+\tau^-$	8998	122	183

generated over 4π. From these results the level of ditau contamination passing the Bhabha and dimuon cuts is $(4.1 \pm 0.3)\%$ and $(2.8 \pm 0.2)\%$ respectively, assuming an approximate lepton universality. The errors are computed assuming that the fraction of events passing a set of cuts follows a binomial distribution.

The correction factor for obtaining the real number of dimuons over 4π can be obtained from the formula

$$F_\mu = [(P_\mu/G_\mu) + (P_\tau/G_\tau)]^{-1}, \tag{4.18}$$

where G_μ and G_τ are the numbers of generated dimuons and ditaus in the simulated samples, and P_μ and P_τ are the numbers that pass the $\dagger_\mu$ cuts. A similar formula can be used to compute F_e for Bhabhas. F_μ is found to be (2.052 ± 0.023) and F_e is found to be (1.957 ± 0.023) with approximately half this error from simulation statistics and half from the s-channel correction factor.

These factors must then be combined with the correction factors for the trigger and particle identification efficiencies which are not modelled in the simulation. A summary of all the correction factors is shown in Table 4.16.

There are (204 ± 14) events that pass the $\dagger_\mu$ selection cut. This sample is contaminated with (4.0 ± 0.4) cosmic events, which leaves (200 ± 14). The total number of reconstructed dimuon events is therefore $(200 \pm 14(\text{stat.})) \times (2.217 \pm 0.064(\text{syst.}))$ which gives $(443 \pm 29(\text{stat.}) \pm 13(\text{syst.}))$. The total number of reconstructed s-channel Bhabha events is $(207 \pm 14(\text{stat.})) \times (2.135 \pm 0.090(\text{syst.}))$ which gives $(442 \pm 30(\text{stat.}) \pm 19(\text{syst.}))$.

4.20 The Hadronic Event Analysis

The selection criteria for hadronic events, and the efficiencies and backgrounds for the resulting sample used in this analysis were determined by the DELPHI

Table 4.16: The computed correction factors to the dimuon and Bhabha samples to reconstruct the (s-channel) generated numbers over 4π.

Correction to the $\dagger_e$ sample	Correction factor
F_e (simulated efficiency and ditau background subtraction within barrel)	1.957 ± 0.023
Bhabha identification efficiency correction	1.089 ± 0.044
Trigger efficiency correction	1.002 ± 0.002
Total	2.135 ± 0.090
Correction to the $\dagger_\mu$ sample	Correction factor
F_μ (simulated efficiency and ditau background subtraction)	2.052 ± 0.023
Dimuon identification efficiency correction	1.048 ± 0.018
Trigger efficiency correction	1.031 ± 0.021
Total	2.217 ± 0.064

analysis team IV. The published paper based on this data is ref. [41]. The selection criteria for charged particles were as follows:

- a polar angle θ between 20° and 160°;
- a momentum between 0.1GeV/c and 50GeV/c;
- a track length > 30cm;
- a relative error on the momentum measurement below 100%;
- a projection of the impact parameter in the xy plane below 4cm;
- a z coordinate at the origin below 10cm.

Clusters of HPC energies in the energy range $0.1 < E < 50$GeV where not associated to charged tracks were assumed to be from neutral particles.

Hadronic events were accepted if the total charged multiplicity was at least 5 and if either the invariant mass of all charged particles was larger than 12GeV, or the total energy (including the HPC clusters) was greater than 16GeV. The $\tau^+\tau^-$ background to this sample was determined to be $(0.3 \pm 0.1)\%$ using the KORALZ event generator. The cut on the invariant mass of the charged particles removed the remaining contributions from beam gas and two photon interactions.

A detailed Monte Carlo simulation of hadronic events in DELPHI was performed using DELSIM, the MUSTRAAL event generator [42] and the Lund parton shower fragmentation model [29]. The simulation described well the distribution of various topological variables of the hadronic data in DELPHI when the same analysis was applied to the real and simulated data, although track losses in the forward region ($|cos(\theta)| > 0.65$) were greater than expected in the real data, and an additional correction to the final number of events was required. The final estimated efficiency of this analysis method was $(92.1 \pm 1.1)\%$.

The numbers of hadronic events selected at each energy, using the same runs as for the leptonic analysis, are shown in Table 4.17.

Table 4.17: The number of hadronic events at each energy in the 1989 data.

Collision Energy (GeV)	Number of Hadronic Events
88.28	199
89.28	240
90.28	747
91.04	1201
91.28	1791
91.54	2668
92.28	579
93.28	548
94.28	90
95.04	90
TOTAL	**8153**

The total number estimated number of hadronic events for the selected runs is therefore $(8852 \pm 98(\text{stat.}) \pm 106(\text{syst.}))$.

4.21 Calculation of Hadron/Charged Lepton Event Ratios

The final estimates for the total number of dimuons, s-channel Bhabhas and hadronic events within DELPHI for the chosen 1989 runs are shown in Table 4.18.

This gives a final answer for the ratios of the event numbers:

$$N_{had}/N_{ee} = (20.0 \pm 1.4(\text{stat.}) \pm 0.9(\text{syst.}))$$

Table 4.18: The reconstructed number of s-channel Bhabhas, dimuons and hadronic events for the selected runs of the 1989 DELPHI data.

Event type	Total number	Statistical error	Systematic error
Bhabha	442	30	19
Dimuon	443	29	13
Hadronic	8852	98	106

$$N_{had}/N_{\mu\mu} = (20.0 \pm 1.3(\text{stat.}) \pm 0.6(\text{syst.})). \tag{4.19}$$

The ratio of dimuon to ditau events has also been computed to be:

$$N_{\tau\tau}/N_{\mu\mu} = (0.85 \pm 0.14(\text{stat.})). \tag{4.20}$$

4.22 Calculation of Partial Width Ratios

In the preceding section the ratios of hadronic to leptonic events were calculated for this event sample. However to obtain from this the partial width ratios of the Z° decays to the hadronic channel and these leptonic channels the contribution of the photon exchange term and the Z°/photon interference term must be subtracted off. These will bias the results as the ratio of these decay products in photon exchange is different, as shown in Chapter 1. The correction factors can be estimated using the ZBATCH [13] and ZHADRO [13] programs and are given in Table 4.19 for each c.m. energy. The Z° mass value is one of the input parameters and is here the value of ref. [41] determined from the DELPHI hadronic data taken during 1989. The average correction value, weighted for the number of hadronic events at each energy, is 1.016. The estimated theoretical error is less than 0.5%. After applying this correction there is a final measurement of the values of Γ_{had}/Γ_{ee} and $\Gamma_{had}/\Gamma_{\mu\mu}$ of

$$\begin{aligned} \Gamma_{had}/\Gamma_{ee} &= (20.3 \pm 1.4(\text{stat.}) \pm 0.9(\text{syst.})) \\ \Gamma_{had}/\Gamma_{\mu\mu} &= (20.3 \pm 1.3(\text{stat.}) \pm 0.6(\text{syst.})). \end{aligned} \tag{4.21}$$

The partial width ratio of dimuon and ditau events remains the same;

$$\Gamma_{\tau\tau}/\Gamma_{\mu\mu} = (0.85 \pm 0.14(\text{stat.})). \tag{4.22}$$

Table 4.19: The photonic exchange correction factors to the Z° partial width ratio Γ_{had}/Γ_{ll} for each c.m. energy in the 1989 data assuming $\alpha_s = 0.12$,$m_H = 100$GeV,$m_t = 130$GeV and $M_Z = 91.171$GeV. The calculation uses the ZBATCH and ZHADRO programs of ref. [13].

C.M. Energy/GeV	Photonic Correction Factor
88.28	1.081
89.28	1.042
90.28	1.019
91.04	1.012
91.28	1.011
91.54	1.011
92.28	1.015
93.28	1.026
94.28	1.040
95.04	1.051

4.23 Error Summary

The various contributions to the final error on $\Gamma_{had}/\Gamma_{\mu\mu}$ and Γ_{had}/Γ_{ee} are shown in Fig. 4.21, making the assumption that all the errors can be added in quadrature. It can be seen from this breakdown of the errors that the low statistics at this stage of data taking are the primary limit on the resolution of the experiment. The second largest source of error on the dimuon sample is the trigger efficiency, followed by the muon identification efficiency; both these are measured from the data and so are in fact also constrained by statistics. The second largest error on the Bhabha sample is the Bhabha identification uncertainty with the HPC - this large uncertainty also being due to low statistics. The largest totally non-statistical error is the theoretical t-channel subtraction for the Bhabha sample at 0.9%.

Figure 4.21: The relative sizes of the separate contributions to the errors on $\Gamma_{had}/\Gamma_{\mu\mu}$ and Γ_{had}/Γ_{ee}. Pie chart (a) shows the breakdown of the $\Gamma_{had}/\Gamma_{\mu\mu}$ error. Pie chart (b) shows the same for Γ_{had}/Γ_{ee}. The relative sizes of the pie charts indicates the relative sizes of the total computed errors.

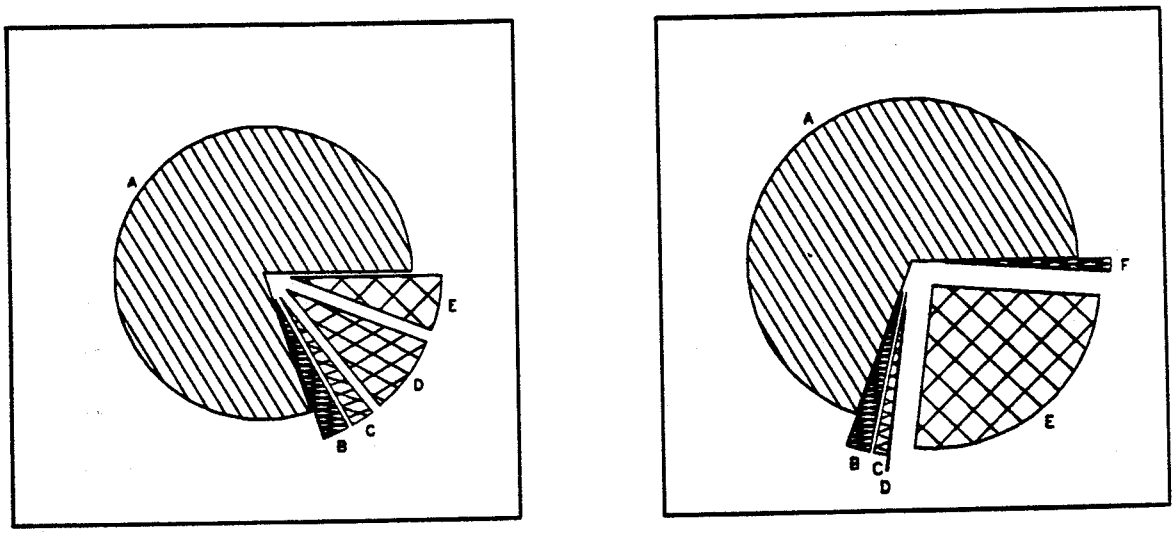

Plot(a)		Plot(b)	
A	Total statistical error	A	Total statistical error
B	Systematic hadronic error	B	Systematic hadronic error
C	Simulation statistics	C	Simulation statistics
D	Trigger efficiency uncertainty	D	Trigger efficiency uncertainty
E	Dimuon identification uncertainty	E	Bhabha identification uncertainty
		F	t-channel subtraction

Chapter 5

Leptonic Analysis of the 1990 Data

Preamble

Chapter 5 presents a study of the data collected during the 1990 running up until 14/7/1990 (run 13620); these data are taken at 7 c.m. energies from 88.22 to 94.22 GeV with $\sim$ 72% collected at 91.22GeV near the peak of the resonance. The same selection cuts are used as for the 1989 data analysis of Chapter 4; the efficiency parameters are, however, re-computed to take into account changes in the detector performance. The ratios Γ_{had}/Γ_{ee} and $\Gamma_{had}/\Gamma_{\mu\mu}$ are found to be $(21.96 \pm 0.65(\text{stat.}) \pm 0.49(\text{syst.}))$ and $(21.06 \pm 0.66(\text{stat.}) \pm 0.37(\text{syst.}))$ respectively from this data sample. In addition the ratio $\Gamma_{\tau\tau}/\Gamma_{\mu\mu}$ is estimated to be $(1.02 \pm 0.06(\text{stat.}))$.

5.1 Dimuon Data Analysis

The efficiency of the dimuon trigger varied from $(92.0 \pm 1.3 \pm 0.6)\%$ at the start of data taking to $(99.8 \pm 0.1 \pm 0.1)\%$ by mid-July. The variation was due to problems with the OD trigger system during the early stage of running. The mean value over the running period was $(97.0 \pm 0.5 \pm 0.2)\%$. The dimuon events are selected using the same analysis cuts as determined in Chapter 4. However it is now possible to examine the effect of certain selection cuts used in the analysis with more precision now that greater statistics are available than in 1989. Fig. 5.1 compares the inverse momentum distributions of the 1990 and simulation data for a sample of data predicted to consist of $\sim$ 92% dimuons after all the dimuon selection cuts except the momentum cut have been applied. For this plot a tighter vertex cut of $r < 0.4$cm and $(-2.15 < z < +1.85)$cm has also been applied to reduce the cosmic background by a factor of 4 as this would otherwise distort the real data spectrum when compared to the simulation.

The distributions show that the resolution of the dimuon peak itself is considerably better than for the 1989 data, shown in Section 4.11. The low momentum tail of the distribution (mainly ditaus) appears well modelled by

Figure 5.1: Normalized inverse momentum distributions for a ~ 92% dimuon sample. Distributions for the 1990 data (full line) and simulation data (broken line) over the range (0 to 0.190)GeV^{-1} are shown in plot(b). In plot(a) the difference between the real and simulation data is plotted over the range (0.027 to 0.178)GeV^{-1} with statistical error bars added to the data points. This range of inverse momenta contains possible momentum selection cuts which are marked on the plot.

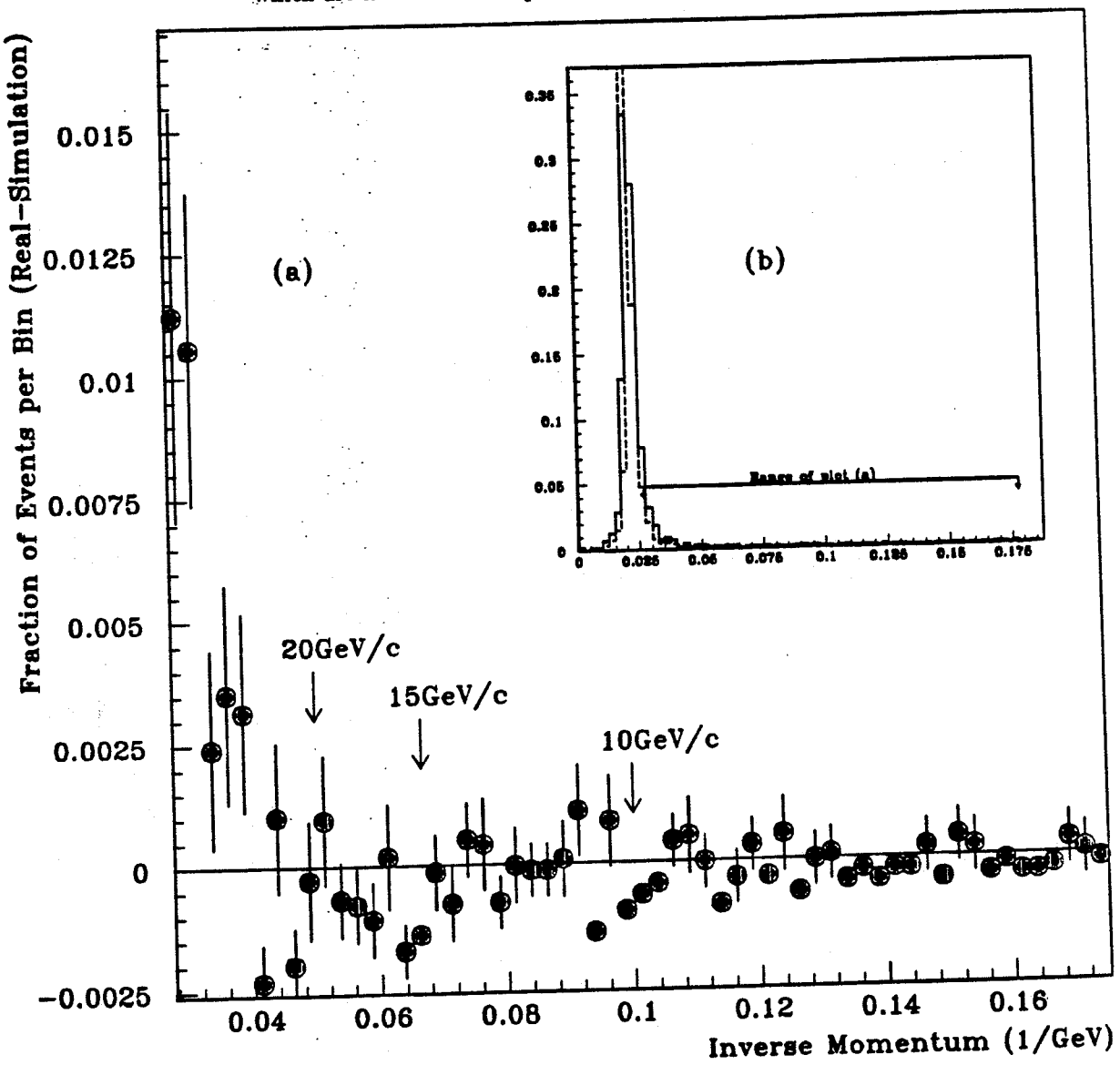

Analysis Conditions	
Real data sample	Runs 7912 - 13620
Analysis package	DELANA33,GEDTAN
Selection cuts	t_{A1},t_{A2},t_{A3}, t_{B7},t_{A8},t_{A10} and a tight vertex cut (see text)
Detector simulation	DELSIM35
Dimuon generator and sample size	DYMU3: 8639 events
Ditau generator and sample size	KORALZ: 8998 events
Simulated dimuon:ditau ratio	0.923 : 0.077

the simulation up to $\sim$ 20GeV/c but fails above that. The physical reason for the improved momentum resolution at high momenta is that better alignment and calibration constants, particularly for the TPC, enable more accurate measurements of the track curvatures to be made. All these data are also taken under full magnetic field conditions, unlike the 1989 data for which there was a consequent degradation of performance during part of the data taking.

The comparison of the real and simulation data indicates that the 1989 momentum cut of 15GeV/c is suitable for use - bearing in mind the need to predict with the simulation the level of background and loss of signal in the dimuon sample due to this cut.

The cosmic background to the dimuon sample needs to be recomputed for the 1990 data; as before the number of tracks are determined that satisfy the dimuon selection outside the $r < 0.8$cm and $(-4.3 < z < +3.7)$cm vertex cut, and within the cuts $|z| < 10.0$cm and $r < 8.0$cm. The results for each c.m. energy in 1990 are shown in Table 5.1.

Table 5.1: Cosmic background to the dimuon sample in the 1990 data.

Energy	Cosmics outside the $\dagger_{A8}$ vertex cut	Estimated cosmic contamination within the $\dagger_{A8}$ vertex cut
88.22	35	1.46 $\pm$ 0.24
89.22	37	1.54 $\pm$ 0.25
90.22	116	4.83 $\pm$ 0.45
91.22	263	10.96 $\pm$ 0.68
92.22	41	1.71 $\pm$ 0.27
93.22	32	1.33 $\pm$ 0.23
94.22	49	2.04 $\pm$ 0.29
TOTAL	**573**	**23.90 $\pm$ 1.00**

The number of events passing the dimuon cut at each c.m. energy is shown in Table 5.2.

The dimuon identification efficiency can be determined using the procedure of Section 4.17.2; a nearly pure dimuon sample is created using momentum cuts of 20GeV/c on each track, an acolinearity of less than 2°, and a veto of 4GeV associated energy deposited in the HPC from either track. This gives 981 events, 967 of which pass the $\dagger_{B7}$ cut used in the dimuon selection - the estimated ditau

Table 5.2: Events passing the dimuon selection cuts at each centre of mass energy in the 1990 data.

Energy	$\dagger_\mu$
88.22	11
89.22	49
90.22	165
91.22	787
92.22	55
93.22	33
94.22	32
TOTAL	**1132**

background is about 1% for both samples. This gives an identification efficiency of (98.6 ± 0.4); the simulated efficiency is $(99.7 \pm 0.1)\%$ and therefore the correction factor required for this cut is (1.011 ± 0.004).

The list of required correction factors to the 1990 dimuon data sample is shown in Table 5.3.

Table 5.3: The computed correction factors to the dimuon sample in the 1990 data after cosmic subtraction for the purpose of obtaining an idealized dimuon sample over 4π solid angle.

Correction to 4π of the $\dagger_\mu$ sample	Correction factor
F_μ (simulated dimuon identification efficiency and ditau background subtraction included)	2.052 ± 0.023
Compensation for the difference in the dimuon identification efficiency between the real and simulation data	1.011 ± 0.004
Trigger efficiency correction	1.031 ± 0.006
Total	2.139 ± 0.028

There are $(1132 \pm 34(\text{stat.}))$ events that pass the $\dagger_\mu$ selection cut. This sample is contaminated with $(24 \pm 1(\text{stat.}))$ cosmic events, which leaves $(1108 \pm 34(\text{stat.}))$. The total number of dimuon events in a perfect event sample (4π coverage and 100% identification) is therefore $(1108 \pm 34(\text{stat.})) \times (2.139 \pm 0.028(\text{syst.}))$ which gives $(2370 \pm 73(\text{stat.}) \pm 31(\text{syst.}))$.

Table 5.4: Events passing the Bhabha selection cuts at each centre of mass energy in the 1990 data.

Energy	$\dagger_e$
88.22	24
89.22	75
90.22	173
91.22	791
92.22	42
93.22	33
94.22	31
TOTAL	**1169**

5.2 Bhabha Data Analysis

The trigger efficiency for Bhabhas was computed to be $(99.8 \pm 0.1)\%$ during the data taking. Using the same selection procedure as used for the 1989 data the number of Bhabha events obtained at each c.m. energy is shown in Table 5.4.

The energy spectrum in the HPC is shown in Fig. 5.2 for a data sample consisting of Bhabhas, dimuons and ditaus selected as in Section 4.17.3 using all the Bhabha selection cuts except the HPC energy cut, and then using MUB signals to veto dimuons and some ditaus. The predicted ratio of Bhabhas, dimuons and ditaus for the sample is 0.698 : 0.285 : 0.017. The difference between the real and simulation data is also plotted and it can be seen there is reasonable agreement up to 30GeV, up from about 25GeV in the 1989 data sample. However there is still degradation of the Bhabha peak in terms of absolute energy and spread when compared to the simulation; the major problem is in modelling the behaviour when particles pass through the gaps between HPC modules. However, as shown in Section 4.17.3 the simulation can provide an accurate measure of the level of ditau background in the 1989 data, which is dependent on the modelling of the low energy part of the spectrum, and will therefore be taken also to be accurate for the 1990 data where the correspondence has in fact improved.

An absolute efficiency must also be computed for the HPC Bhabha identification. The procedure of Section 4.17.3 can be followed again; a tight acolinearity cut of 2°, a 20GeV/c momentum cut on both high momenta tracks, no other tracks with $>$ 1GeV/c and no hits in the MUB. These, along with the angular

Figure 5.2: The spectrum of HPC energies of 1990 (solid line) and simulation data (dashed line) for a data sample of ~ 70% Bhabhas selected without the HPC. Plot(a) shows the original distributions. In plot(b) the difference between the real and simulation data up to 40GeV is plotted with statistical error bars added.

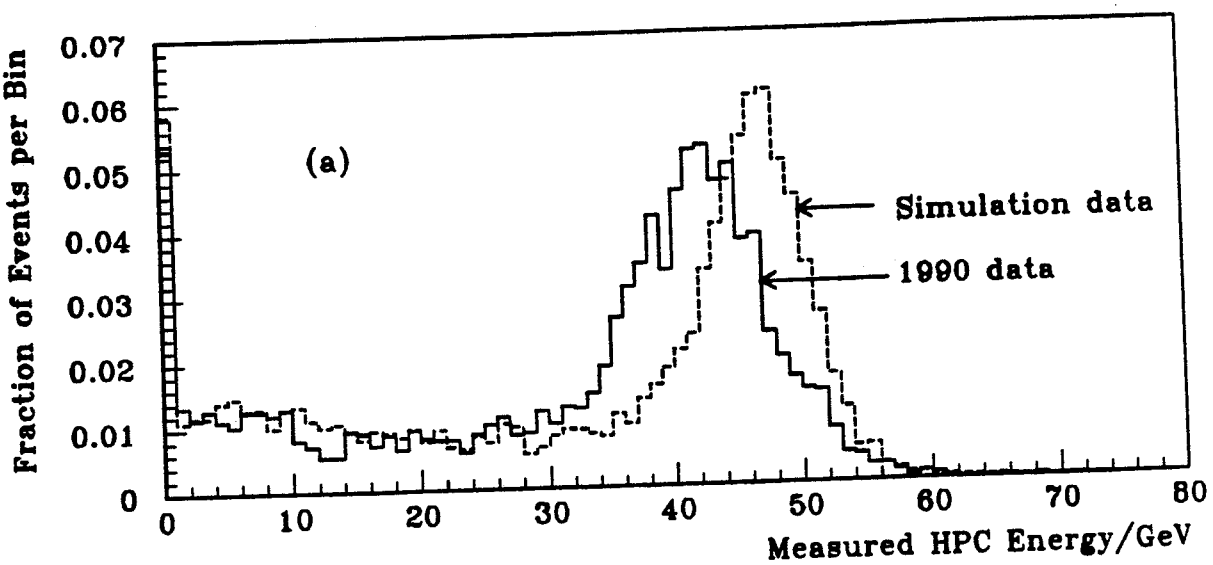

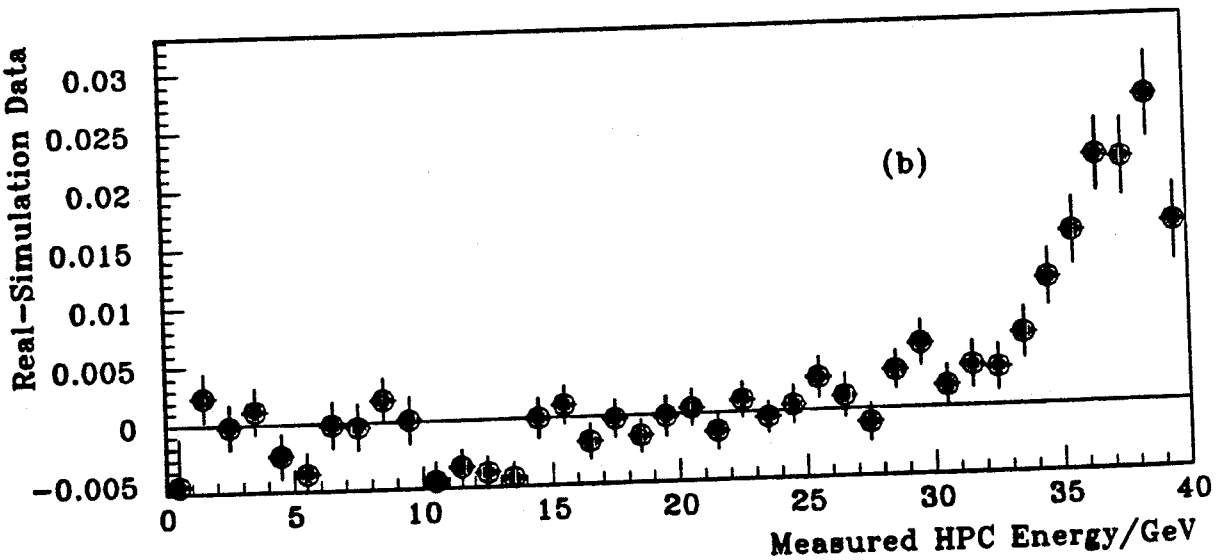

Analysis Conditions	
Real data sample	Runs 7912 - 13620
Analysis package	DELANA33,GEDTAN
Detector simulation	DELSIM35
Bhabha generator and sample size	BABAMC: 4098 barrel events
Dimuon generator and sample size	DYMU3: 8639 events
Ditau generator and sample size	KORALZ: 8998 events
Selection cuts	$\dagger_{A1}, \dagger_{A2}, \dagger_{A9}$ and no MUB hits associated with either of the highest momenta tracks
Simulated Bhabha:dimuon:ditau ratio	0.698 : 0.017 : 0.285

cuts, yield 806 events with a calculated 96.0% purity. Of this sample 723 pass the HPC selection cuts with an estimated 99.7% purity. This gives a measured efficiency of $(93.2 \pm 1.2)\%$, compared to a simulated efficiency of $(94.0 \pm 0.4)\%$. This shows again the convergence of the real and simulation data; only a small correction factor of $(1.009 \pm 0.014)\%$ needs to be included in the reconstructed number of Bhabhas.

The mean correction factor for t-channel subtraction in the barrel region and s-channel extrapolation to 4π is changed from the 1989 value because of the different distribution of events at each energy. The values of the correction factors calculated with ALIBABA (see ref. [21]) at each energy are displayed in Table 5.5. If these are weighted with the event distribution in Table 5.4 the mean

Table 5.5: ALIBABA computed scaling factors to obtain the s-channel cross-section over 4π from the total cross-section within $(50° \leq \theta \leq 130°)$ for the 1990 data points.

C.M. Energy	$\frac{\sigma_S(0°-180°)}{\sigma_{ST}(50°-130°)}$
88.22	0.791
89.22	1.016
90.22	1.308
91.22	1.620
92.22	1.826
93.22	1.880
94.22	1.834

correction factor is 1.538, with an estimated uncertainty of 0.9% as before for theoretical and energy uncertainties. This is the figure by which the number of simulated events within the barrel region must be modified to obtain the total number of s-channel Bhabhas simulated over 4π. The procedure of Section 4.19 is carried through as before to yield a correction factor F_e from simulation of (1.923 ± 0.023) for obtaining a 4π sample without t-channel or ditau contributions. This must be combined with the trigger efficiency and HPC Bhabha identification efficiency as summarized in Table 5.6. The total number of Bhabha events in a perfect event sample (s-channel, 4π coverage and 100% identification) is therefore $(1169 \pm 34(\text{stat.})) \times (1.944 \pm 0.036(\text{syst.}))$ which gives $(2273 \pm 66(\text{stat.}) \pm 42(\text{syst.}))$.

Table 5.6: The computed correction factors to the Bhabha sample for the 1990 data taking for obtaining an idealized s-channel sample over 4π solid angle.

Correction to the $\dagger_e$ sample	Correction factor
F_e (simulated Bhabha detection efficiency and ditau background subtraction included)	1.923 ± 0.023
Compensation for the difference in the Bhabha identification efficiency between the real and the simulation data	1.009 ± 0.014
Trigger efficiency correction	1.002 ± 0.001
Total	1.944 ± 0.036

5.3 Ditau Data Analysis

The same analysis is done here as for Chapter 4; the ratio of ditaus to dimuons is calculated, assuming that differences in the systematic corrections to each sample are negligible, apart from those computed in the simulations. The number of events passing the ditau selection cuts at each energy in the 1990 data is given in Table 5.7

Table 5.7: Events passing the ditau selection cuts at each centre of mass energy in the 1990 data.

Energy	Events found
88.22	6
89.22	20
90.22	62
91.22	311
92.22	23
93.22	17
94.22	11
TOTAL	**450**

Using the same method as used in Chapter 4, the number of real dimuons and ditaus may be estimated with Equation 5.1 where no initial assumption is made of the relative number of dimuons and ditaus;

$$\begin{pmatrix} \mu_R \\ \tau_R \end{pmatrix} = \begin{pmatrix} 2.121 & -0.176 \\ -0.390 & 6.129 \end{pmatrix} \begin{pmatrix} (1108 \pm 34(\text{stat.})) \\ (450 \pm 21(\text{stat.})) \end{pmatrix}, \qquad (5.1)$$

where $(1108 \pm 34(\text{stat.}))$ is the number of events passing the dimuon cuts, after cosmic subtraction, and $(450 \pm 21(\text{stat.}))$ is the number that pass the ditau selection cuts. The other numbers in the array are estimates computed from the simulation of the efficiencies of particle detection of each sample, and the mixing of these samples.

Therefore the computed real numbers of dimuons and ditaus over 4π are:

$$\mu_R = (2269 \pm 72(\text{stat.})); \tag{5.2}$$

$$\tau_R = (2317 \pm 130(\text{stat.})). \tag{5.3}$$

This gives

$$\tau_R/\mu_R = (1.02 \pm 0.06(\text{stat.})). \tag{5.4}$$

This result is compatible with lepton universality, which will be assumed to be exact when computing ditau backgrounds to the dimuon and Bhabha samples.

5.4 Hadronic Data Analysis

This analysis was done, as before, by the DELPHI analysis team IV. The trigger system was unchanged except for the following: an inclusion of a coincidence trigger between the TOF and the OD; a minimum requirement for the TOF trigger of two quadrants firing instead of three; a FEMC trigger threshold lowered from 4.0 to 3.5 GeV and a FEMC back-to-back trigger added as well as the single cluster trigger. The improved trigger efficiency is estimated to be $(99.5 \pm 0.2)\%$. The hadronic events are selected in the same way as in the 1989 sample; at least five charged tracks are required and a minimum charged energy of 14% of the c.m. energy. The overall efficiency is estimated to be $(92.7 \pm 1.1)\%$. The number of hadronic events detected at each energy during the runs used in the leptonic analysis are shown in Table 5.8.

The total number estimated number of hadronic events for the selected runs is therefore $(49330 \pm 230(\text{stat.}) \pm 590(\text{syst.}))$.

Table 5.8: The number of hadronic events at each energy in the 1990 data during runs selected for the leptonic analysis.

Collision Energy (GeV)	Number of Hadronic Events
88.22	587
89.22	1546
90.22	5482
91.22	33129
92.22	2277
93.22	1475
94.22	1230
TOTAL	**45726**

Table 5.9: The reconstructed number of s-channel Bhabhas, dimuons and hadronic events for the selected runs of the 1990 DELPHI data.

Event type	Total number	Statistical error	Systematic error
Bhabha	2273	66	42
Dimuon	2370	73	31
Hadronic	49330	230	590

5.5 Calculation of Partial Width Ratios

The final estimates for the total number of dimuons, s-channel Bhabhas and hadronic events within DELPHI for the chosen 1990 runs are shown in Table 5.9.

This gives a final answer for the ratios of the event numbers:

$$\begin{aligned} N_{had}/N_{ee} &= (21.70 \pm 0.64(\text{stat.}) \pm 0.48(\text{syst.})) \\ N_{had}/N_{\mu\mu} &= (20.81 \pm 0.65(\text{stat.}) \pm 0.37(\text{syst.})). \end{aligned} \tag{5.5}$$

The ratio of dimuon to ditau events has also been computed to be:

$$N_{\tau\tau}/N_{\mu\mu} = (1.02 \pm 0.06(\text{stat.})). \tag{5.6}$$

These results must now be corrected for the photon exchange contribution as in Chapter 4 to obtain the partial width ratios. Using the programs ZBATCH and ZHADRO [13] again the correction factor can be obtained for each c.m. energy. The average correction value, weighted for the number of hadronic events at each energy, is 1.012. The estimated theoretical error is less than 1%.

This gives a final answer for Γ_{had}/Γ_{ee} and $\Gamma_{had}/\Gamma_{\mu\mu}$ of

$$\Gamma_{had}/\Gamma_{ee} = (21.96 \pm 0.65(\text{stat.}) \pm 0.49(\text{syst.}))$$
$$\Gamma_{had}/\Gamma_{\mu\mu} = (21.06 \pm 0.66(\text{stat.}) \pm 0.37(\text{syst.})). \quad (5.7)$$

The partial width ratio of dimuon and ditau events remains the same;

$$\Gamma_{\tau\tau}/\Gamma_{\mu\mu} = (1.02 \pm 0.06(\text{stat.})). \quad (5.8)$$

5.6 Error Summary

The various contributions to the final errors on the partial width ratios that have been computed are shown in Fig. 5.3, making the assumption that all the errors can be added in quadrature.

Figure 5.3: The relative sizes of the separate contributions to the errors on the partial width ratios for the 1990 data sample. Pie chart (a) shows the breakdown of the $\Gamma_{had}/\Gamma_{\mu\mu}$ error. Pie chart (b) shows the same for Γ_{had}/Γ_{ee}.

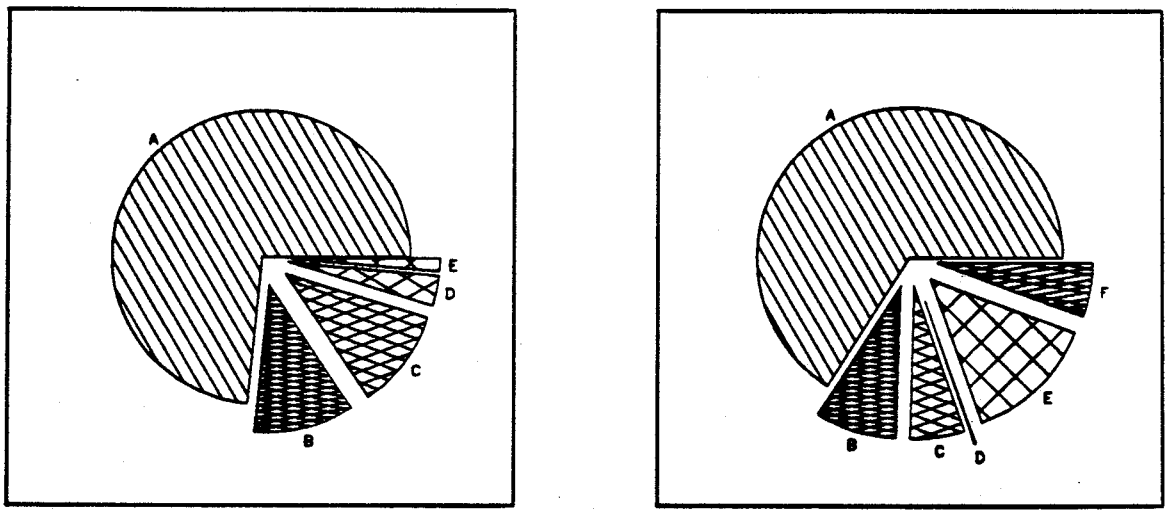

Plot(a)		Plot(b)	
A	Total statistical error	A	Total statistical error
B	Systematic hadronic error	B	Systematic hadronic error
C	Simulation statistics	C	Simulation statistics
D	Trigger efficiency uncertainty	D	Trigger efficiency uncertainty
E	Dimuon identification uncertainty	E	Bhabha identification uncertainty
		F	t-channel subtraction

It can be seen that statistical errors still dominate; the systematic hadronic error and simulation statistics form the next biggest contributions to the $\Gamma_{had}/\Gamma_{\mu\mu}$

error; the Bhabha identification efficiency forms the second biggest uncertainty in the Bhabha sample, although this measurement is also in fact dependent on statistics.

5.7 Partial Width Ratios in a Resonance Scan

The analysis up to this point has been concerned with obtaining an overall figure for the partial width ratio for the sum of the data at all the energy points of the scan. The numbers of events at each energy have only been used to obtain weighted correction factors such as the t-channel Bhabha correction. However there is a possibility that some energy variation of the partial width ratio may be present across the resonance that may be resolvable with the current level of statistics. One possibility is a third kind of exchange particle (apart from the Z° and photon) with a different coupling strength ratio to leptons and quarks and with a mass a few GeV different from M_Z. Here the analysis of the sections above is carried through from the 1989 and 1990 data combined, with separate correction factors for t-channel Bhabhas and photon exchange at each energy.

The analysis is carried through as before; the numbers of events at each energy are corrected for detector inefficiency and angular cuts, and backgrounds are subtracted off; the cosmic background to the dimuon sample, the ALIBABA (t-channel) corrections and the photonic exchange corrections are have different values for the data at each energy point.

The results are shown in graphical form in figs. 5.4 and 5.5. The error bars are the results of statistical and systematic errors added in quadrature and the dotted line indicates the theoretical value of 4.83% that is computed in Chapter 6. Plot 5.4(a) shows the ratio of Bhabha events in the barrel to the hadronic events over 4π solid angle. This ratio appears to vary over the scan; however this variation is due to the t-channel Bhabha contribution, the proportional size of which increases away from the resonance (see figs. 4.19 and 4.20). When the t-channel contribution is removed using the ALIBABA program, and the s-channel extrapolated to 4π the ratio appears energy independent (plot 5.4(b)). The (smaller) correction for photonic exchange away from the peak has also been included in this plot. If a linear expansion is made about the Z° mass value

Figure 5.4: Plots of (a) the ratio of Bhabha events in the barrel region and hadronic events over 4π and (b) the final measured partial width ratios of Z° decay to s-channel Bhabha and hadronic events, with the theoretical value (dotted line), over the energy points of a scan of the Z° resonance.

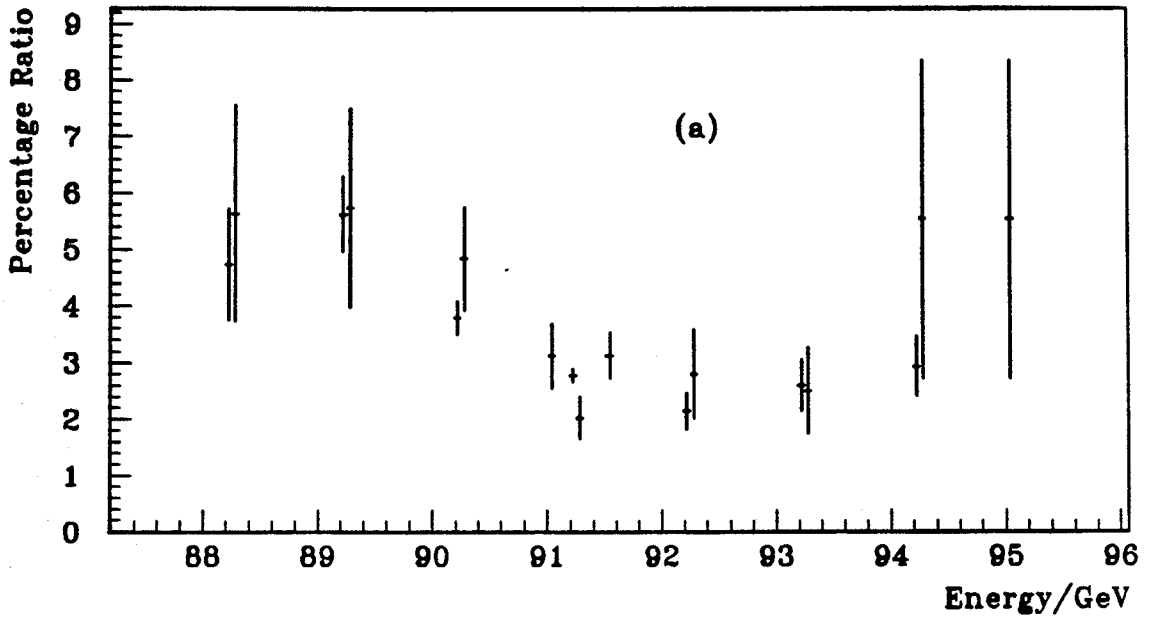

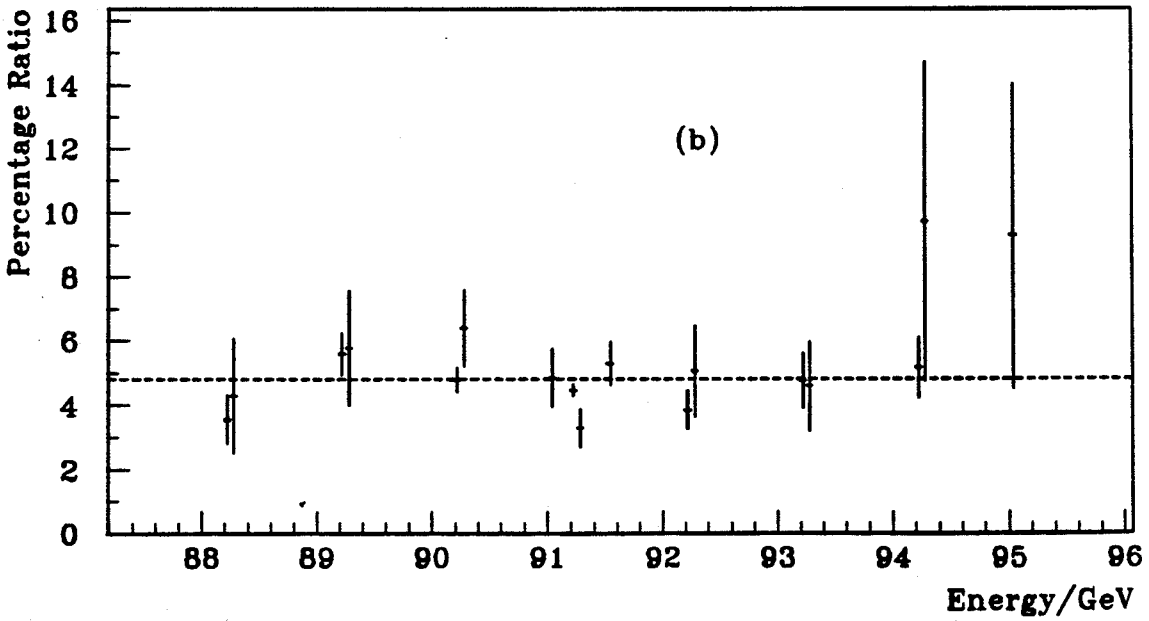

Data Samples	
1989 data sample	Runs 3302 - 6057
1990 data sample	Runs 7912 - 13620

The corrections have been made to the hadron and dimuon samples to obtain the idealized numbers i.e those of a 4π, 100% efficient detector with no background. The energy dependent cosmic, t-channel Bhabha and photon exchange contaminations have been separately subtracted for each energy.

Figure 5.5: A plot of the final measured partial width ratios of Z° decay to dimuon and hadronic events, with the theoretical value (dotted line), over the energy points of a scan of the Z° resonance.

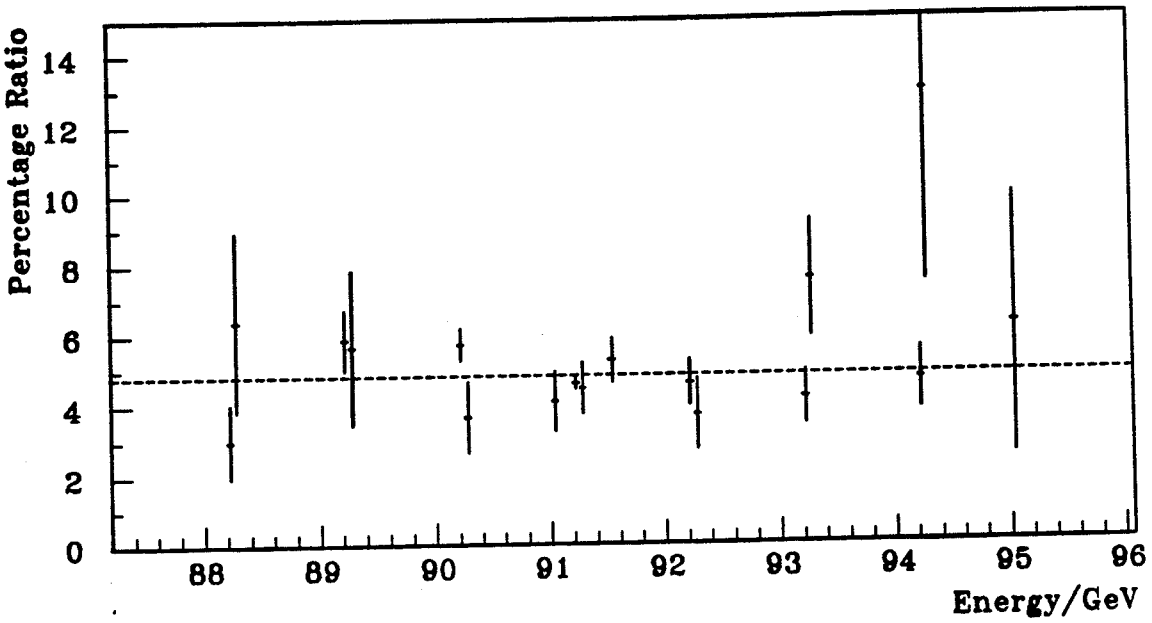

Data Samples	
1989 data sample	Runs 3302 - 6057
1990 data sample	Runs 7912 - 13620
The corrections have been made to the hadron and dimuon samples to obtain the idealized numbers i.e those of a 4π, 100% efficient detector with no background. The energy dependent cosmic and photon exchange contaminations have been separately subtracted for each energy.	

91.188GeV [43] taken from the DELPHI hadronic data, and if a parameter fit made using MINUIT [44], the slope of the variation across the resonance is found to be $(0.00 \pm 0.13)\text{GeV}^{-1}$ for the Bhabha data. A limit on the linear variation of the partial width ratio over $\pm$4GeV to either side of the M_Z value can be placed of $\pm$10% to one standard deviation.

Fig. 5.5 shows the partial width ratios to dimuon and hadronic events in a scan across the resonance; the cosmic and photon exchange contributions have been subtracted. As for the Bhabhas there is no indication of an energy dependent variation. A linear expansion about M_Z yields a slope of $(-0.06 \pm 0.15)\text{GeV}^{-1}$, which is again compatible with zero. Assuming the real value is in fact zero, the error on the fit value gives an estimate of the precision that can be obtained in this analysis. The variation is limited to within about $\pm$10% at one standard

deviation over ±4GeV on either side of M_Z. A confidence limit of 95% can be set that the variation is less than 20%.

A parabolic fit can also be done to both the Bhabha/hadronic and dimuon/hadronic partial width ratios over this energy range; again the fit values are within a single standard deviation of a flat distribution, and limit the possible variation with energy to within ±20% at the 95% confidence level for $|\sqrt{s} - M_Z| \leq 4\text{GeV}$.

Chapter 6

Comparison of Theoretical and Experimental Data

6.1 Recomputation of Theoretical Partial Width Ratios

As discussed in Chapter 1, the limit on the accuracy with which the theoretical partial width ratios may be determined within the Standard Model is set by the uncertainty of the value of $\alpha_s[M_Z{}^2]$. In Chapter 1 a value was determined of 20.85 ± 0.21 using a value of $\alpha_s[M_Z{}^2]$ of (0.126 ± 0.031) and the GAMMAZ program of G.Burgers [13].

The hadronic data from DELPHI can be used to provide a better estimate of $\alpha_s[M_Z{}^2]$ and hence of the theoretical partial width ratio. One of the analysis techniques with the smallest theoretical errors in determining this is the method of energy-energy correlations of hadronic events first introduced by Basham *et al.* [45]. These correlations are defined in practice by the histogram of the angle between all combinations of pairs of particles in hadronic events, weighted by the normalized energies, and averaged over all events;

$$EEC(\chi) = \frac{2}{\Delta\chi.N} \int_{\chi-\frac{\Delta\chi}{2}}^{\chi+\frac{\Delta\chi}{2}} \sum_{events}^{N} \sum_{i,j} \frac{E_i E_j}{E_{vis}{}^2} \delta(\chi' - \chi_{ij}) d\chi' \qquad (6.1)$$

where χ_{ij} is the angle between particles i and j and $\Delta\chi$ is the width of the histogram bin. Two-jet events yield a distribution sharply peaked near $\chi = 0°$ and $\chi = 180°$, whereas events with hard gluon radiation fill the central region in an asymmetric fashion. The shape of the distribution is therefore correlated with α_s. The energy-energy correlation asymmetry (ΔEEC) is defined as

$$\Delta EEC(\chi) = EEC(\pi - \chi) - EEC(\chi). \qquad (6.2)$$

$$\frac{\Gamma_{\tau\tau}}{\Gamma_{\mu\mu}} = 1.00 \pm 0.06(\text{stat.}) \tag{6.7}$$

These results are compatible with lepton universality; both are within one standard deviation of unity.

A limit can also be placed on a possible breakdown of lepton universality at this energy scale ($s \sim 8300\text{GeV}^2$). The result for the Bhabha/dimuon ratio has a precision of about ± 0.044 to one standard deviation if the statistical and systematic errors are added in quadrature. Assuming a Gaussian distribution on the total error a 95% confidence level prediction can be made that ($0.88 \leq \Gamma_{ee}/\Gamma_{\mu\mu} \leq 1.05$). At the same confidence level the ditau/dimuon ratio is limited to ($0.88 \leq \Gamma_{\tau\tau}/\Gamma_{\mu\mu} \leq 1.12$).

6.3.2 Partial Width Ratios

The differences between the theoretical prediction of Section 6.1 and the experimental partial width ratios of Section 6.2 are summarized below

$$\boxed{\begin{array}{l}\Gamma_{had}/\Gamma_{ee}(\text{expt.}) - \Gamma_{had}/\Gamma_{ee}(\text{theor.}) = 1.04 \pm 0.59(\text{stat.}) \pm 0.50(\text{syst.}) \\ \Gamma_{had}/\Gamma_{\mu\mu}(\text{expt.}) - \Gamma_{had}/\Gamma_{\mu\mu}(\text{theor.}) = 0.25 \pm 0.61(\text{stat.}) \pm 0.38(\text{syst.})\end{array}} \tag{6.8}$$

The value for $\Gamma_{had}/\Gamma_{ee}(\text{expt.})$ is therefore within 1.4σ of the theoretical prediction, and the value for $\Gamma_{had}/\Gamma_{\mu\mu}(\text{expt.})$ is within 0.4σ when the errors are combined in quadrature. According to the results of Section 5.7, there is also no evidence of a systematic change in the partial width ratios within ± 4GeV of the Z° mass value, and such a change is limited by the precision of that analysis to $\pm 20\%$ at the 95% confidence level.

6.4 Comparison with Other Experiments

Apart from the four LEP experiments ALEPH, DELPHI, L3 and OPAL the only other experiment currently in operation capable of measurements to comparable precision at the Z° resonance peak is the Mark II detector at the Stanford Linear Collider (SLC) in the United States; this accelerator has had considerable technical problems so the total sample of data available in this case is currently restricted to a few hundred Z° decays. Other experiments are handicapped by

the lower c.m. energy; for example the three TRISTAN experiments at the KEK centre in Japan (AMY, TOPAZ and VENUS) can only study e^+e^- events at a c.m. energy of up to 61.4GeV. At this energy the AMY experiment reports the hadron/charged lepton production ratio to be (4.54 ± 0.50) at 50GeV, rising to (5.38 ± 0.27) at 61.4GeV [49]. These are factors of (1.18 ± 0.13) and (1.40 ± 0.07) more than the equivalent values for QED and QCD effects only and so it is clear that at this energy range the effect of the resonance is significant. However the ability to monitor any deviation from the Standard Model prediction of the ratio value is limited; for example within two standard deviations the increase in the partial width ratio above the QED/QCD value measured by the AMY collaboration at 61.4GeV could lie between 26% and 54%. Therefore experiments that are operational at lower energies have not quoted measured values for the partial width ratio measurement although their data have been affected by the tail of the resonance and they have been able to show compatibility with the Standard Model predictions. A study of the combined results from PEP, PETRA and preliminary TRISTAN data is done in ref. [50] which shows the variation of the ratio of hadron to charged lepton production with energy up to 50GeV. However, these experiments have been able to search for violations of lepton universality at lower energies and none have been found. The most recent result is also from ref. [49] which quotes an average value of $R_{\tau\tau}/R_{\mu\mu}$ from data taken over the energy range 50GeV to 61.4GeV of (1.15 ± 0.06).

The results of the analysis of this thesis are presented in Table 6.2 together with the results of the ALEPH, OPAL, L3 and Mark II experiments for comparison. The data from the other LEP experiments are the latest available at the time of writing, and is taken either from the last published results or the most recent preprints where these are available [2]. It is clear that there is good agreement among all these measurements of the hadron/charged lepton partial width ratios and between these and the theoretical prediction. There are small differences in the precision of the measurements, as estimated by the detector groups themselves. However, these are primarily due to the different sizes of the data samples; for example the ALEPH result is based on a larger data sample of

[2] L3 hadron/charged lepton partial width ratio is a preliminary value quoted at the "Neutrino '90" conference.

References

[1] C.N. Yang and R.L. Mills, Phys. Rev. **95** p.631; **96** (1954) p.191.

[2] T. Kinoshita and W.B. Lindquist, Phys. Rev. Lett. **47** (1981) p.1573.

[3] P.B. Schwinberg, R.S. Van Dyck and H.G. Dehmelt, Phys. Rev. Lett. **47** (1981) p.1679.

[4] E. Fermi, Z. Phys. **88** (1934) p.161.

[5] R.P. Feynman and M. Gell-Mann, Phys. Rev. **109** (1958) p.193.

[6] C.S. Wu *et al.*, Phys. Rev. **105** (1957) p.1413.

[7] N. Cabibbo, Phys. Rev. Lett. **10** (1963) p.531.

[8] P.W. Higgs, Phys. Rev. **145** (1966) p.1156.

[9] S.L. Glashow, Nucl. Phys. **22** (1961) p.579
S. Weinberg, Phys. Rev. Lett. **19** (1967) p.1264
A. Salam, in "Elementary Particle Theory", ed. W. Svartholm Almquist & Wiksell Stockholm 1968.

[10] F.J. Hasert et al., Phys. Rev. Lett. **46B** (1973) p.121;
F.J. Hasert et al., Phys. Rev. Lett. **46B** (1973) p.138

[11] M.G. Bowler,"Femtophysics", Pergamon Press (1990).

[12] UA1 Collaboration, Phys. Lett. **B122** (1983) p.103; UA2 Collaboration, Phys. Lett. **B122** (1983) p.476.

[13] G. Burgers, CERN publication 88-06 Vol.1 p.121.

[14] S. Jadach and Z. Was, Comput. Phys. Commun. **36** (1985) p.191;
S. Jadach *et al.*, CERN report CERN 89-08, Vol. III (1989) p.67.

[15] J.E. Compagne and R. Zitoun, Z. Phys. **C43** (1989) p.469;
"Proc. Brighton Workshop on Radiative Corrections", Sussex July 1989.

[16] F.A. Berends, R. Kleiss and W. Hollik, DESY preprint DESY 87-094.

[17] "Z Physics at LEP", edited by G. Altarelli,R. Kleiss and C. Verzegnassi, CERN publication 89-08.

[18] W. Marciano, Brookhaven preprint BNL 36147.

[19] M. Kobayashi and T. Maskawa, Prog. Theor. Phys. **49** (1973) p.652.

[20] P.R. Renton, "Electroweak Interactions", Cambridge University Press (1990).

[21] W. Beenakker, F.A. Berends and S.C van der Marck, "Large Angle Bhabha Scattering", University of Leiden preprint (1990).

[22] M. Sands, "The Physics of Electron Storage Rings", SLAC-121 UC-28(AOC) Nov. 1970.

[23] "LEP Design Report", CERN-LEP/84-01.

[24] DELPHI collaboration, "The DELPHI Detector at LEP", CERN-PPE/90-128, submitted to Nuclear Instruments and Methods.

[25] DELPHI collaboration, "DELSIM Reference Manual", DELPHI Note 89-67 (1989), unpublished.

[26] J. Cuevas *et al.*, "FASTSIM Simulation for DELPHI", DELPHI Note 87-27 (1987), unpublished.

[27] DELPHI collaboration, "DELANA User's Guide", DELPHI Note 89-44 (1989), unpublished.

[28] R. Brun and J. Zoll, "ZEBRA - Data Structure Management System", CERN Program Library Q100.

[29] T. Sjostrand, Comput. Phys. Commun. **27** (1982) p.243; **28** (1983) p.229; T. Sjostrand and M. Bengtsson, Comput. Phys. Commun. **43** (1987) p.367.

[30] D. Bertrand, L. Pape, "TANAGRA User's Guide", DELPHI note 87-95 PROG 98 (1987), unpublished.

[31] F. Sauli, "Principles of Operation of Multiwire Proportional and Drift Chambers", CERN Publication 77-09.

[32] J. Townsend, "Electrons in gases", (Hutchinson, London 1947).

[33] T. Fearnley, M.Sc Thesis, University of Oxford (1987).

[34] U.S NIM Committee, "FASTBUS Modular High Speed Data Acquisition and Control System", U.S Department of Energy, Division of High Energy Physics, DOE/ER-0189.

[35] M.E.F. Veitch, D.Phil Thesis, University of Oxford (1989).

[36] N.C.E. Crosland, "Some Interim Results on Echoes", internal Oxford DELPHI Group report, unpublished.

[37] The DELPHI Collaboration, Phys.Lett **B241** (1990) p.425.

[38] R. Brun, O. Couet, C. Vandoni, P. Zanarini and M. Goosens, "PAW - Physics Analysis Workstation: Version 1.07", CERN Program Library Entry Q121.

[39] Particle Data Group, "Review of Particle Properties", Phys. Lett. **B204** (1988).

[40] M.Greco, Phys. Lett. **B177** (1986) p.97.

[41] The DELPHI Collaboration, Phys.Lett **B241** (1990) p.435.

C. Lambropoulos [v], J.W. Lamsa [κ], L. Lanceri [p], V. Lapin [u], J.-P. Laugier [c], R. Lauhakangas [e], P. Laurikainen [e], G. Leder [b], F. Ledroit [l], J. Lemonne [x], G. Lenzen [s], V. Lepeltier [o], A. Letessier-Selvon [m], E. Lieb [s], E. Lillestol [f], E. Lillethun [i], J. Lindgren [e], I. Lippi [θ], R. Llosa [g], M. Lokajicek [e], J.G. Loken [r], M.A. Lopez Aguera [n], A. Lopez-Fernandez [o], D. Loukas [v], J.J. Lozano [g], R. Lucock [d], B. Lund-Jensen [y], P. Lutz [l], L. Lyons [r], G. Maehlum [f], N. Magnussen [s], J. Maillard [l], A. Maltezos [v], F. Mandl [b], J. Marco [n], J.-C. Marin [f], A. Markou [v], L. Mathis [l], C. Matteuzzi [η], G. Matthiae [q], M. Mazzucato [θ], M.Mc Cubbin [y], R.Mc Kay [κ], E. Menichetti [z], C. Meroni [η], W.T. Meyer [κ], W.A. Mitaroff [b], G.V. Mitselmakher [e], U. Mjoernmark [h], T. Moa [g], R. Moeller [λ], K. Moenig [s], M.R. Monge [δ], P. Morettini [δ], H. Mueller [k], H. Muller [f], G. Myatt [r], F. Naraghi [m], U. Nau-Korzen [s], F.L. Navarria [α], P. Negri [η], B.S. Nielsen [λ], M. Nigro [θ], V. Nikolaenko [u], V. Obraztsov [u], R. Orava [e], A. Ostankov [u], A. Ouraou [c], R. Pain [m], H. Palka [κ], T. Papadopoulou [ξ], L. Pape [f], P. Pasini [α], A. Passeri [q], M. Pegoraro [θ], V. Perevozchikov [u], M. Pernicka [b], M. Pimenta [a], O. Pingot [x], C. Pinori [θ], A. Pinsent [r], M.E. Pol [a], G. Polok [κ], P. Poropat [p], P. Privitera [α], A. Pullia [η], J. Pyyhtia [e], A.A. Rademakers [β], D. Radojicic [r], S. Ragazzi [η], W.H. Range [y], P.N. Ratoff [r], A.L. Read [ζ], N.G. Redaelli [η], M. Regler [b], D. Reid [y], P.B. Renton [r], L.K. Resvanis [j], F. Richard [o], J. Ridky [e], G. Rinaudo [z], I. Roditi [f], A. Romero [z], P. Ronchese [θ], E.I. Rosenberg [κ], U. Rossi [α], E. Rosso [f], P. Roudeau [o], T. Rovelli [α], V. Ruhlmann [c], A. Ruiz [n], H. Saarikko [e], Y. Sacquin [c], E. Sanchez [g], J. Sanchez [g], E. Sanchis [g], M. Sannino [δ], M. Schaeffer [w], H. Schneider [k], F. Scuri [p], A. Sebastia [g], A.M. Segar [r], R. Sekulin [d], M. Sessa [p], G. Sette [δ], R. Seufert [k], R.C. Shellard [f], P. Siegrist [c], S. Simonetti [δ], F. Simonetto [θ], A.N. Sissakian [e], T.B. Skaali [ζ], J. Skeens [κ], G. Skjevling [ζ], N.E. Smirnov [u], G.R. Smith [d], R. Sosnowski [μ], K. Spang [λ], T. Spassoff [e], E. Spiriti [q], S. Squarcia [δ], H. Staeck [s], C. Stanescu [q], G. Stavropoulos [v], F. Stichelbaut [x], A. Stocchi [η], J. Strauss [b], R. Strub [w], C.J. Stubenrauch [f], M. Szczekowski [μ], M. Szeptycka [μ], P. Szymanski [μ], S. Tavernier [x], G. Theodosiou [v], A. Tilquin [l], J. Timmermans [β], V.G. Timofeev [e], L.G. Tkatchev [e], D.Z. Toet [β], A.K. Topphol [i], L. Tortora [q], D. Treille [f], U. Trevisan [δ], G. Tristram [l], C. Troncon [η], E.N. Tsyganov [e], M. Turala [κ], R. Turchetta [w], M.-L. Turluer [c], T. Tuuva [e], I.A. Tyapkin [e], M. Tyndel [d], S. Tzamarias [f], F. Udo [β], S. Ueberschaer [s], V.A. Uvarov [u], G. Valenti [α], E. Vallazza [z], J.A.Valls Ferrer [g], G.W. Van Apeldoorn [β], P. Van Dam [β], W.K. Van Doninck [x], N. Van Eijndhoven [f], C. Vander Velde [x], J. Varela [a], P. Vaz [a], G. Vegni [η], M.E. Veitch [r], J. Velasco [g], L. Ventura [θ], W. Venus [d], F. Verbeure [x], L.S. Vertogradov [e], L. Vibert [m], D. Vilanova [c], E.V. Vlasov [u], A.S. Vodopyanov [e], M. Vollmer [s], G. Voulgaris [j], M. Voutilainen [e], V. Vrba [e], H. Wahlen [s], C. Walck [g], F. Waldner [p], M. Wayne [κ], A. Wehr [s], P. Weilhammer [f], J. Werner [s], A.M. Wetherell [f], J.H. Wickens [x], J. Wikne [ζ], W.S.C. Williams [r], M. Winter [w], D. Wormald [ζ], G. Wormser [o], K. Woschnagg [y], N. Yamdagni [g], P. Yepes [β], A. Zaitsev [u], A. Zalewska [π], P. Zalewski [μ], P.I. Zarubin [e], E. Zevgolatakos [v], G. Zhang [s], N.I. Zimin [e], R. Zitoun [m], R.Zukanovich Funchal [l], G. Zumerle [θ] and J. Zuniga [g]

[a] *LIP, Av. Elias Garcia 14 - 1e, P-1000 Lisbon Codex, Portugal*
[b] *Institut für Hochenergiephysik, Österreichische Akademie der Wissenschaften, Nikolsdorfergasse 18, A-1050 Vienna, Austria*
[c] *DPhPE, CEN-Saclay, F-91191 Gif-Sur-Yvette Cedex, France*
[d] *Rutherford Appleton Laboratory, Chilton, Didcot OX11 0QX, UK*
[e] *Joint Institute for Nuclear Research, Dubna, Head Post Office, P.O. Box 79, SU-101 000 Moscow, USSR*
[f] *CERN, CH-1211 Geneva 23, Switzerland*
[g] *Instituto de Fisica Corpuscular (IFIC), Centro Mixto Universidad de Valencia-CSIC, Avda. Dr. Moliner 50, E-46100 Burjassot (Valencia), Spain*
[h] *Department of Physics, University of Lund, Sölvegatan 14, S-223 63 Lund, Sweden*
[i] *Department of Physics, University of Bergen, Allégaten 55, N-5007 Bergen, Norway*
[j] *Physics Laboratory, University of Athens, Solonos Street 104, GR-10680 Athens, Greece*
[k] *Institut für Experimentelle Kernphysik, Universität Karlsruhe, Postfach 6980, D-7500 Karlsruhe 1, FRG*
[l] *Institute of Physics, University of Stockholm, Vanadisvägen 9, S-113 46 Stockholm, Sweden*
[m] *LPNHE, Universités Paris VI et VII, Tour 33 (RdC), 4 place Jussieu, F-75230 Paris Cedex 05, France*
[n] *Facultad de Ciencias, Universidad de Santander, av. de los Castros, E-39005 Santander, Spain*
[o] *Laboratoire de l'Accélérateur Linéaire, Université de Paris-Sud, Bâtiment 200, F-91405 Orsay, France*
[p] *Dipartimento di Fisica, Università di Trieste and INFN, Via A. Valerio 2, I-34127 Trieste, Italy*

and Istituto di Fisica, Università di Udine, Via Larga 36, I-33100 Udine, Italy
[q] *Istituto Superiore di Sanità, Istituto Nazionale di Fisica Nucleare (INFN), Viale Regina Elena 299, I-00161 Rome, Italy*
and Dipartimento di Fisica, Università di Roma II and INFN, Tor Vergata, I-00173 Rome, Italy
[r] *Nuclear Physics Laboratory, University of Oxford, Keble Road, Oxford OX1 3RH, UK*
[s] *Fachbereich Physik, University of Wuppertal, Postfach 100 127, D-5600 Wuppertal 1, FRG*
[t] *Laboratoire de Physique Corpusculaire, Collège de France, 11 place M. Berthelot, F-75231 Paris Cedex 5, France*
[u] *Institute for High Energy Physics, Serpukhov, P.O. Box 35, SU-142 284 Protvino (Moscow Region), USSR*
[v] *Greek Atomic Energy Commission, Nuclear Research Centre Demokritos, P.O. Box 60228, GR-15310 Aghia Paraskevi, Greece*
[w] *Division des Hautes Energies, CRN–Groupe DELPHI, B.P. 20 CRO, F-67037 Strasbourg Cedex, France*
[x] *Physics Department, Universitaire Instelling Antwerpen, Universiteitsplein 1, B-2610 Wilrijk, Belgium*
and IIHE, ULB–VUB, Pleinlaan 2, B-1050 Brussels, Belgium
and Service de Physique des Particules Elémentaires, Faculté des Sciences, Université de l'Etat Mons, Av. Maistriau 19, B-7000 Mons, Belgium
[y] *Department of Physics, University of Liverpool, P.O. Box 147, Liverpool L69 3BX, UK*
[z] *Dipartimento di Fisica Sperimentale, Università di Torino and INFN, Via P. Giuria 1, I-10125 Turin, Italy*
[a] *Dipartimento di Fisica, Università di Bologna and INFN, Via Irnerio 46, I-40126 Bologna, Italy*
[β] *NIKHEF-H, Postbus 41882, NL-1009 DB Amsterdam, The Netherlands*
[γ] *Department of Radiation Sciences, University of Uppsala, P.O. Box 535, S-751 21 Uppsala, Sweden*
[δ] *Dipartimento di Fisica, Università di Genova and INFN, Via Dodecaneso 33, I-16146 Genoa, Italy*
[ε] *Department of High Energy Physics, University of Helsinki, Siltavuorenpenger 20 C, SF-00170 Helsinki 17, Finland*
[ζ] *Physics Department, University of Oslo, Blindern, N-1000 Oslo 3, Norway*
[η] *Dipartimento di Fisica, Università di Milano and INFN, Via Celoria 16, I-20133 Milan, Italy*
[θ] *Dipartimento di Fisica, Università di Padova and INFN, Via Marzolo 8, I-35131 Padua, Italy*
[κ] *Ames Laboratory and Department of Physics, Iowa State University, Ames IA 50011, USA*
[λ] *Niels Bohr Institute, Blegdamsvej 17, DK-2100 Copenhagen O, Denmark*
[μ] *Institute for Nuclear Studies, and University of Warsaw, Ul. Hoża 69, PL-00681 Warsaw, Poland*
[ξ] *Physics Department, National Technical University, Zografou Campus, GR-15773 Athens, Greece*
[π] *High Energy Physics Laboratory, Institute of Nuclear Physics, Ul. Kawiory 26 a, PL-30055 Cracow 30, Poland*

Appendix B
Future Developments

The experimental results of this thesis confirm the predictions of the Standard Model regarding the partial width ratio of the Z° to charged leptons and hadrons, and test lepton universality at an energy scale of $s \sim 8300(\mathrm{GeV})^2$. However, the precision of these measurements is limited to about 3% by statistics; to improve this is it clear that a larger data sample is required.

One priority is to increase the LEP luminosity which has been a factor of ~ 5 (2 - $3 \times 10^{30}\mathrm{cm}^{-2}\mathrm{s}^{-1}$) less than the design value throughout most of the 1989 and 1990 running. This is improving and in late August 1990 was approaching $5 \times 10^{30}\mathrm{cm}^{-2}\mathrm{s}^{-1}$. There are hopes that this improvement will continue.

This thesis is also based on data recorded only in the barrel of DELPHI, the angular region $50^\circ \leq \theta \leq 130^\circ$, because of problems with the forward detectors. However, the operation of these is now improved and the DELPHI analysis teams have begun to extend the analysis down to 22°; this is particularly valuable for measurements of the forward-backwards charge asymmetry in charged lepton production which arises from the interference term between photon and Z° exchange near the resonance. The larger angular region will also increase the statistical sizes of the lepton samples, although the systematic differences between the barrel and end-cap detector parameters will have to be well understood. One of the simplifying aspects of the analysis of this thesis is that the detectors are reasonably uniform over the angular region of active particle detection.

As the statistical errors are reduced the systematic errors will assume greater importance. Over its first year of operation the performance of DELPHI has improved considerably and many parameters are approaching their design values. These improvements are due to better alignment and calibration of the sub-detectors, as well as improved operational reliability. As the parameters improve they are also better understood and this means systematical uncertainties will

also decrease. As an example of this a study is shown in Fig. B.1 of the number of layers of MUB chambers hit in an event (summed both hemispheres) passing the dimuon selection cuts defined in Chapter 4. Data are shown from the 1989, 1990 and simulation samples. The simulated distribution is computed using a ratio of dimuons and ditaus of (0.974 : 0.026) which assumes lepton universality and a sample of dimuons increased by 2.0% from cosmic contamination. The real data sets, passing the same cuts, are plotted with statistical error bars on the same normalized plots. The plots show that there are generally a smaller number of layers with hits in the 1989 data than in the simulation data. The average number is 5.94 in the real data, and 6.68 in the simulation.

The 1990 data are seen to follow more closely the simulated distribution and the average number of layers hit has increased to become nearly the same as the simulation. This change reflects increasing operational stability and better understood calibration constants.

Another example of operational improvement is in the particle momentum resolution of DELPHI as discussed in Chapters 4 and 5.

The general outlook for the future is therefore optimistic. The statistics of the event samples are likely to improve, possibly by as much as a factor of 100 over the next two years of LEP operation; this would reduce the statistical error on the partial width ratio measurements by a factor of 10. In addition the full capabilities of the DELPHI experiment are beginning to be achieved and better understood. This will result in a reduction in the systematic uncertainties. A measurement of the charged lepton/hadron production ratio and tests of lepton universality at a 0.3% level of accuracy, which may reveal small discrepancies with the Standard Model predictions, may therefore be possible within two years.

Figure B.1: Numbers of layers of muon chambers hit in the 1989, 1990 and simulation dimuon data samples. The selection cuts are defined in the analysis chapters. The data are contaminated by $(2.8 \pm 0.2)\%$ ditaus and this is also modelled in the simulation. Plot(a) is a comparison of the 1989 and simulation data (broken line). Plot(b) shows the same for the 1990 data. The average number of layers hit is marked with an 'R' (real data) and 'S' (simulation data) on each plot.

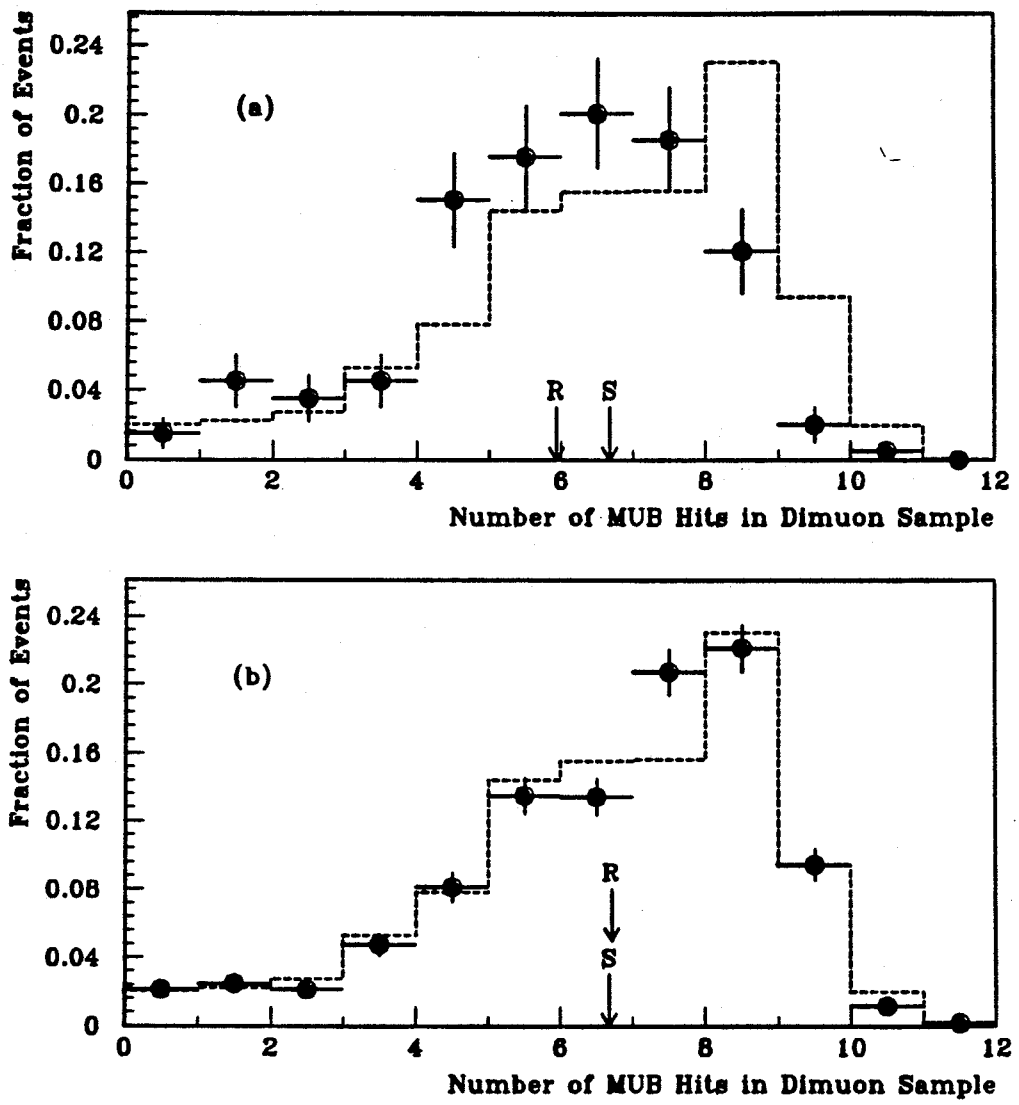

Analysis Conditions	
1989 data sample	Runs 3302 - 6057
1990 data sample	Runs 7912 - 13620
Analysis package	DELANA31/33(1990),GEDTAN
Selection cuts	$\dagger_{A1}, \dagger_{A2}, \dagger_{A3}, \dagger_{B4}, \dagger_{B7}, \dagger_{A8}, \dagger_{A10}$
Detector simulation	DELSIM35
Dimuon generator and sample size	DYMU3: 8639 events
Ditau generator and sample size	KORALZ: 8998 events
Simulated dimuon:ditau ratio	0.974:0.026